P-TYPE POINT CONTACT GERMANIUM DETECTORS AND THEIR APPLICATION IN RARE-EVENT SEARCHES

Graham Kurt Giovanetti

A dissertation submitted to the faculty at the University of North Carolina at Chapel Hill in partial fulfillment of the requirements for the degree of Doctor of Philosophy in the Department of Physics.

Chapel Hill
2015

Approved by:

John F. Wilkerson

Gerald Cecil

Jonathan Engel

Reyco Henning

David C. Radford

ABSTRACT

Graham Kurt Giovanetti: P-type Point Contact Germanium Detectors and Their Application in Rare-Event Searches
(Under the direction of John F. Wilkerson)

In the last two decades, experimental results from the direct detection of solar, reactor, and atmospheric neutrinos have provided convincing evidence that neutrinos have mass, the first definitive evidence of physics beyond the Standard Model. The existence of massive neutrinos opens many questions about the neutrino's intrinsic properties, including the absolute mass, the relative hierarchy of the neutrino mass states, and the Majorana or Dirac nature of the neutrino. The Majorana Demonstrator is an array of p-type point contact (PPC) high purity germanium detectors that will search for the neutrinoless double-beta decay ($0\nu\beta\beta$) of ^{76}Ge, a process that can only occur if the neutrino is a Majorana particle. PPC detectors have several characteristics that make them well suited for a ^{76}Ge $0\nu\beta\beta$ search, including sub-keV energy thresholds that allow for background rejection based on low-energy x-ray tagging. This feature makes the Majorana Demonstrator sensitive to signals that might be present from processes that are not in the current Standard Model of particle physics.

The Majorana Low-background Broad Energy Germanium Detector at KURF (MALBEK) is a PPC detector operated at the Kimballton Underground Research Facility (KURF) in Ripplemead, VA. MALBEK was used to test the stability and performance of PPC detectors and study sources of background near the detector energy threshold. It was found that the dominant background below 1 keV in MALBEK data is due to slow surface events, a class of signals originating from interactions that occur near the detector surface. Techniques were developed for identifying surface events and simulating their formation and distribution. These techniques were then applied to 89.5 kg-d of data and searches were performed for

signals from weakly interacting massive particles (WIMPs), solar axions, and Pauli exclusion principle violating electron transitions. No evidence of a signal was found. These results are presented in the context of present and future experiments, including the MAJORANA DEMONSTRATOR.

ACKNOWLEDGEMENTS

I would like to thank John Wilkerson for his support, mentorship, and for providing a careful balance of guidance and freedom throughout my graduate career. I would also like to thank Reyco Henning for his mentorship and advice. I have had the pleasure of working with and learning from many great scientists. Thanks to Jason Detwiler, Steve Elliott, Kevin Giovanetti, Matt Green, Mark Howe, Mike Marino, Chris O'Shaughnessy, David Radford, Alexis Schubert, and all of my other MAJORANA and UNC ENAP collaborators. A special thank you to Paddy Finnerty who was the driving force behind MALBEK and a constant source of useful discussion and welcome distraction. Thank you to Sean Finch, Derek Roundtree, Werner Tornow, Lhoist North America, Matthew Busch, and the rest of the TUNL technical staff for their logistical support and help with MALBEK operations. Finally, thanks to my parents for the gift of education, my family and friends for their unwavering support, and Catherine for keeping it all fun.

I was supported during graduate school by Mr. Lovick P. Corn and Mrs. Elizabeth Turner Corn through the University of North Carolina at Chapel Hill Graduate School, the United States Department of Energy (DOE) under Grant DE-FG02-97ER41041, and the DOE Office of Science Graduate Fellowship Program.

TABLE OF CONTENTS

LIST OF TABLES

LIST OF FIGURES

LIST OF ABBREVIATIONS AND SYMBOLS

$0\nu\beta\beta$	Neutrinoless Double-beta Decay
$2\nu\beta\beta$	Double-beta Decay
BEGe	Broad Energy Germanium
C.L.	Confidence Level
CMB	Cosmic Microwave Background
DFSZ	Dine, Fischler, Srednicki, and Zhitnitsky Axion Model
DSWT	Discrete Stationary Wavelet Transform
DWT	Discrete Wavelet Transform
GAT	Germanium Analysis Toolkit
HPGe	High Purity Germanium
KSVZ	Kim, Shifman, Vainstein, and Zakharov Axion Model
KURF	Kimballton Underground Research Facility
MALBEK	Majorana Low-background BEGe Detector at Kimballton
PEP	Pauli Exclusion Principle
PPC	P-type Point Contact
Q	End-point Energy
ROI	Region of Interest
SBC	Single Board Computer
SIS3302	Struck Innovativ Systeme 3302 Digitizer
SURF	Sanford Underground Research Laboratory
WIMP	Weakly Interacting Massive Particle
WMAP	Wilkinson Microwave Anisotropy Probe

CHAPTER 1: Introduction

Section 1.1: Neutrinoless Double-beta Decay

Physicists have observed the flavor oscillation of neutrinos from a variety of sources [1], showing in all cases that the neutrino flavor states $(\nu_e, \nu_\mu, \nu_\tau)$ are distinct from the neutrino mass states (ν_1, ν_2, ν_3) and can be written as

$$\nu_\alpha = \sum_i U_{\alpha i} \nu_i \tag{1.1}$$

where $\alpha = e, \mu, \tau$; $i = 1, 2, 3$; and $U_{\alpha i}$ is the neutrino mixing matrix. Oscillation experiments have also demonstrated that the mass splitting between the first and second neutrino mass states is much smaller than the mass splitting to the third mass state,

$$\Delta m^2_{sol} = m_2^2 - m_1^2 \ll \Delta m^2_{atm} = |m_3^2 - (m_1^2 + m_2^2)/2| \tag{1.2}$$

where Δm^2_{sol} is determined by measuring solar neutrino oscillation $(\nu_e \to \nu_\mu, \nu_\tau)$ and reactor neutrino oscillation $(\bar{\nu_e} \to \bar{\nu_\mu}, \bar{\nu_\tau})$, and Δm^2_{atm} is determined by observing atmospheric and accelerator neutrino disappearance $(\nu_\mu \to \nu_\tau)$. While the relative mass splittings are known, oscillation experiments are only sensitive to the absolute value of Δm^2_{atm}, leaving two possible neutrino mass hierarchy scenarios. In the normal hierarchy, named for its similarity to the mass hierarchies in the quark and charged lepton sector, ν_3 is the heaviest mass state. In the inverted hierarchy, ν_3 is lighter than ν_1 and ν_2.

The absolute mass of the neutrino is also unknown. The current best direct limits on the neutrino mass come from the Mainz group [2], who constrained the superposition of the neutrino mass states to be less than 2.3 eV at the 95% C.L. by looking for distortions

in the tritium beta-decay spectrum around the 18.6 keV endpoint energy. Additional constraints on the sum of the neutrino masses come from indirect cosmological probes. An analysis of the anisotropies of the cosmic microwave background (CMB) using five years of Wilkinson Microwave Anisotropy Probe (WMAP) data limits the sum of the neutrino masses, $\sum m_\nu < 1.3$ eV [3]. A 2013 measurement by the PLANCK collaboration combined with other probes of the matter distribution of the Universe results in even more stringent constraints, $\sum m_\nu < 0.23$ eV [4]. KATRIN, the next generation direct neutrino mass tritium beta-decay spectrometer aims to improve sensitivity of the Mainz experiment by one order of magnitude [5].

Neither oscillation experiments nor direct neutrino mass measurements provide insight into the neutrino mass generation mechanism or the neutrino's Majorana nature. The neutrino interacts via the weak force, which only couples to the negative chirality component of a fermion field. In the limit of a massless particle, chirality is indistinguishable from helicity. In the case of a massless neutrino, this implies that any right(left)-handed (anti-)neutrino would be sterile and unobservable, regardless of the Majorana or Dirac nature of the particle. The Standard Model therefore includes only a left(right)-handed (anti-)neutrino. With the introduction of neutrino mass, the negative chirality state (ν_l) becomes a superposition of $\pm\frac{1}{2}$ helicity states, where the contribution from the $+\frac{1}{2}$ helicity state is heavily suppressed by a factor proportional to $\frac{m_\nu}{E}$, where E is the neutrino energy. In this case, neutrino mass can be added to the Standard Model Lagrangian in one of several ways. Most simply, massive neutrinos can be included analogously to the charged leptons by introducing a Dirac mass term, requiring the addition of a (anti-)neutrino with positive(negative) chirality and mostly right(left)-handed helicity. However, this requires a neutrino Yukawa coupling many orders of magnitude smaller than couplings in the charged lepton sector. A second method for generating neutrino mass relies on the fact that neutrinos are electrically neutral. If neutrinos are identical to anti-neutrinos, a suggestion first made by Ettore Majorana [6], then a Majorana term can be added to the Standard Model Lagrangian that violates lepton number

conservation and couples neutrinos to anti-neutrinos. The addition of a Majorana mass term is forbidden for charged particles because it violates charge conservation but could be allowed for electrically neutral neutrinos. The only practical way to determine whether the neutrino is a Majorana particle is by observation of neutrinoless double-beta decay ($0\nu\beta\beta$) [7].

For some even-even nuclei, the single-beta decay channel is either energetically forbidden, due to pairing forces, or heavily suppressed, e.g. ^{48}Ca $\rightarrow$ ^{48}Ti. In these cases, the nucleus can double-beta decay ($2\nu\beta\beta$), simultaneously converting two neutrons into two protons and emitting two β particles and two anti-neutrinos. This process was originally suggested in 1935 by Maria Goeppert-Mayer, who estimated a lifetime for the process of approximately 10^{17} years [8]. It wasn't until 1987 that the first laboratory observation of $2\nu\beta\beta$ was made by Elliott, Hahn, and Moe in ^{82}Se [9]. Physicists are now searching for neutrinoless double-beta decay ($0\nu\beta\beta$), a related process postulated in 1939 by Wendell H. Furry [10]. In $0\nu\beta\beta$, two neutrons are converted to two protons with the emission of two β particles and no neutrinos. In the simplest case of light neutrino exchange, the inverse half-life of $0\nu\beta\beta$ can be written as

$$\frac{1}{T^{0\nu}_{1/2}} = G_{0\nu}(Q_{\beta\beta}, Z)|M_{0\nu}|^2\langle m_{\beta\beta}\rangle^2, \tag{1.3}$$

where $G_{0\nu}(Q_{\beta\beta}, Z)$ is a calculable phase space factor, $M_{0\nu}$ is a nuclear matrix element, and $\langle m_{\beta\beta}\rangle$ is the effective Majorana neutrino mass. Observation of $0\nu\beta\beta$ would indicate that the neutrino is a Majorana particle, show that lepton number is not conserved, and give a measure of the effective Majorana neutrino mass.

The signature for $0\nu\beta\beta$ is the emission of two electrons whose summed energy is equal to the double-beta decay end-point energy ($Q_{\beta\beta}$). If the effective Majorana neutrino mass is of the order Δ^2_{atm}, the expected $0\nu\beta\beta$ event rate from a tonne of isotope is approximately 1 count/year. For an experiment to be sensitive to this small an event rate, the background contributions in the signal region of interest (ROI) must be kept to equivalently low levels. This is accomplished by locating the $0\nu\beta\beta$ experiment in a deep underground environment, surrounding the detector by shielding, and assembling the detector from carefully screened

low-background materials.

There are several experimental aspects that must be considered when building a $0\nu\beta\beta$ experiment, both when selecting the source isotope and defining the detection technique. First, the source isotope should be readily attainable, either due to its high natural abundance or through an established enrichment process, so that the detector mass can be made large without prohibitive cost. Selecting an isotope with a higher $Q_{\beta\beta}$ value has the added benefit of moving the $0\nu\beta\beta$ ROI above the majority of backgrounds from the U and Th decay chains and providing a larger phase space for the decay. Second, the detector itself should have good energy resolution in the ROI, which maximizes the signal to background ratio. Additional background reduction can be accomplished if the detector allows event reconstruction, has good timing resolution, or can tag the daughter nucleus from the decay. Lastly, the detector must be constructed of radio-pure components and installed in a low-background environment. This means that the detector must be built underground, at a depth sufficient to limit high-energy muon induced neutrons and cosmogenically induced backgrounds in the detector components. The detector must also be installed in a shield that will minimize the environmental and anthropogenic backgrounds present underground, such as fast neutrons from (α, n) reactions in the surrounding rock, gammas from local sources, and radon. The detector components themselves must also be constructed from materials with low levels of primordial contaminants and limited cosmogenic activation.

Section 1.2: The Majorana Demonstrator

The Majorana collaboration is currently building the Majorana Demonstrator, a 40 kg array of high purity germanium (HPGe) detectors. Approximately 30 kg of these detectors are constructed from material enriched to 87% in ^{76}Ge, allowing the Demonstrator to search for $0\nu\beta\beta$ while establishing the feasibility of constructing a future tonne-scale germanium-based experiment [11]. Individual germanium crystals are mounted in detector modules constructed of radio-pure plastics and electroformed copper [12]. Detector modules

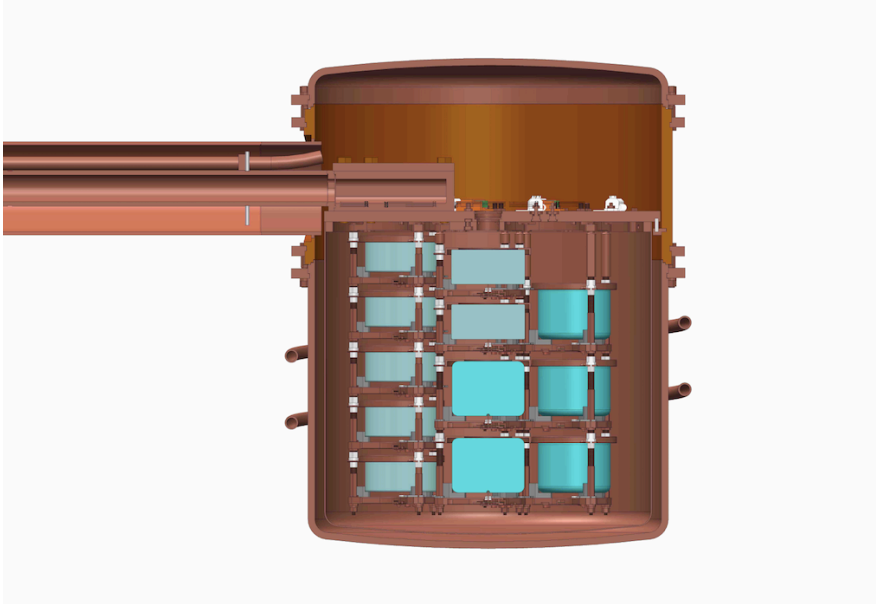

Figure 1.1: Drawing of a MAJORANA DEMONSTRATOR cryostat. Strings of germanium crystals (turquoise) hang from the cryostat cold plate.

are stacked vertically to build detector strings that are deployed in a vacuum cryostat as shown in Figure 1.1. The strings create a thermal path from the cryostat cold plate to the germanium crystals, which must be kept at cryogenic temperatures during operation. Two cryostats, each containing 20 kg of detectors, are under construction in a cleanroom facility at the 4850' level of the Sanford Underground Research Facility (SURF) in Lead, SD. Once complete, these cryostats will be installed in a compact shield made from electroformed copper, commercial high purity copper, lead, plastic, and an active muon veto. The DEMONSTRATOR shield is shown in Figure 1.2. The background goal for the DEMONSTRATOR is 3 background counts/tonne/year in the 4 keV wide ROI around the 2039 keV ^{76}Ge endpoint energy. This scales to a rate of 1 count/tonne/year for a DEMONSTRATOR-style tonne-scale experiment, the required background level for sensitivity to $0\nu\beta\beta$ if neutrinos follow the inverted mass hierarchy. The projected background rate for the DEMONSTRATOR based on radio-assay of the cryostat and shield components is less than or equal to 3.1 counts/tonne/year.

To achieve the background goal of 3 counts/tonne/year/ROI, the DEMONSTRATOR must

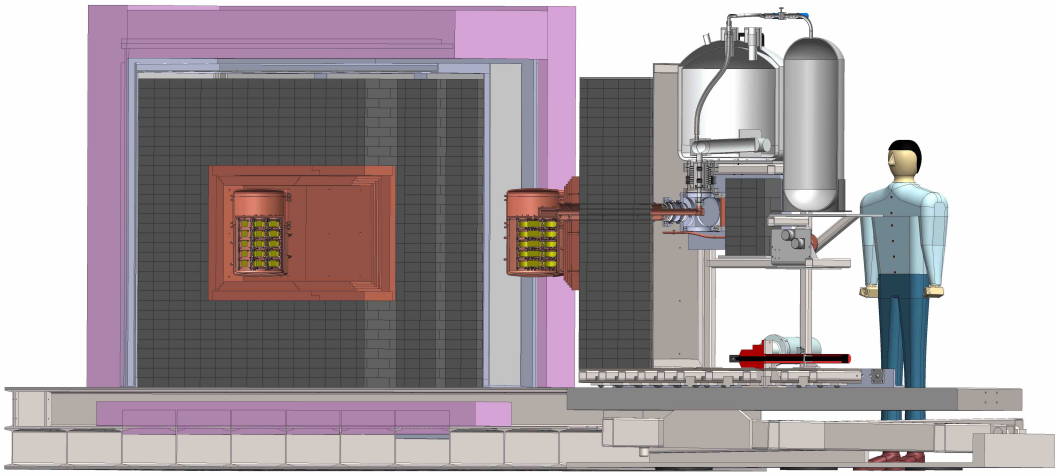

Figure 1.2: Cutaway of the MAJORANA DEMONSTRATOR shield. The shield is constructed of electroformed copper, commercial high-purity copper, lead, and plastic and houses two cryostats containing strings of germanium detectors.

be able to distinguish the neutrinoless double-beta decay signal, which is a localized, effectively single-site event, from background multi-site events, e.g. events from gamma-rays Compton scattering multiple times within a single HPGe detector. Initially, segmented N-type coaxial detectors were considered for use in the DEMONSTRATOR due to their ability to tag events occurring across multiple segments. However, these detectors are difficult to manufacture and handle and, because each segment requires its own readout channel, increase the amount of potentially radio-impure material inside the cryostat.

An alternative to segmented detectors are P-type point contact (PPC) detectors, a relatively new HPGe detector technology with a cylindrical geometry and a small, few millimeter diameter signal contact. Figure 1.3 shows a schematic drawing of a PPC detector. These detectors have several advantages over N-type segmented detectors. First, PPC detectors have an even weighting potential throughout the bulk of the crystal that rapidly increases around the point contact, resulting in characteristically different signal shapes for multi-site and single-site events. This allows for multi-site event discrimination comparable to or better than a segmented detector [13]. Second, because of their small contact size, PPC detectors

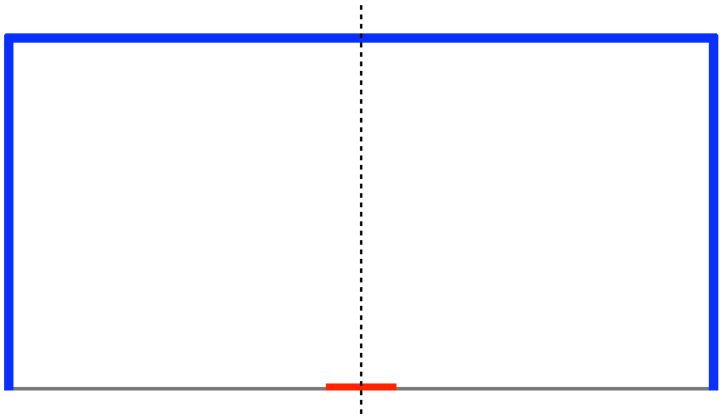

Figure 1.3: Cross-sectional drawing of a PPC detector. The detector is axially symmetric about the dashed line. The n^+ contact is shown in blue and the p^+ point contact is shown in red. Bias voltage is applied to the n^+ contact and signals are read out from the p^+ contact. PPC detectors typically have a diameter around 60 mm and heights ranging from 30 to 50 mm.

have a capacitance on the order of 1 pF and can be operated with sub-keV energy thresholds [14]. This can be used to reduce $0\nu\beta\beta$ backgrounds from cosmogenically produced ^{68}Ge using a time correlated analysis cut. Long lived ^{68}Ge (Q_{ec} = 106 keV, $T^{1/2}$ = 270.8 days) decays via electron capture to ^{68}Ga (Q_{ec} = 2921.1 keV, $T^{1/2}$ = 67.7 min) and can contribute background events in the $0\nu\beta\beta$ ROI. This rate can be reduced by up to 98% by tagging L-shell capture (1.3 keV) and K-shell capture (10.3 keV) events that occur during the ^{68}Ge decay and vetoing for several ^{68}Ga half-lives. Finally, PPC detectors are simpler to fabricate than segmented detectors and only require one set of readout electronics per detector, reducing the amount of material within the detector cryostat. For these reasons, the MAJORANA collaboration is using PPC detectors in the DEMONSTRATOR.

The use of low energy threshold PPC detectors in the DEMONSTRATOR has the added advantage of making the detector sensitive to nuclear recoils from weakly interacting massive particles (WIMPs), a popular candidate for dark matter, as well as other non-Standard Model processes, such as axion-electron scattering and Pauli exclusion principle violating electron transitions.

Section 1.3: Direct WIMP Detection

Astronomical observations of galactic rotation curves, strong lensing, and the anisotropy of the CMB all suggest that visible matter only accounts for a fraction of the total mass of the Universe [1]. The missing mass can be attributed to gravitationally interacting but non-luminous dark matter that formed shortly after the Big Bang and coalesced into halos around galaxies as the Universe cooled. While dark matter has not been directly detected, a recent measurement by the Planck satellite predicts that it constitutes 26.8% of the energy density in the Universe [4]. A viable particle candidate for dark matter must be stable over the lifetime of the Universe, electrically neutral, non-relativistic and, to explain the anisotropy of the CMB, non-baryonic.

Weakly interacting massive particles (WIMPs) are a class of dark matter particle candidates that only interact gravitationally and through the weak force and are projected to have masses between 1 and 1000 GeV. WIMP-like particles are predicted in many extensions of the Standard Model, including supersymmetric theories [15] and theories with extra dimensions [16]. There are three general approaches used to search for WIMPs. Indirect searches look for signature decay or annihilation products from WIMPs in the cosmic ray spectrum, collider based searches look for missing energy due to WIMPs produced during a particle collision, and direct searches look for WIMPs elastically scattering from nuclei in terrestrial detectors as the earth travels through the galactic dark matter halo.

The expected WIMP-nuclear recoil spectrum shape in a direct dark matter detector can be calculated by convolving the presumed galactic WIMP velocity distribution with the angular scattering distribution [17]. This results in a spectrum that falls off exponentially with energy and has a cutoff at the escape velocity of the halo. The WIMP interaction rate is determined by the WIMP flux, which depends on the WIMP density, velocity, and mass, and the WIMP interaction cross-section. This rate should modulate by a few percent annually as the earth's velocity relative to the WIMP halo changes as the earth rotates about the sun. The interaction cross-section depends on the coupling of WIMPs to baryons

and could be spin-dependent, which requires the target nucleus to have non-zero spin, or spin-independent, which would scale as the square of the target nucleus mass [18]. Current spin-independent experiments are approaching sensitivity to scattering cross sections on the order of 1×10^{-45} cm^2. To achieve this level of sensitivity, WIMP detectors rely on many of the same techniques employed by $0\nu\beta\beta$ experiments, deploying large-mass radio-pure detectors deep underground and collecting data over long periods of time.

Recently, several experiments have reported anomalous results that suggest the existence of an approximately 10 GeV WIMP. The longest standing claim is from DAMA/LIBRA, an array of radio-pure NaI detectors that has collected data for over 14 years. DAMA/LIBRA measures an annual rate modulation with a significance of 9.3σ that can be attributed to a low-mass WIMP [19]. A similar annual modulation was reported by CoGeNT in three years of data collected with a PPC germanium detector similar to those that will be used in the Demonstrator [20], although new analyses of the CoGeNT data, both by the collaboration [21] and others [22], find a reduced signal significance. An additional hint of a low-mass WIMP was reported by CRESST-II, who initially reported a CoGeNT compatible signal in an array of $CaWO_4$ crystals [23]. An improved, lower-background version of the experiment excludes the original signal region [24]. The most recent signal claim comes from CDMS-Si, which uses a subset of the CDMS-II detectors made from silicon. CDMS-Si expected to measure 0.5 background events in their ROI after collecting 140 kg-d of data and found 3 events, a result best fit by an 8.6 GeV WIMP that is consistent with the CoGeNT signal region [25].

A number of other experiments have performed searches that are in disagreement with the positive low-mass WIMP results. The strictest limits on spin-independent interactions come from LUX [26], a dual-phase xenon time projection chamber, and SuperCDMS [27], a germanium-based detector that sets the best limits for WIMPs with masses below 6 GeV. In light of the contradictory experimental results, there have been efforts to show that various astrophysical and experimental corrections can bring the disagreements into alignment, for

example [28, 29]. Ultimately, model independent tests are needed to resolve the ambiguity in the interpretation of the possible WIMP signal detections.

There are currently two collaborations operating PPC detectors that should be sensitive to the signal excess reported by CoGeNT. The CDEX-TEXONO collaboration is running the CDEX-1 PPC detector at the China Jinping Underground Laboratory. The detector is surrounded by a NaI(Tl) crystal anti-Compton veto and operated within a conventional lead shield. First results from CDEX-1 using 53.9 kg-d of data are in conflict with the CoGeNT signal presented in [30]. While the energy threshold, detector geometry, and energy spectra are very similar between the two detectors, the analyses differ in their treatment of backgrounds caused by energy degraded surface events. These contradictory results highlight the importance of understanding detector backgrounds when performing a WIMP search with a PPC detector. The MAJORANA collaboration is also operating PPC detectors sensitive to nuclear recoils from a low-mass WIMP. The first of these is the MALBEK detector, a single PPC that ran underground between January 2010 and August 2012 as part of the research and development program for MAJORANA.

Section 1.4: Outline of This Dissertation

The MAJORANA Low-background Broad Energy Germanium Detector at KURF (MALBEK) is a PPC detector housed at the Kimballton Underground Research Facility (KURF). MALBEK was used to test the performance of PPC detectors and to study sources of background relevant to searches for $0\nu\beta\beta$, WIMP dark matter, solar axions, and other non-Standard Model physics accessible to PPC germanium detectors.

Chapter 2 describes the MALBEK detector in detail and provides an overview of the basic data selection cuts used to generate an energy spectrum. Chapter 3 is an in-depth study of surface events, the dominant background in the MALBEK detector below 1 keV, and includes a discussion of how best to identify and remove them. Chapter 4 develops a model for surface event formation and compares results from a surface event simulation

to data collected with MALBEK. Finally, Chapter 5 describes searches for WIMPs, solar axions, and Pauli exclusion principle violating electron transitions that were performed using 89.5 kg-d of data collected at KURF.

CHAPTER 2: The MAJORANA Low-background BEGe Detector at KURF

Section 2.1: Detector and Shielding

The MAJORANA Low-background Broad Energy Germanium Detector at KURF (MALBEK) is a 450 g high purity germanium detector manufactured by Canberra Industries. Broad Energy Germanium (BEGe) detectors are Canberra's commercial line of p-type point contact (PPC) detectors aimed at gamma-ray spectroscopy and sample radio-assay measurements. BEGe detectors are manufactured with a thin Li contact on the face of the detector and are typically operated within a windowed cryostat to increase the efficiency for detecting x-rays and low energy gamma-rays. This is not a desirable feature in a low-background rare-event detector, so the MALBEK crystal was produced with a full thickness Li contact and installed in a custom-made detector mount and cryostat machined from low-background, oxygen-free high conductivity (OFHC) copper. The MALBEK detector also has a smaller diameter point contact and a different aspect ratio than a standard BEGe detector. A complete description of the MALBEK geometry, materials used in the MALBEK cryostat, and information on the radio-purity of individual components can be found in [31].

MALBEK is housed at the Kimballton Underground Research Facility (KURF), a laboratory located on the 14th level of Lhoist North America's Kimballton mine in Ripplemead, VA. KURF is operated and maintained by Virginia Polytechnic Institute and hosts experiments from a number of partner institutions. The Kimballton mine follows a seam of limestone as it passes underneath nearby Butt Mountain, so the overburden at the laboratory site varies significantly as a function of zenith angle. Recent measurements estimate the effective depth at KURF to be 1450 meters of water equivalent [32]. The KURF laboratory building is accessible from the surface by vehicle and is outfitted with power, phone, and a high speed

fiber internet connection. Most experiments at KURF are contained in modified industrial shipping containers that provide an additional level of cleanliness and isolation from the mine environment.

The MALBEK infrastructure is described in detail in Padraic Finnerty's dissertation [33]. In brief, the MALBEK experiment is housed in two half-sized shipping containers. One container holds the detector, the detector shield, and the liquid nitrogen fill system. A second container houses the data acquisition computer, electronics, and slow control systems. A conduit for signal and data lines connects the two trailers. Both containers are equipped with a HEPA air filtration system and dehumidifiers to reduce airborne particulate and humidity. This is important both for the overall cleanliness of the experiment as well as for the protection of data acquisition electronics from diesel particulate generated by mining equipment.

The MALBEK shield was designed by engineers at the Triangle Universities Nuclear Laboratory and is shown schematically in Figure 2.1. The detector and liquid nitrogen dewar can be lifted into the shield from below with a pallet jack. This eliminates the need to disassemble the shield to access the detector, reducing the risk of shield component contamination from improper handling. The outermost shielding layer is 25.4 cm of polyethylene decking material that is not shown in Figure 2.1. Polyethylene has a high neutron capture cross section and is used to block (α,n) and fission neutrons from the cavern walls [34]. Inside the polyethylene is a sealed Lexan box that is continuously purged with dry boil-off nitrogen to reduce radon levels near the detector. The innermost shielding layers are made from lead. A 20 cm outer lead layer is built from 180 low-background lead bricks purchased from Sullivan metals with ^{210}Pb activity less than 2.5 Bq/kg [35]. Each brick was etched in a nitric acid bath to ensure the surfaces were free from contamination before being stacked in the shield. The 2.54 cm inner lead layer is constructed from ancient lead provided by Juan Collar of the University of Chicago. The ancient lead has ^{210}Pb activity less than 0.01 Bq/kg [33]. A teflon tube is routed through the shield so that a 1 μC ^{133}Ba source on a piano wire can be

inserted into the shield for detector calibrations.

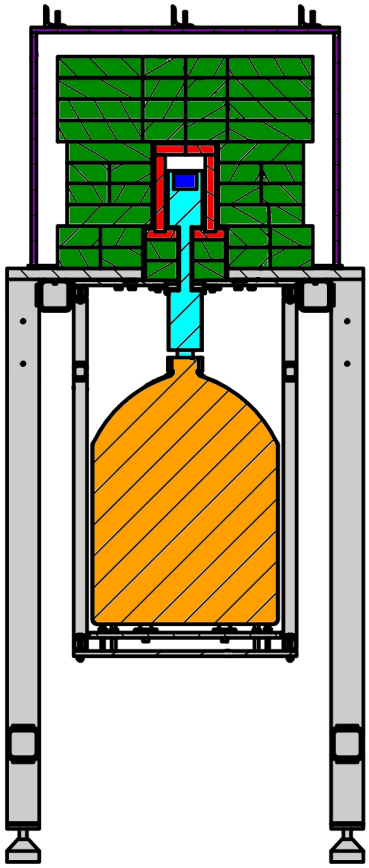

Figure 2.1: Drawing of the MALBEK shield. The support table (grey) is approximately 140 cm tall. The germanium crystal (dark blue) sits within a copper vacuum cryostat (light blue). The innermost shield layer is made from ancient lead (red). This is surrounded by Sullivan lead (green) and a Lexan box that is flushed with boil-off nitrogen. The detector and dewar (goldenrod) can be lowered from the shield without unstacking the lead bricks. The polyethylene outer shield layer is not shown. Drawing is courtesy of Matthew Busch.

Section 2.2: Data Acquisition System and Slow Controls

The MALBEK data acquisition system is built around `ORCA`, the object-oriented real-time control and acquisition software package developed at the University of North Carolina at Chapel Hill by Mark Howe [36]. `ORCA` represents hardware and system processes with graphical objects that can be manipulated and linked graphically to intuitively build complex readout schemes and slow control systems. `ORCA` also includes its own C-like scripting

language, `ORCAScript`, that can be used to automate data taking routines, monitor detector systems and data quality, and plot and filter the data stream in real-time. `ORCA` is used for all of the MALBEK data readout and slow control operation. An overview block diagram of the MALBEK data acquisition system is shown in Figure 2.2.

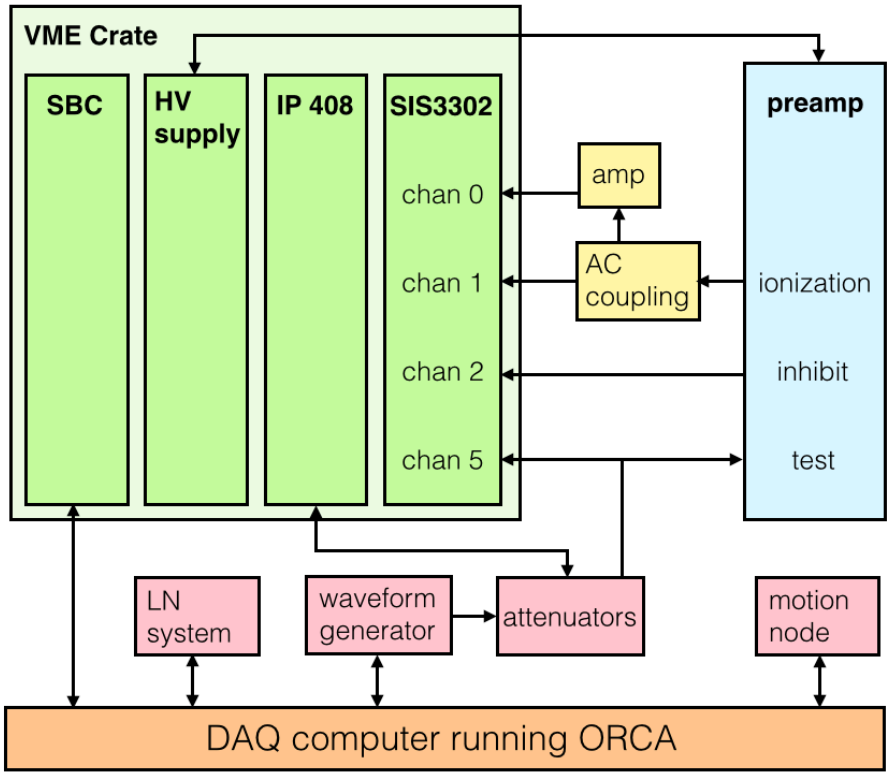

Figure 2.2: Block diagram of the MALBEK data acquisition system.

MALBEK is outfitted with a Canberra pulse-reset preamplifier with an approximately 40 ms reset period. The preamplifier has two identical signal outputs. One of the outputs is AC-coupled into a Struck Innovativ Systeme 3302 (SIS3302) eight-channel 16-bit 100-MHz VME digitizer. This channel has an energy range from 5 keV to 3 MeV and was used to study the MALBEK background spectrum around the ^{76}Ge double-beta decay endpoint energy [31]. The second preamplifier output passes through a NIM-based Phillips Scientific 777 linear amplifier before being digitized. This channel has an energy range from 0.3 keV to 160 keV and is used for the rare-event searches presented in this dissertation. Both

SIS3302 signal channels self-trigger on the output of an on-board trapezoidal filter, which helps discriminate low amplitude signals from noise. The preamplifier pulse-reset signal, which indicates when a pulse-reset occurs, is also digitized by the SIS3302. When the reset channel is triggered a small data record containing the timestamp of the reset is placed in the `ORCA` data stream. In order to reduce the size of MALBEK data files, basic real-time filtering is implemented using `ORCAScript` to remove events associated with preamplifier resets that are easily distinguishable based on their shape. This filtering is not 100% efficient and offline pulse-reset event removal is also performed.

An Agilent 33220A arbitrary waveform generator is attached to the test input of the preamplifier and injects a test pulse at 10 sec intervals during data taking. The waveform generator events provide a useful means of tracking the detector resolution and stability over the long run periods. A sync pulser from the waveform generator is fed into a channel of the SIS3302 so that a record is captured in the `ORCA` data stream coincident with every waveform generator induced event. The waveform generator output can optionally be attenuated using a set of step attenuators controlled by an Acromag IP408 digital I/O VME module. This system is used to generate sets of events with a known waveform shape and energy. These events are then used to test the trigger efficiency of the digitizer and measure cut acceptance efficiencies near the detector energy threshold.

The detector is biased using an ISEG VHQ224L, a 5 kV VME-based high voltage supply with selectable polarity. The ISEG has peak to peak ripple less than 2 mV and can ramp the high voltage on or off at a programmable rate. The VHQ224L is controlled and monitored by `ORCA`.

Liquid nitrogen levels in the detector and shield-purge dewar are monitored using an American Magnetics, Inc. (AMI) 286 multi-channel liquid level sensor. The AMI 286 is also used to automate dewar fills from two 240 l dewars that sit outside of the MALBEK shipping containers. `Orca` records the dewar level and fill state from the AMI 286 in the data stream so that data collected during liquid nitrogen filling can be tagged and removed. A MotionNode

accelerometer is attached to the detector stand and triggers on accelerations greater than 190 μg. This was intended to provide a record of vibrations caused by haul trucks passing the laboratory building or other mining operations that could cause microphonic events. No vibration events were recorded during the run period, perhaps due to the sheer mass of the shield and the isolation provided by the shipping container.

There are several systems in place to protect the detector in the event of a power outage or liquid nitrogen shortage. The entire data acquisition system is on an uninterruptible power supply capable of supporting the system for several minutes. Upon loss of power, the high voltage bias of the detector is ramped down by `ORCA`. If power is maintained but liquid nitrogen levels fall below a set point, the detector is automatically unbiased by the data acquisition computer. In the event of a computer failure that occurs simultaneously with a loss of liquid nitrogen, a custom circuit will automatically un-bias the detector.

An `ORCAScript` is used to automate MALBEK data taking. New runs begin hourly. The script collects run statistics, including channel trigger rates, energy spectra, and the status of slow control systems, like liquid nitrogen levels and bias supply current, and sends a daily summary email to users. The script also watches for excursions from standard operating conditions, such as liquid nitrogen fills or loss of power, and sends alert emails to a subset of the user group.

2.2.1: Digitizer Configuration

The SIS3302 calculates the energy of events using a trapezoidal filter [37] with programmable decimation, peaking time, gap time, and tau factor. The decimation defines the rate of down-sampling that is performed on the waveform before the filter. The peaking time, gap time, and tau factor define the averaging time, delay time, and decay time constant of the trapezoidal filter. After a trigger, the first value and the maximum value of the filtered waveform in the energy buffer are written to memory. The optimal values for the decimation, peaking time, and gap time were determined by minimizing the width of

the spectral peak due to pulser events. The tau factor was determined by fitting the decay time of a set of physics waveforms collected with the SIS3302. The energy calculated by the digitizer trapezoidal filter was used for data quality monitoring. For physics data analysis, an offline energy reconstruction was performed. This is described in Section 2.4.1.

The SIS3302 also uses a fast trapezoidal filter for internal triggering to minimize the noise trigger rate near the detector threshold. When the filter output exceeds the channel's trigger threshold, a prescribed number of analog-to-digital converter (ADC) values are stored in the event memory. The SIS3302 fast trapezoidal filter has three configurable settings: decimation, peaking time, and sum-gap time, which is the sum of the peaking time and the gap time. The same peaking and gap time found to optimize the energy filter were used for the trigger filter. The optimal trigger threshold maximizes the trigger efficiency for low energy events while maintaining a manageable noise trigger rate. A 300 eV trigger threshold was used during MALBEK data taking, about two times higher than the measured full width at half maximum (FWHM) of a pulser peak. Figure 2.3 shows the trigger efficiency as a function of energy determined using the waveform generator and attenuators.

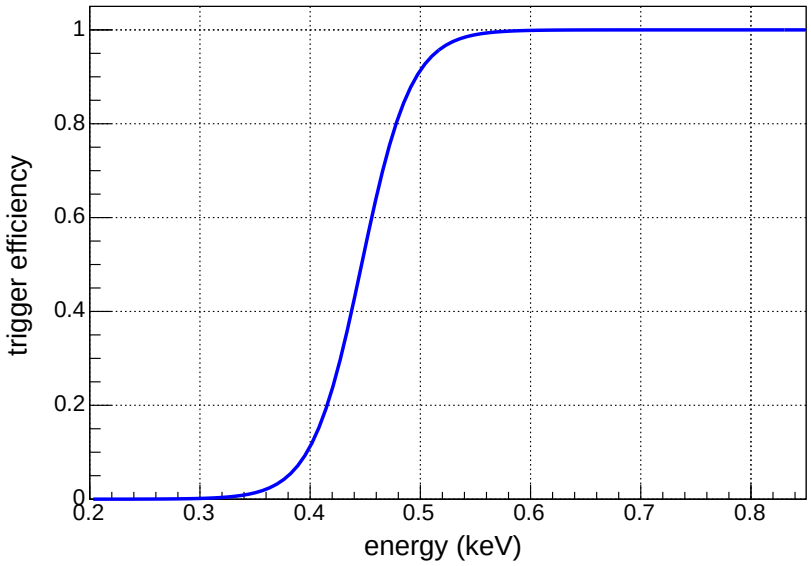

Figure 2.3: Trigger efficiency of the low energy SIS3302 channel determined using the waveform generator and attenuator system.

A user defined number of raw data samples are saved after every trigger. If the rising edge of an event is centered in the data buffer, the data sample length must only be twice the length of the energy trapezoidal filter to perform offline energy reconstruction. However, the position of the rising edge of the waveform changes with variations in the rise-time of an event, up to the length of the trigger trapezoidal filter peaking time. To accommodate this, an additional trigger filter peaking time of samples were added to the buffer length. Then the buffer length was rounded up to the nearest power of two, eliminating the need to truncate a waveform before performing frequency analyses, e.g. the wavelet denoising described in Section 3.3.1. 8192 samples were recorded for each event during data taking.

The location of an event's rising edge within the buffer can be manipulated in two ways. The original SIS3302 firmware had a pre-trigger delay setting that defined the number of samples written to event memory before a trigger, up to a maximum length of 1024 samples. During initial testing with the SIS3302, it was found that the maximum pre-trigger delay was too short to digitize sufficient baseline to perform offline filtering on very slow events. A new firmware specification was provided to Struck engineers who implemented a feature called buffer wrap. The buffer wrap writes a constant stream of ADC data to the event memory, keeping a programmable number of samples in the buffer. After a trigger, the remainder of the event buffer is filled with post-trigger data. This allows for arbitrarily long pre-trigger delays at the expense of increased digitizer dead time as the event memory is refilled after each trigger. The buffer wrap delay was set during data collection to place the rising edge of the slowest rise-time events in the center of the digitization window.

The SIS3302 has a programmable offset that determines the position of the waveform within the 16 bit range of the digitizer. This was set so that the resting baseline of the preamplifier had an ADC value of approximately 5000. This allowed for a large ADC range for positive valued physics events while maintaining the ability to fully digitize triggers caused by signals that oscillate about the baseline, e.g. microphonics.

After examining some of the initial data collected with the SIS3302 digitizer, it became

clear that there were bursts of noise present on the SIS3302 waveforms at 15 μs intervals. It was eventually determined that the noise originated from the VME-based single board computer (SBC) used to read out and control the SIS3302 and VHQ224L. To eliminate this noise, a readout scheme was implemented in `ORCA` that takes advantage of the dual data buffers on the SIS3302. During normal operation, the SIS3302 writes data to one of its buffers. The SBC does no polling at this time. At a set interval, the SBC polls the card and reads data from the first buffer. While this is happening, the SIS3302 writes any triggered event records to the second buffer. Once readout is complete, the SIS3302 begins writing to the original buffer and data written to the second buffer is discarded. This readout method eliminates the SBC polling related noise while reducing the detector lifetime by $\ll 1\%$.

Section 2.3: MALBEK Operation History

MALBEK arrived at the University of North Carolina at Chapel Hill in October of 2009. After initial detector testing and basic characterization measurements, MALBEK was moved to its permanent location at KURF in January of 2010. The first year of MALBEK operations underground were spent testing data acquisition system configurations for use with the MAJORANA DEMONSTRATOR. Data collection using the SIS3302 digitizer described in Section 2.2 began in March 2011. After a modest dataset was collected with MALBEK in the shield, it became evident that a significant and unexpected peak at 46.5 keV originating from ^{210}Pb was present in the data. This peak was accompanied by the set of lead x-rays between 70 and 90 keV and a bremsstrahlung continuum. Several possible sources of the ^{210}Pb contamination were identified: brass components within the cryostat, tin solder used to manufacture the detector pin, the innermost ancient lead shielding, and two lead shims used to hold the MALBEK crystal within the detector mount. Alexis Schubert performed a detailed simulation of the MALBEK internal geometry and shield and showed that, based on the shape of the bremsstrahlung continuum and the relative intensities of the ^{210}Pb peaks, the likely source of contamination was the lead shims [31]. In light of these simulation results,

MALBEK was removed from the shield on 24 October 2011 and the detector was driven from KURF to Canberra Industries in Meriden, Connecticut. At Canberra, the lead shims were removed and replaced with low-background PTFE. The data collected during this period are not suitable for a WIMP search due to the significant background contribution from ^{210}Pb in the region of interest. However, the ^{210}Pb contamination provided a useful low energy gamma-ray calibration source inside of the cryostat that will be discussed in detail in Chapter 3.

The detector returned to KURF on 26 October 2011, after spending less than three days on the surface. The detector was inserted into the shield and cooled and data taking commenced on 15 November 2011, 12 days after the surface exposure. The detector continued to collect data for 288 days until 8 August 2012, at which point it was removed from the shield to perform a set of source calibrations that are discussed in Chapters 3 and 4. The data collected over the 288 day period are divided into two distinct run periods separated by a period of frequent power outages at KURF, 15 November 2011 – 12 March 2012, during which 104 days of data were collected, and 9 April 2012 – 29 August 2012, during which 117 days of data were collected. The data processing and calibration described in Section 2.4 is performed separately on these two run periods.

Section 2.4: Data Processing

Before data collected with `ORCA` can be used to search for a signal, the data are processed and basic data selection cuts are applied. A comprehensive overview of the MALBEK data processing and selection can be found in [33]. A general overview will be given here.

`ORCA` saves data in a file containing an `XML` header that describes the configuration of the data acquisition system followed by a set of binary records from all objects that collected data during the run. `ORCA` files are processed using MAJORANA-`ORCAROOT`, a program that converts `ORCA` files into a `ROOT` [38] compatible format. The `ROOT` files are then processed using the Germanium Analysis Toolkit (`GAT`), a software package developed by the MAJORANA

collaboration for analyzing HPGe detector data [39]. `GAT` is a collection of processors that calculate parameters from an event, e.g. the event energy and rise-time. After the data are processed with `GAT`, the event energies are calibrated and cuts are applied to remove noise and other non-physics related signals.

2.4.1: Energy Calculation and Calibration

Event energies are calculated using a digital trapezoidal filter [37] implemented as a processor in `GAT`. First, event waveforms are pole-zero corrected to remove the decaying component of the signal caused by AC-coupling the pulse-reset preamplifier into the SIS3302 digitizer. The waveform is then filtered using a trapezoidal filter with an 11.0 μs peaking time and a 1.0 μs gap time. The maximum value of the filtered waveform is used as the uncalibrated energy of the event. The optimal peaking time and gap time were found by minimizing the resolution of a pulser energy peak by varying the two parameters.

MALBEK's copper cryostat and thick n^+ contact severely attenuate low energy gamma-rays and x-rays from external radioactive sources, so the energy calibration utilizes several x-ray peaks from cosmogenically activated isotopes within the germanium crystal. The peaks listed in Table 2.1 are fit with a gaussian function and a linear background function. The peak centroids are then fit with a linear equation to determine the conversion between the trapezoidal filter energy and ionization energy. This calibration is done separately for the two data taking periods.

Table 2.1: Peaks used for energy calibration. Peak energies are from [40].

Isotope	**Energy (keV)**
^{68,71}Ge L-capture	1.30
^{55}Fe K-capture	6.54
^{65}Zn K-capture	8.98
^{68}Ga K-capture	9.66
^{68,71}Ge K-capture	10.37

2.4.2: Data Selection Cuts

After processing the data with `GAT`, a series of cuts are applied to remove non-physics events. Two general classes of cuts are performed, cuts based on the timing of the event and cuts based on the waveform shape. For a detailed description of the definition and performance of these cuts, see [33].

The first timing based cut removes data runs collected immediately following detector re-biasing after a power outage. These runs were found to have increased trigger rates and can be eliminated without a significant impact on the down-time of the detector relative to the exposure lost during the power failure. The second timing based cut removes events that occur within 1 ms of a pulse-reset signal from the preamplifier. The preamplifier resets at approximately 25 Hz, so this cut reduces the live-time of the detector by about 5%. In a similar fashion, events that are coincident with the waveform generator signal are cut from the dataset. Lastly, the 15 minutes of data collected following a nitrogen fill are removed. The trigger rate over this time period temporarily spikes, likely due to microphonics caused by boiling nitrogen in the dewar and fill lines.

The waveform shape cuts are based on parameters calculated by `GAT` and are designed to eliminate microphonics and other noise-induced SIS3302 triggers. All of the following cuts are defined to accept 99% of signal events and are calibrated using a set of waveforms with energies between 0.3 and 7 keV created by injecting pulses from the waveform generator and attenuator system into the test input of the preamplifier. The first cut is based on the integral of the waveform. This removes events that oscillate about the baseline, including microphonics, triggers caused by noise picked up from the VME bus, and small amplitude, inverse polarity events thought to be caused by micro-discharges in the bias voltage circuit. The second cut uses the amplitude of the current signal of the waveform divided by the energy of the waveform. This parameter is commonly called A/E and is used at higher energies to identify multi-site events from gamma-rays that Compton scatter multiple times within the detector, see Section 1.2. In this case, the A/E value is sensitive to the same

oscillatory noise events identified by the integral cut as well as the inverse polarity micro-discharge events. The final waveform shape based cut uses the ratio of energies calculated by two trapezoidal filters with different shaping times [41]. This cut identifies any remaining microphonic events that are not removed by the integral and A/E cuts. The calculated signal acceptance efficiency after application of the timing and waveform shape cuts is shown in Figure 2.4.

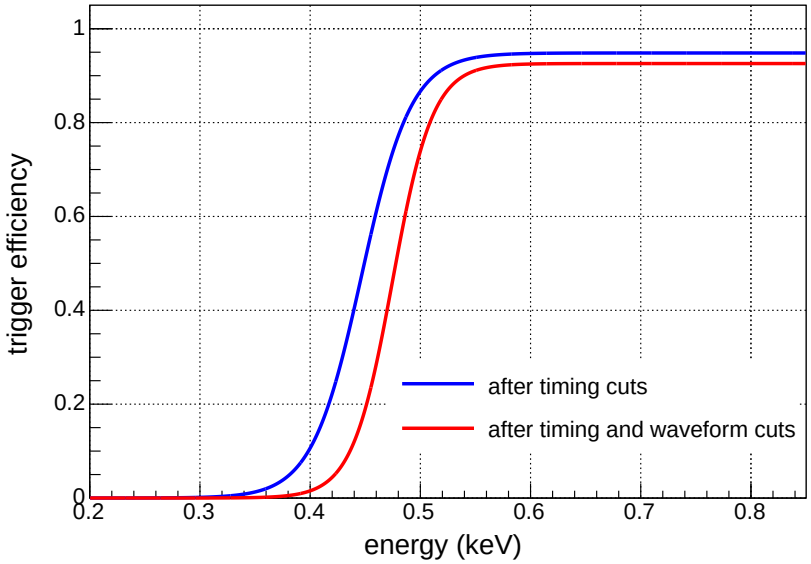

Figure 2.4: Basic data selection cut efficiencies. The signal acceptance efficiency after application of the timing cuts is shown in red and the signal acceptance efficiency after the timing cuts and waveform shape based cuts are applied is shown in blue.

With the data selection cuts in place, the MALBEK dataset can be used to explore physics backgrounds in the low energy region and, ultimately, search for signals from WIMPs, solar axions, and Pauli exclusion principle violating electron transitions. The next chapter will discuss a particularly difficult background to understand and eliminate, energy degraded events that originate from interactions occurring near the detector surface.

CHAPTER 3: Surface Events

Section 3.1: Signal Formation in PPC Detectors

Ionizing radiation incident on a High Purity Germanium (HPGe) detector will create electron-hole pairs proportional in number to the total energy deposited in the detector. Any mobile electrons (holes) created within the crystal's depleted region will drift towards the n^+ (p^+) detector contact under the influence of the electric field generated by the applied bias voltage and the space charge distribution within the detector. As the charges move, they induce currents on the contacts that are dependent on the number and velocity of the charge carriers and the field they are moving through. A single charge carrier q will induce a charge Q on an electrode

$$Q = -q\phi_0(\boldsymbol{x}) \tag{3.1}$$

where $\phi_0(\boldsymbol{x})$ is the weighting potential that describes the coupling of a charge carrier within the detector to a given electrode [42]. The weighting potential is calculated by setting the electrode of interest at a unit potential and all other electrodes at zero potential. Equation 3.1 provides a means of determining the signal that results from a particle interacting within a detector and creating electron-hole pairs. First, the mobile charges' paths through the crystal are calculated. These depend on the charge drift velocity as a function of field and crystal orientation and the motion of charge carriers due to diffusion and mutual repulsion. Then, the calculated charge trajectories are combined with the weighting potential to determine the induced current on the corresponding electrode.

To obtain a signal from the detector, the current induced on an electrode by the moving charges is integrated and converted to a voltage pulse by a charge-sensing preamplifier. In the absence of charge trapping within the detector, the amplitude of the voltage output from

the preamplifier will be proportional to the total number of electron-hole pairs created by the original interaction. While the amplitude of the signal will be the same for a given amount of energy deposited, the time evolution of the voltage signal is influenced by the topology of the charge carriers, the geometry of the detector, and the characteristics of the electric field within the crystal. Traditional detector geometries, like the coaxial and planar configurations often used for gamma ray spectroscopy, have smoothly varying weighting fields, short drift paths, and short collection times. This results in signals with consistent shapes regardless of the interaction position of the incident particle.

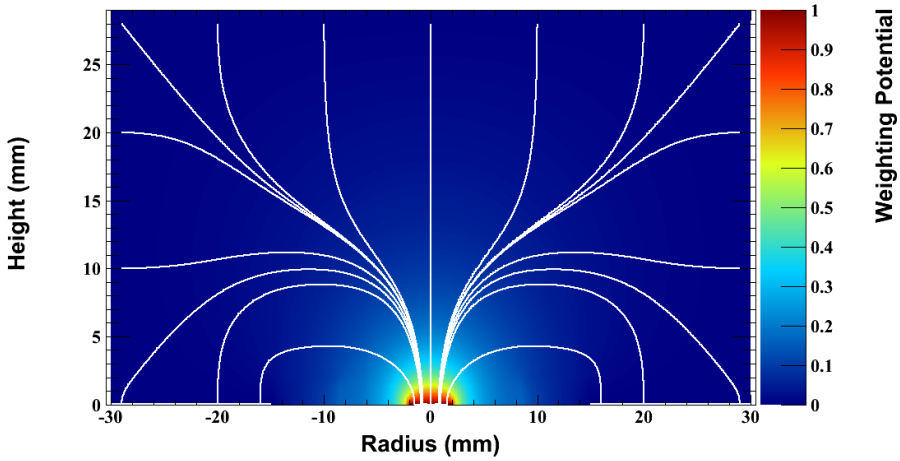

Figure 3.1: Weighting potential within a PPC detector. The color intensity shows the magnitude of the weighting potential throughout the bulk of the detector. The white lines show calculated hole drift paths. The weighting potential and drift paths were calculated using M3DCR [43] and SigGen [44]. Figure is from [33].

In contrast, the geometry of a p-type point contact (PPC) detector results in a weighting potential that is small throughout the bulk of the crystal and strongly localized about the point contact. An example calculation of the weighting potential for a PPC geometry is shown in Figure 3.1. Because of the sharply peaked potential, charges moving within the crystal induce most of their signal when they are very close to the point contact. Another consequence of the PPC geometry is that the drift time, the time it takes for a hole in the detector bulk to drift to the detector electrode, varies widely as a function of position, ranging from a few 100 ns to upwards of 1 μs at points furthest from the p^+ contact. This

means that holes created at different locations within the crystal may arrive at the point contact at varying times. These two features, a sharply peaked weighting potential and position dependent drift times, result in signal shapes that vary markedly with event type.

Figure 3.2 shows an example of the varying signal shapes seen using a PPC detector. A gamma-ray that Compton scatters within the detector can deposit energy in two or more locations. The charge created at each interaction point may reach the high weighting potential region of the detector at different times, inducing current signals on the electrode that can be resolved in time, as seen in panel (b). A gamma-ray that is photoelectrically absorbed within the detector, depositing all of its energy in a single location, will induce a single discrete current signal, as seen in panel (a). The dependence of signal shape on interaction position in PPC detectors can be used to distinguish multi-site events from single-site events, a valuable background rejection technique when searching for a single-site event like neutrinoless double-beta decay in the presence of gamma-ray backgrounds.

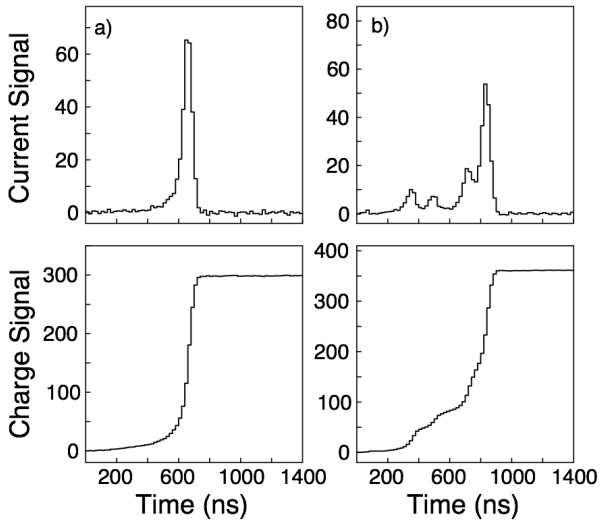

Figure 3.2: Current (top) and charge (bottom) signals from a single-site (a) and multi-site (b) event in a PPC detector. The single-site event current signal is a single peak, resulting in an integrated charge signal with a smoothly rising edge. The multi-site event current signal has multiple distinct peaks, caused by the different arrival times of holes at the high field region near the point contact. This creates a charge signal with kinks in the rising edge. Figure is adapted from [11].

Section 3.2: Surface Events in PPC Detectors

The n^+ contact of a PPC detector is created by depositing lithium on the surface of the detector and diffusing it into the crystal lattice, resulting in an approximately 0.5 - 1 mm thick region of n^+ material extending from the surface into the bulk of the detector. Because of the high impurity concentration in this region, much of the n^+ contact volume remains un-depleted when the detector is biased. For many PPC detector applications, e.g. gamma-ray spectroscopy, where relevant energies often don't fall below 30 keV, this layer is assumed to be entirely inactive when determining the absolute efficiency of the detector to a given photo-peak. In low-background applications, the inactive layer has the desirable property of preventing alpha radiation from the ^{232}Th and the ^{238}U decay chains from entering the detector bulk [45].

In reality, the surface region of the crystal is not entirely inactive. Some fraction of the charge created by an interaction within the n^+ layer can diffuse into the depleted region of the detector and induce a signal in the same manner as a bulk interaction. The amplitude of the signal will only reflect the fraction of initial charge carriers that move into the depletion region, and the full energy of the originating interaction will be lost. Because of this, surface layer events can populate all energies below the full energy of the original interaction.

Spectra showing 40 days of data collected with MALBEK, both before and after the removal of the lead shims described in Section 2.3, are shown in Figure 3.3. The basic data selection cuts described in Section 2.4.2 have been applied to both spectra. The data collected with the lead shims in the cryostat shows a significant peak at 46.5 keV from ^{210}Pb and a roughly exponentially increasing population of events at low energies. The events in this continuum are hypothesized to be energy degraded signals caused by ^{210}Pb gamma-rays, x-rays, and bremsstrahlung interacting in the surface region of the detector. The 40 day spectrum collected after removal of the lead shims shows a factor of 10 decrease in both the 46 keV peak and the continuum of surface events.

Figure 3.3 demonstrates that surface events can present a significant background, partic-

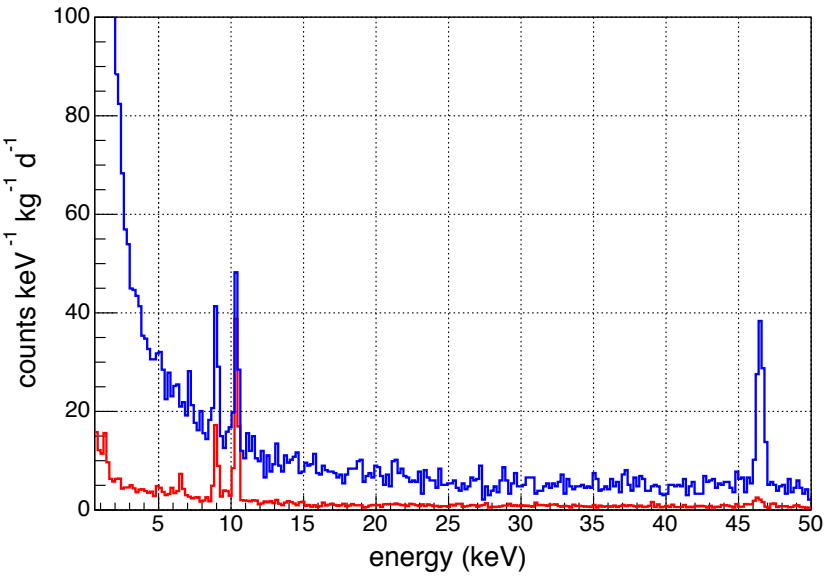

Figure 3.3: Comparison of energy spectra before (blue) and after (red) the removal of lead shims containing relatively high levels of ^{210}Pb from the cryostat. The 46.5 keV ^{210}Pb gamma-ray peak is clearly present in the pre-shim removal energy spectrum along with an increased number of events at low energies caused by interactions occurring near the surface of the detector. The post-shim data shows a factor of 10 reduction in the 46.5 keV line and correspondingly fewer events at low energies.

ularly at energies below 10 keV. This is the energy region most important for the single-site time correlation cut described in Section 1.2 and for many of the other rare-event searches possible with PPC detectors described in Chapter 5. Perhaps most troublesome, is that the distribution of energy degraded events decreases exponentially with energy, the same shape as the signal expected from WIMP-nuclear scattering. This is illustrated in Figure 3.4, which shows the similarity of the expected signal from a 15 GeV WIMP in a HPGe detector and the 40 day spectrum collected with the MALBEK detector while lead shims were in the cryostat. Figure 3.4 demonstrates the importance of identifying and removing surface events from data prior to performing an analysis, particularly when the expected signal closely resembles the surface event distribution. It is equally important to characterize both the acceptance and the rejection efficiencies of a cut designed to remove the surface events. With no a priori expectation for the surface event distribution from a source, this becomes difficult, particularly for events with low energies whose amplitude is comparable to the electronic noise

present on the waveform. The remainder of this chapter will discuss various techniques for identifying surface events and evaluating the acceptance and rejection efficiencies of surface event removal cuts.

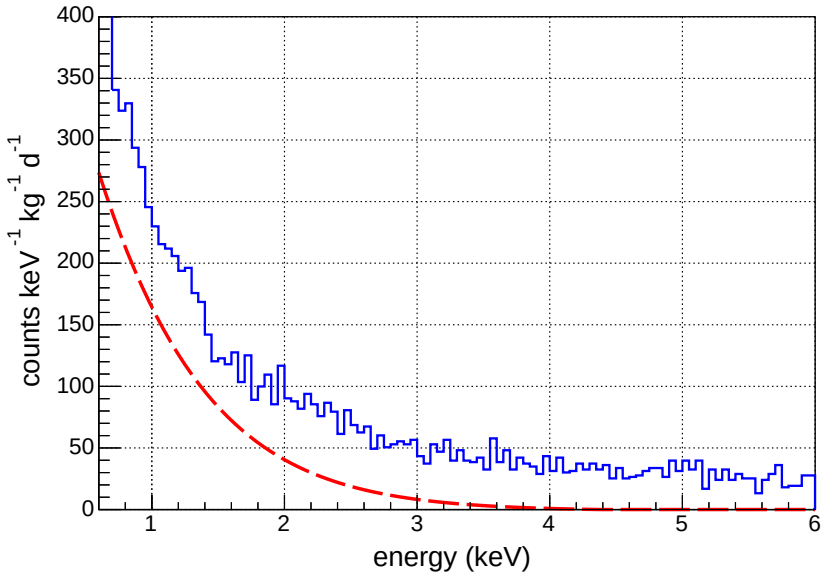

Figure 3.4: Expected signal from 15 GeV WIMPs recoiling from Ge nuclei (red dashed) and a spectrum from 40 days of data taken with the MALBEK detector with lead shims in the cryostat. The spectrum and expected WIMP signal exhibit similar shapes. The MALBEK events in this region are primarily due to the large surface event background from ^{210}Pb gamma-rays and x-rays interacting near the n^+ contact.

Section 3.3: Surface Event Identification

There is no electric field within the un-depleted surface layer of the detector to influence the trajectory of charge, so electrons and holes within this region move only due to diffusion. Results from a simple 2D model of the movement of a charge cloud within a 1 mm deep surface layer is illustrated in Figure 3.5. Charges are placed at varying distances from the detector's surface and allowed to diffuse, and the fraction of the total charge that reaches the boundary between the surface layer and the depleted region of the detector is recorded at 1 ns intervals. In this diffusion only model, it can take many microseconds for holes created in the surface layer to reach the bulk of the detector and induce a signal on the

electrode, resulting in charge signals that take several microseconds to reach their maximum value. This is in sharp contrast to events that occur in the bulk, where all holes are collected through the high field region in several hundred nanoseconds. The difference in the event rise-time, the time it takes the charge signal to reach its maximum value, can be used to distinguish bulk events from surface events and, ultimately, remove surface events from the dataset.

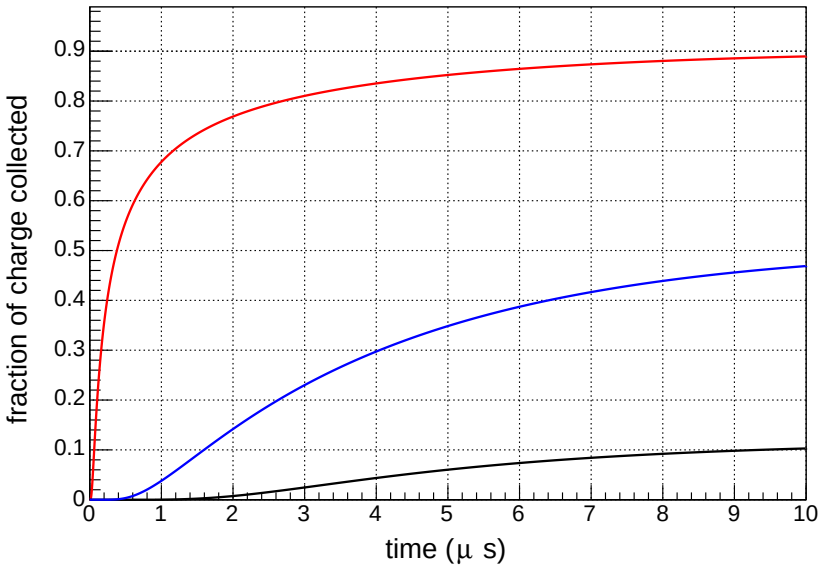

Figure 3.5: Fraction of the charge reaching the surface-bulk boundary as a function of time for a 2D model of a 1 mm deep surface layer. Charges are initially deposited at depths of 0.1 mm (black), 0.5 mm (blue), and 0.9 mm (red). It takes several microseconds for charge to diffuse into the bulk, resulting in charge signals with long rise-times. For a more complete discussion of slow event formation and modeling, see Chapter 4.

The phenomenon illustrated in Figure 3.5 can be clearly seen in events collected with the MALBEK detector. Figure 3.6 shows a charge waveform from a 40 keV event that likely occurred in the bulk and a 40 keV event that likely originated near the detector surface. The surface event takes over 3 μs to reach its maximum value, while the bulk event does so in about 500 ns. Two methods of rise-time determination will be discussed, t_{10-90} and w_{par}.

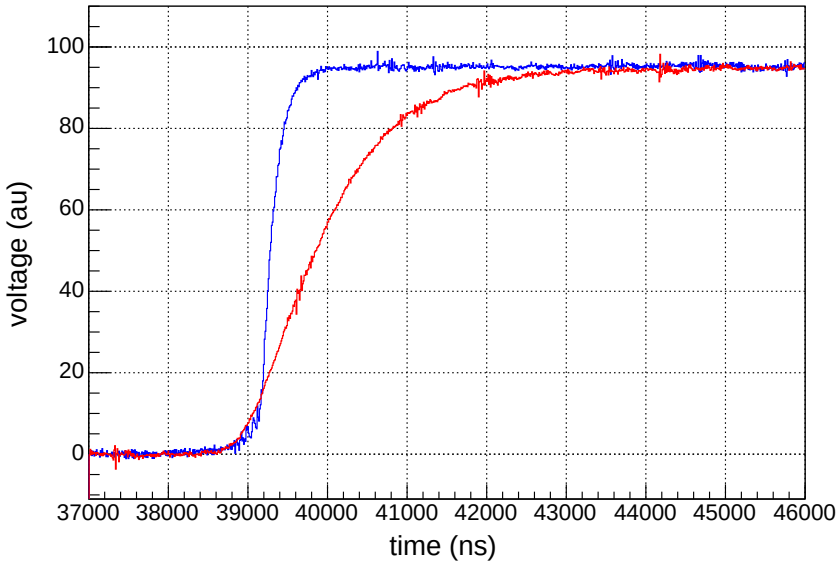

Figure 3.6: Waveforms from a 40 keV bulk event (blue) and a likely 40 keV surface event (red). The surface event takes over 3 μs to reach its maximum value. The bulk event reaches its maximum value in approximately 500 ns.

3.3.1: t_{10-90} Rise-time

A straightforward method for determining the rise-time of an event is to calculate the time it takes the charge signal to rise from 10% to 90% of its maximum amplitude, t_{10-90} [31, 46]. This is done by determining the maximum and minimum amplitude of the charge pulse, then scanning along the waveform to find the points at which the waveform rises by 10% and 90% of the maximum. This method performs well when the signal-to-noise ratio is high, but can be inaccurate as the signal amplitude decreases. An example of this is shown in Figure 3.7, which shows the difference in the rise-time calculated for a set of waveforms when the 10% and 90% points are found by scanning away from the mid-point of the waveform and when the 10% and 90% points are found by a scan starting at the beginning and the end of the waveform.

The failure to correctly determine t_{10-90}, as demonstrated in Figure 3.7, is often a symptom of noise fluctuations on the signal caused by microphonics or other electronic noise. Figure 3.8 shows a 3.2 keV waveform where the rise-time calculation described above has

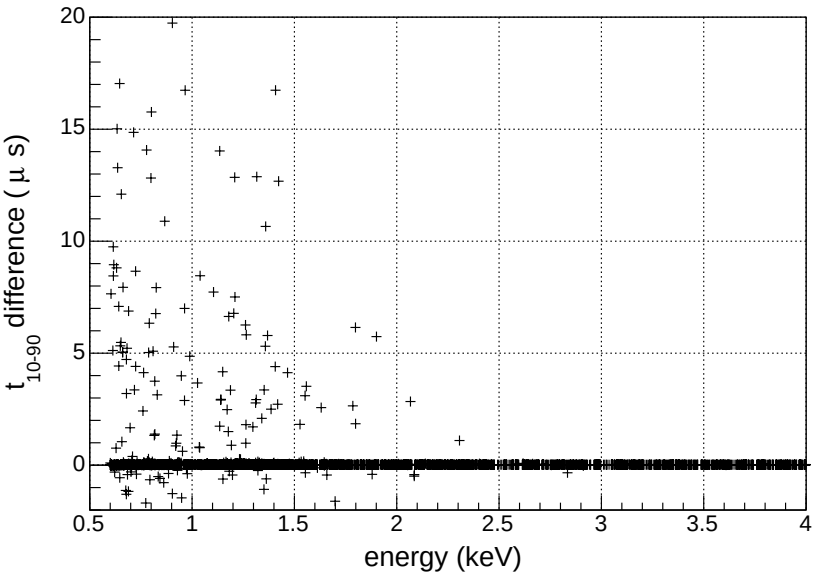

Figure 3.7: The difference in the calculated rise-time using two methods as described in the text for finding the 10% and 90% of maximum points as a function of energy. Above 2 keV, there is no difference in the calculated rise-time between the techniques. As the signal-to-noise ratio decreases below 2 keV, the two rise-time calculation techniques give different results. Between the 0.6 keV threshold and 0.8 keV, almost 50% of the waveforms have inconsistent t_{10-90} calculations.

failed because of a noisy feature occurring at 38,500 ns. In this case, it is necessary to perform some sort of digital filtering to remove the noise from the waveform while leaving the frequencies relevant for the rise-time calculation intact. A commonly used method for removing noise from a signal without broadening its features is wavelet denoising, also known as wavelet thresholding [47–50].

Wavelet denoising and its application to signals from a PPC detector is described in detail in [51]. In brief, wavelet denoising removes noise from a signal by decomposing the waveform into the time-scale domain via a wavelet transformation, thresholding the decomposed waveform to remove noise components, and transforming the waveform back into the time domain using an inverse wavelet transform. There are numerous choices that must be made when performing wavelet denoising, including which wavelet basis, transform, and thresholding technique to use. The wavelet denoising performed here will follow the prescription used in [33] and utilize the `PyWavelets` package [52]. A discrete stationary wavelet trans-

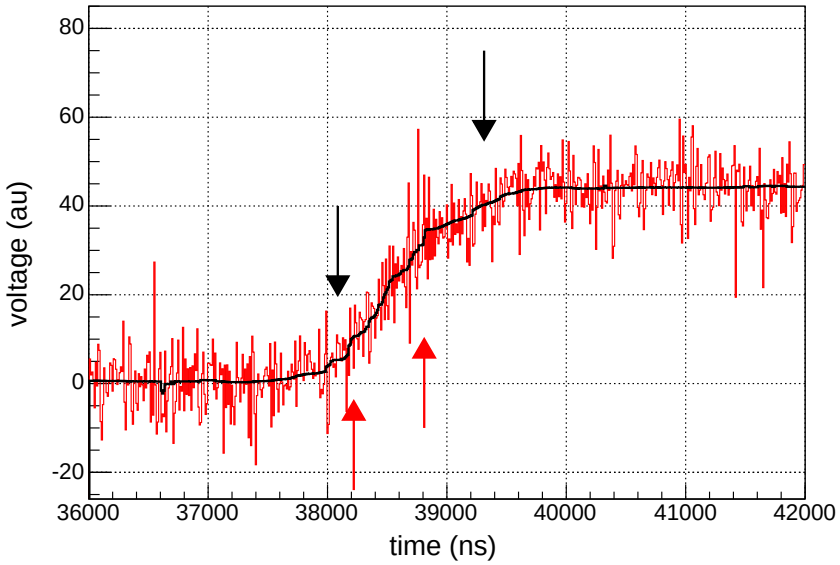

Figure 3.8: A 3.2 keV waveform (red) and the same waveform after wavelet de-noising (black). Arrows indicate the t_{10} and t_{90} times calculated using the raw waveform (red) and the de-noised waveform (black). The t_{90} calculated using the raw waveform is incorrect due to noise on the rising edge of the signal.

form (DSWT) is used for the forward and inverse waveform transformation. The DSWT is translation invariant and eliminates artifacts caused by alignment between the signal and the basis wavelet, a common problem in schemes that utilize the discrete wavelet transform (DWT) [53]. Eight levels of the DSWT are performed on MALBEK waveforms. The choice of the optimum level for denoising depends on the signal and noise characteristics of the data and is best found through experimentation. A favorable waveform basis is selected by maximizing the cross-correlation between the wavelet and the signal. In this analysis, a Haar wavelet is used as a mother wavelet due its close resemblance to a PPC signal. Hard thresholding is performed on each level of decomposed waveform following [48] and defining the threshold values using a set of pure noise events collected by randomly triggering the data acquisition systems. The literature on wavelet theory and wavelet denoising is vast. Some useful texts on the subject are [54–56].

Figure 3.8 shows a wavelet denoised signal in black overlaid on the original, unfiltered waveform in red. The calculated t_{10-90} of the denoised waveform, indicated in the figure by

black arrows, doesn't suffer the same noise sensitivity as the t_{10-90} calculation performed on the original waveform and more accurately reflects the true rise-time of the event. While wavelet denoising improves the performance of the t_{10-90} calculation, it is not a panacea. Figure 3.9 shows the t_{10-90} calculation performed on a set of events generated using the waveform generator and attenuator system described in Section 2.2. Events in this dataset have a t_{10-90} time of about 450 ns and span energies from 300 eV to 6.7 keV, providing a useful means of testing the efficacy of rise-time determination techniques around the 600 eV detector threshold. As the signal-to-noise decreases, so does the accuracy of the t_{10-90} calculation of the denoised waveforms. Below 3 keV, the rise-time calculation behaves unpredictably, rendering the t_{10-90} time ineffective as a means to distinguish surface from bulk events. With this result in mind, efforts were made to define a parameter correlated with the event rise-time but less sensitive to noise.

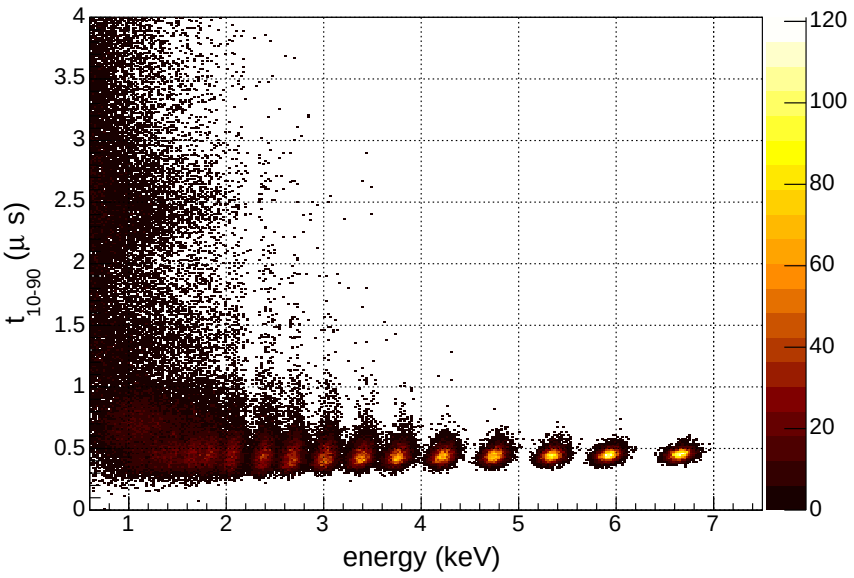

Figure 3.9: t_{10-90} versus energy for a dataset generated using an arbitrary waveform generator. The test signal is stepped down in amplitude in discrete intervals from 6.7 keV to below the detector threshold. All of the events have t_{10-90} rise-times of 450 ns, but as the signal-to-noise decreases around the detector threshold, the rise-time calculation fails to accurately reconstruct the t_{10-90} rise-time of the wavelet denoised waveforms.

3.3.2: w_{par}

Mallat's algorithm decomposes the wavelet transformation into a cascading series of filters [57]. At each level of the transformation, the signal passes through a set of high pass and low pass filters determined by the properties of the mother wavelet. The output of the low pass (integrating) filters are called approximation coefficients and reflect the gross properties of the waveform at the scale (frequency band) of the level. The output of the high pass (differentiating) filter are called detail coefficients and are sensitive to the higher frequency components at that scale. When performing a DWT, the approximation coefficients are down-sampled before being passed to the next level of filtering, while the DSWT passes the un-decimated approximation coefficients. This is a redundant scheme, but overcomes the translation variance of the DWT that can cause artifacts in the denoised waveform. A graphical representation of the DSWT is shown in Figure 3.10.

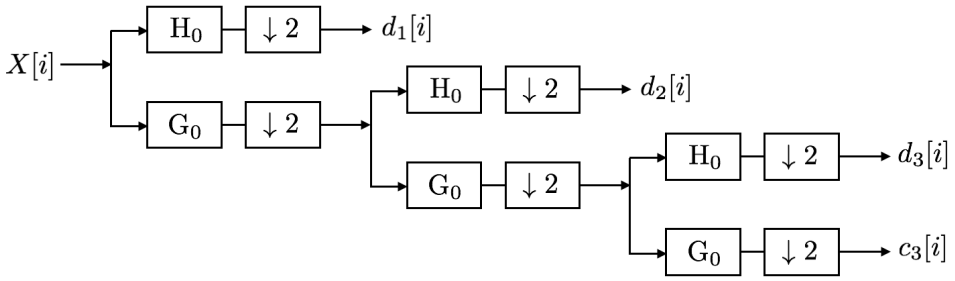

Figure 3.10: Block diagram representing a three level discrete stationary wavelet transformation (DSWT) of waveform $X[i]$. H_0 is a high pass filter block resulting in detail coefficients $d_n[i]$, where n is the level of the filter, and G_0 is a low pass filter block resulting in approximation coefficients $c_n[i]$. The un-decimated approximation coefficients from level n pass to the level $n+1$ filters.

In [33], a parameter is developed that is sensitive to the rise-time of a waveform based on the detail coefficients calculated during the DSWT. The formal definition is

$$w_{par} = \max\left(|c_D^{(i)}(n=0)|^2\right)/E^2, \tag{3.2}$$

where $c_D^{(i)}(n=0)$ is the i^{th} first-level detail coefficient and E is energy of the event. The behavior of w_{par} is dependent on the specific choice of wavelet, the number of transform levels used, and the waveform sampling frequency. For MALBEK, the DSWT is an 8-level transformation using a Haar wavelet, so the level-1 coefficients are the average of 2^8 adjacent samples, or 2.6 μs of waveform, minus the average of the next 2^8 samples. $c_D^{(i)}(n=0)$ is effectively a smoothed derivative of the waveform. Taking the absolute value squared of $c_D^{(i)}(n=0)$ follows the convention for obtaining power spectra in frequency analysis and dividing by E^2 normalizes the squared derivative by its amplitude. The result is that w_{par} is simply a measure of the maximum slope of the waveform, smoothed, squared, and normalized. An example calculation of w_{par} is shown in Figure 3.11.

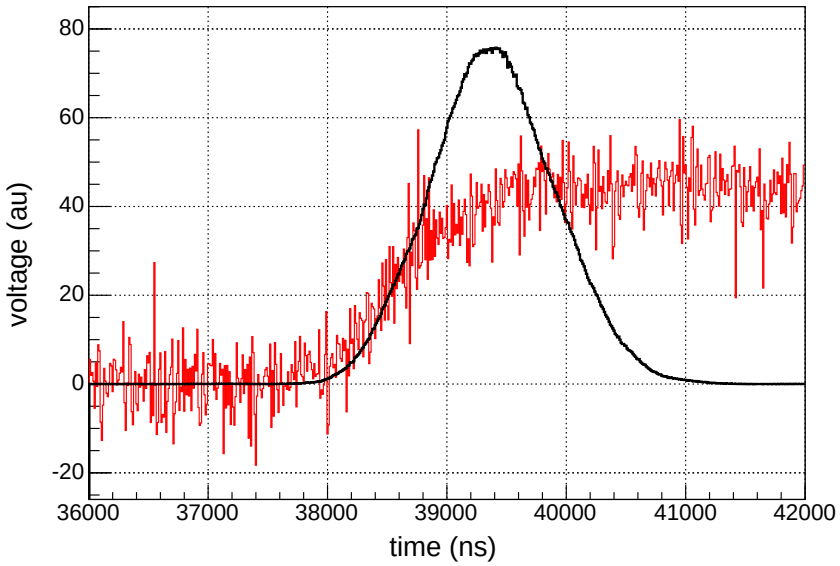

Figure 3.11: A 3.2 keV waveform (red), identical to the waveform show in Figure 3.8, and the first level detail coefficient power spectrum (black). The maximum value of the power spectrum normalized by the energy of the event squared (w_{par}) is used as an alternative calculation of the event rise-time.

Figure 3.12 shows the w_{par} distribution for the same set of waveform generator events shown in Figure 3.9. The spread in the distribution of the calculated w_{par} value increases as the signal-to-noise decreases, but, in contrast to t_{10-90}, it does so in a smooth, characterizable way. The waveform generator can generate waveforms with arbitrarily long rise-times.

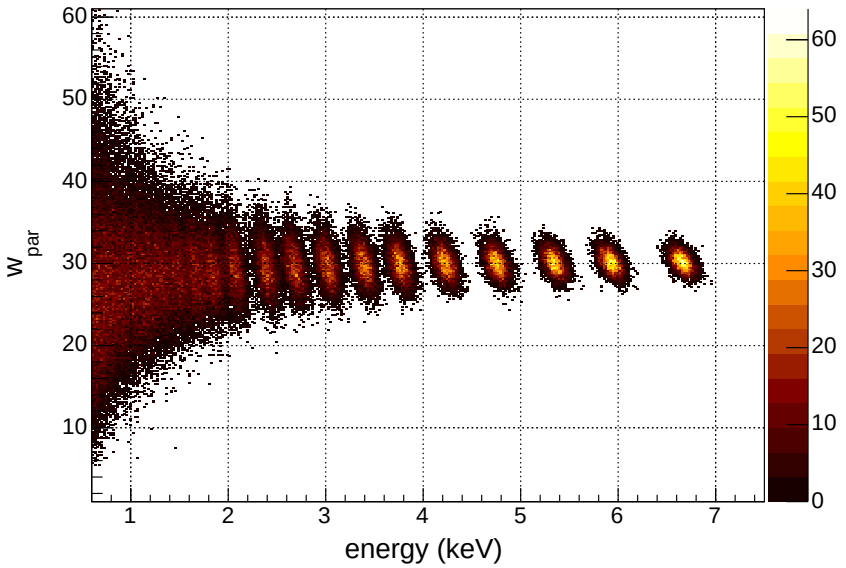

Figure 3.12: w_{par} versus energy for a dataset generated using an arbitrary waveform generator. All of the events have t_{10-90} rise-times of 450 ns. The spread in calculated w_{par} values increases with decreasing energy, but does so in a way that is more easily characterized than the t_{10-90} distribution shown in Figure 3.9.

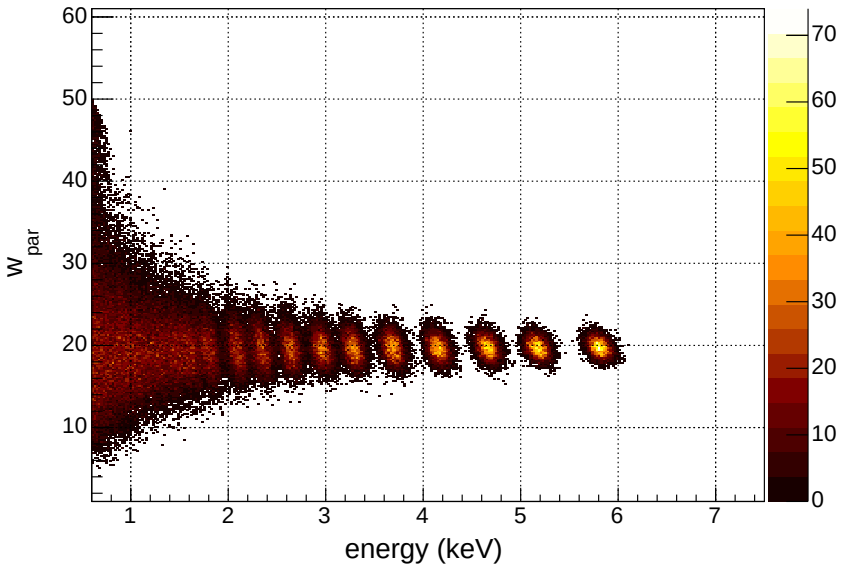

Figure 3.13: w_{par} versus energy for a dataset generated using an arbitrary waveform generator. All of the events have t_{10-90} rise-times of 1100 ns.

Figure 3.13 shows the w_{par} distribution for a set of waveform generator events with t_{10-90} rise-times of 1100 ns. The shape of the distribution is similar to Figure 3.12, but the mean w_{par} value is lower. The remainder of the analyses described here will utilize w_{par} to evaluate the rise-time of events. It is important to note that w_{par} is not the inverse rise-time, although they are clearly related in a manner that is dependent on the detailed shapes of the waveforms produced by the detector. However, they need not be related in the first place. The only requirement for this analysis parameter is that it separates bulk from surface events. Figure 3.14 shows the t_{10-90} value and the w_{par} value calculated for events collected using the MALBEK detector with lead shims in the cryostat. Above 2.5 keV, w_{par} is clearly sensitive to the rise-time of the event. Below 2.5 keV, the poor performance of t_{10-90} makes a comparison to w_{par} uninformative. Section 3.4 will describe the performance of w_{par} in the lowest energy regime and discuss how w_{par} can be used to remove surface events with slow rise-times from a dataset.

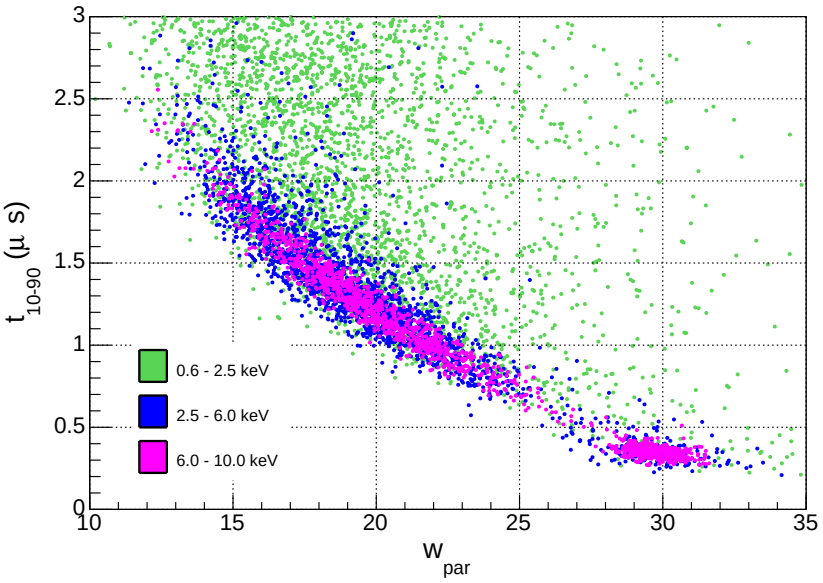

Figure 3.14: t_{10-90} versus w_{par} for events in three different energy regions. These data were collected with lead shims in the detector cryostat. Between 6.0 and 10.0 keV (violet) there is a clear correlation between event rise-time and w_{par}. The same is true between 2.5 and 6.0 keV (blue). Below 2.5 keV, there is no correlation between the rise-time calculation techniques due to the poor performance of the t_{10-90} calculation.

Section 3.4: Surface Event Removal

Before performing a search for a signal from new physics with a PPC detector, slow surface events, which can constitute a significant background, must be quantified or removed from the data. When there is overlap between signal events and background events, e.g. the region of the spectrum below 2 keV, there are two paths one could take to accomplish this. The first is to define a cut that maximizes the acceptance of bulk fast events, and hence the exposure of the detector, and then correct for any slow surface events that pass the cut criteria and contaminate the signal region of interest. The second option is to define a cut that more efficiently removes surface events, but necessarily does so at the expense of the fast event acceptance efficiency. In both approaches, failure to properly correct for the slow event contamination or the acceptance efficiency of fast events can artificially improve or reduce the sensitivity of the experiment, or, at worst, mimic the very signal one is looking for.

This section will examine the distribution of slow surface events and the effect of various cuts on populations of slow and fast events in different datasets, ultimately showing that a measurement of the signal acceptance efficiency is more accurate and reliable than a measurement of the background leakage. Bulk signals have a more-or-less universal shape that can be mimicked with a waveform generator or using attenuated data, and the evaluated signal efficiency can be cross-checked using known spectral features, such as the stability of the L-shell line strength as a function of the cut. Measuring background leakage, on the other hand, requires a good model of or proxy for the various populations of background sources in this energy range, which are difficult to obtain.

3.4.1: Surface Event Distributions From Varying Sources

It is useful to examine the rise-time distribution of different datasets to understand how various spectral features contribute to the slow event continuum. Three datasets will be

presented in this section. The first is 40 days of data collected with a ^{210}Pb source inside of the cryostat, the second dataset is a thirty minute run taken with an uncollimated ^{241}Am calibration source positioned directly above the cryostat on-axis with the detector, and the last dataset consists of 89.5 kg-d of shielded exposure used for the analyses presented in Chapter 5.

Figure 3.15a shows the w_{par} distribution for events in the 0.6 keV to 50 keV energy range for the 40 day lead source dataset. Figure 3.15b shows data over the same energy range collected during an equivalent exposure time after the lead shims were removed. Energy spectra from these datasets were previously shown in Figure 3.3. The number of events in the 46 keV ^{210}Pb peak are reduced by an order of magnitude in Figure 3.15b. The same reduction is seen in the band of slow events with w_{par} values less than 30, demonstrating that radiation, in this case external 46 keV gamma rays, lead x-rays ranging from 70 to 90 keV, and lead bremsstrahlung interacting near the detector surface populate the slow event continuum down to the detector energy threshold. Events that are postulated to occur near the detector surface have both longer rise-times and lower signal amplitudes, consistent with the simple model of charge diffusion shown in Figure 3.5. Below 2 keV, the slow event band bleeds into the fast event region. This contamination must be accommodated when performing a slow event cut based on w_{par}.

The w_{par} distribution for data collected with an uncollimated ^{241}Am source illuminating the detector from above the cryostat is shown in Figure 3.16. 36% of ^{241}Am decays emit a 59.5 keV gamma ray that, if it penetrates the detector cryostat, has a high probability of depositing its energy within a millimeter of the detector surface and generating a slow surface event. Due to the short run exposure and the low background rate, the vast majority of events in this dataset in the energy region below 12 keV are due to surface events from 59.5 keV gamma rays. The slow event distribution in Figure 3.16 has a qualitatively different shape than the slow events observed in Figure 3.15. This is presumed to be due to the difference in the penetration depth of the gamma rays generating the surface events and the gamma

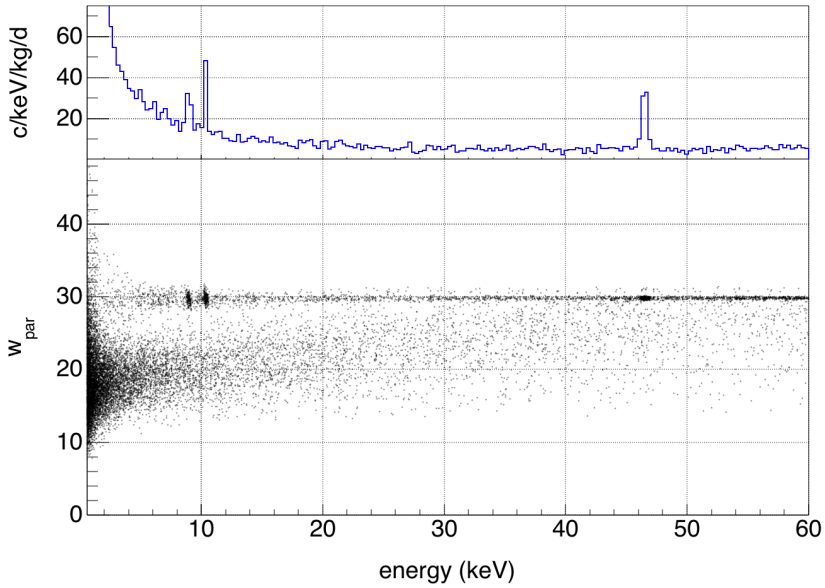

(a)

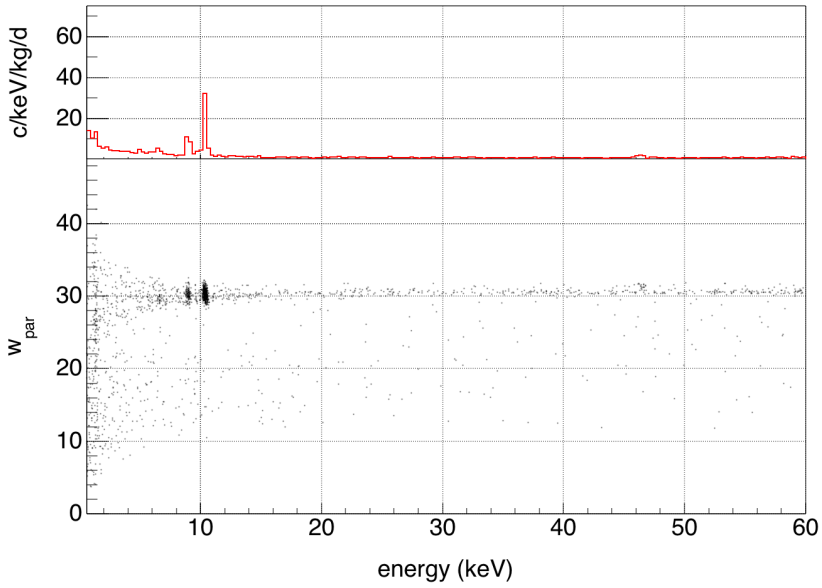

(b)

Figure 3.15: w_{par} distributions for 40 days of data taken before (a) and after (b) removal of the ^{210}Pb contamination in the cryostat. In (a), the continuum of slow events is due 46 keV gamma-rays and lead x-ray lines between 70 keV and 90 keV interacting near the detector surface. In (b) the peak strength and the slow event continuum is reduced by an order of magnitude.

ray source's position relative to the crystal. The band of slow events with w_{par} values less than 30 are clearly separated from the fast event population at 10 keV but bleed into the fast pulse region at energies less than 2 kev. This is further illustrated by the two curves in Figure 3.16. The solid red line is defined such that 99% of fast rising events generated with the pulser fall above the line. The solid green line is defined so that 99% of the events in the ^{241}Am dataset fall below the line. Assuming the majority of events in the ^{241}Am dataset below 12 keV are energy degraded surface events, the solid green line is an approximation of where one would place a cut to efficiently remove slow events. There is a significant region below 2.5 keV where events fall below the slow event rejection curve and above the fast pulse acceptance curve. Events in this region are ambiguously defined. Again, any cut that is designed to retain fast events from this region must correct for slow event leakage into the signal region.

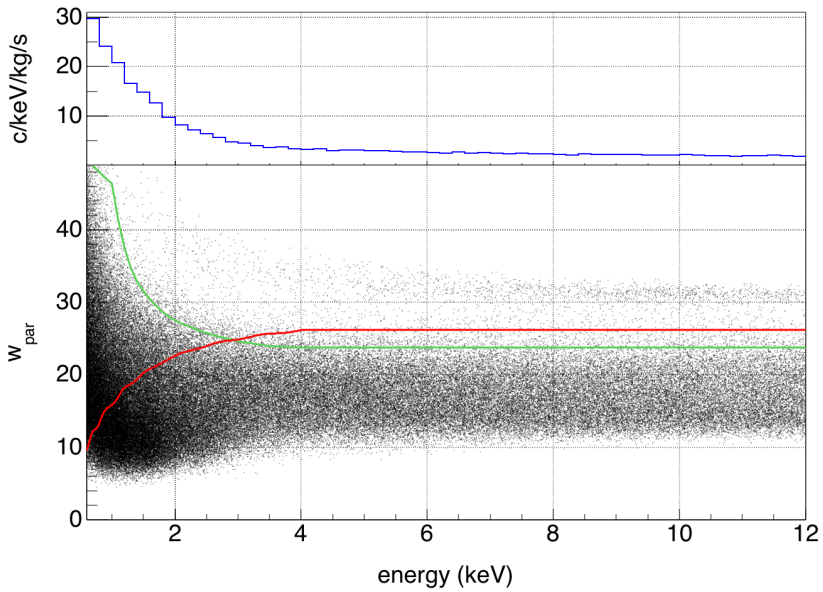

Figure 3.16: w_{par} versus energy for a flood measurement using an ^{241}Am source. All events falling above the solid red curve pass a rise-time cut built to retain 99% of fast pulser data. Events falling below the solid green curve fail a cut designed to remove 99% of the ^{241}Am data. Between the two curves is an ambiguous region containing events identified as both surface and bulk events.

Figure 3.17 shows the w_{par} distribution for an 89.5 kg-d shielded exposure. The ^{65}Zn K-

shell capture (9.0 keV), ^{68}Ga K-shell capture (9.7 keV), and ^{68}Ge K-shell capture (10.4 keV) lines are visible as tight clusters around w_{par} values of 30. The corresponding L-shell capture lines are visible around 1 keV, forming a vertical band. This band demonstrates the same spread in w_{par} value that is visible in the fast pulser data as the signal-to-noise ratio decreases towards the detector energy threshold. The 89.5 kg-d dataset has a smaller contribution from slow events than the lead shim or ^{241}Am datasets. Still, the contamination of the fast event region from the slow event continuum below 2 keV is visible in the figure.

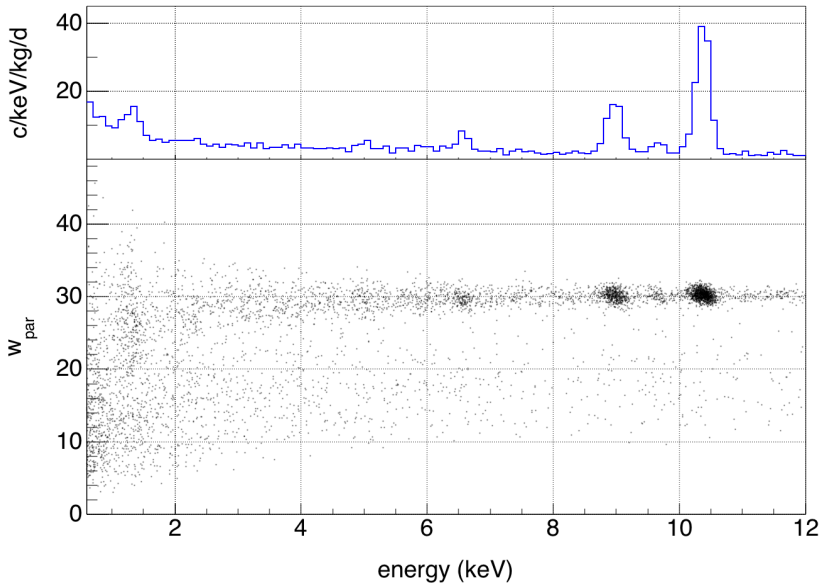

Figure 3.17: w_{par} versus energy for the 89.5 kg-d exposure dataset.

To better understand the differences in slow event populations from different background sources, it is instructive to examine w_{par} distributions within a fixed energy window. Figure 3.18a shows the distribution of w_{par} values for events falling between 0.6 keV and 0.9 keV for the ^{241}Am source data, lead shim data, 89.5 kg-d exposure, and the fast waveform generator dataset. In this energy region, spanning from the detector threshold to 3σ below the ^{65}Zn L x-ray line, the three physics datasets consist mostly of slow events. The slow event distributions exhibit significantly different shapes, highlighting the difficulty in defining the acceptance and rejection efficiencies for a surface event cut without knowledge of the surface event sources and distributions. As expected, at these low energies, the fast pulser dataset

has significant overlap with slow events.

Figure 3.18b shows the energy region from 0.9 to 1.6 keV. In this region, the 89.5 kg-d dataset includes fast events from the L-shell capture peaks. Figure 3.18c shows the energy region between 1.6 keV, 3σ above the ^{68}Ge L line, and 3.6 keV. In both of these energy regions, the mostly slow lead and ^{241}Am data are better separated from the fast pulser data than in Figure 3.18a. Again, the slow event distributions from the three physics datasets have distinctly different shapes. In Figure 3.18b, the fast event distribution from the 89.5 kg-d dataset is skewed lower in energy than the pulser dataset. This is due to the larger fractional contribution in the 89.5 kg-d dataset from fast events from the L-line peaks around 1 keV, where the median fast event value is lower, and because the pulser dataset is collected at discrete energies, not from a variation in the fast event distribution. The same phenomenon is seen in Figure 3.18c, the fast event distributions from the pulser and lead data are centered around w_{par} of 31 while the 89.5 kg-d dataset fast event peak is skewed slightly lower in w_{par}.

Figure 3.18d and 3.18e restricts the energy region to be between 3.6 keV and 12 keV. With the lower energy data removed, the waveform generator, lead, and ^{241}Am fast event distributions have comparable positions and widths and are well separated from the slow event distributions. Figure 3.18f shows events that fall between the detector threshold and 12 keV. This energy range contains the K-lines clustered around 10 keV. The larger width of the waveform generator fast event distribution relative to the physics data distributions is expected because the majority of fast events in the physics datasets are in the K lines, where w_{par} values shows a clear distinction between slow and fast events.

The variation in the energy and w_{par} distribution of surface events illustrates how difficult it can be to accurately determine the number of slow events that pass a cut designed to maximize the detector efficiency. Other collaborations using PPC detectors for low-mass WIMP searches have adopted different methods for accounting for the slow event leakage into their signal region, and these will be discussed in Section 3.4.4. The next section will investigate an alternative approach, defining a cut that maximizes the efficiency of slow

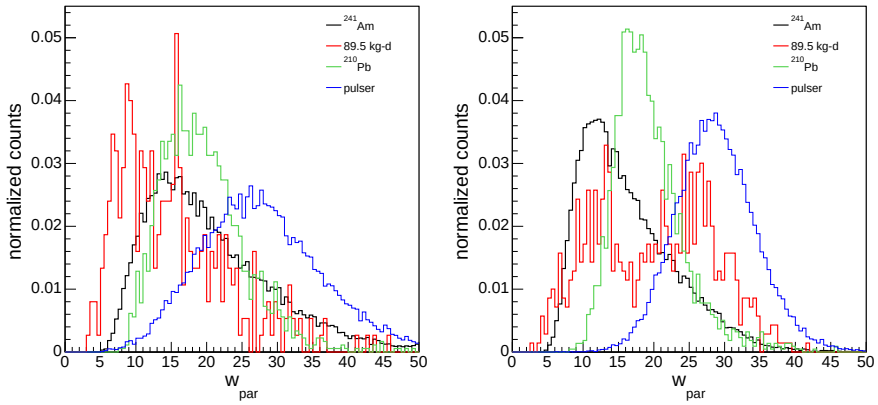

(a) 0.6 – 0.9 keV (b) 0.9 – 1.6 keV

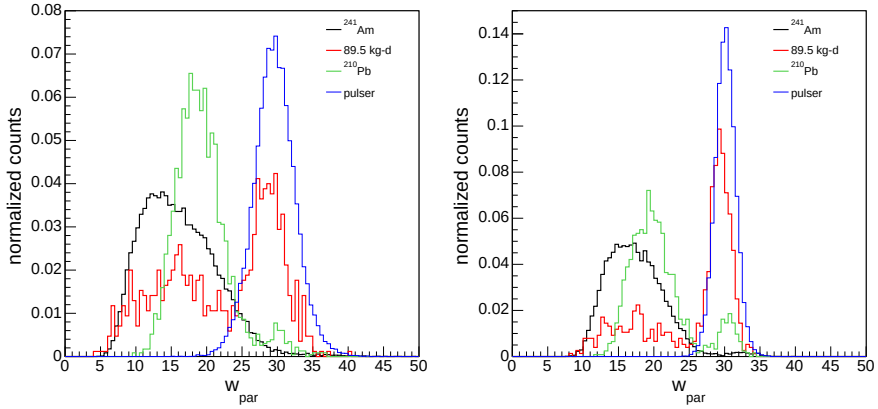

(c) 1.6 – 3.6 keV (d) 3.6 – 6.0 keV

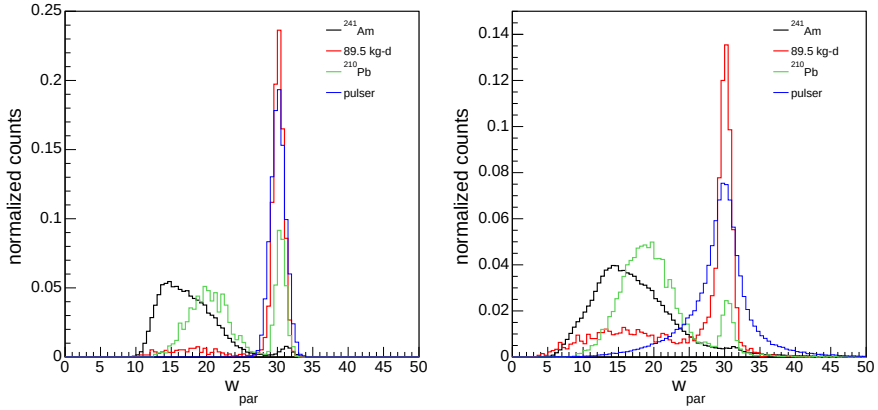

(e) 6.0 – 12.0 keV (f) 0.6 – 12.0 keV

Figure 3.18: Distributions of w_{par} values for events from the ^{241}Am source data (black), lead shim data (green), fast waveform generator data (blue), and 89.5 kg-d shielded exposure (red). The total counts in each distribution are normalized to one. In all figures, the minimum w_{par} value of the lead shim distribution is higher than the minimum value of the ^{241}Am and 89.5 kg-d distributions. This is due to a higher threshold during the lead shim data taking that decreased the trigger efficiency for very slow events.

event removal, then correcting for the decrease in signal acceptance efficiency using known fast event populations.

3.4.2: Fast Event Survival as a Function of Cut Position

The validity of a w_{par} cut and the subsequent efficiency correction can be verified by examining its effect on populations of events with known rise-times. These populations are available not just from data generated using a pulser, but from well understood physical features within the dataset. For example, events that occur in the K and L-shell capture peaks around 1 and 10 keV are fast rising bulk events. The number of events remaining in these populations after a w_{par} cut and signal acceptance efficiency correction should remain constant. As shown in Figure 3.16, most events that occur between the 1 keV peak and the detector threshold in the ^{241}Am dataset are slow surface events, so the number of events remaining in this energy region after a rise-time cut should decrease with increasingly strict cut values.

Three datasets were used for this study, the flood ^{241}Am source measurement, 40 days of data collected with lead shims inside of the cryostat, and 89.5 kg-d of data collected within the shield once the lead patches were removed. The w_{par} cuts used for this study are constant with energy, resulting in a fast event acceptance efficiency that drops off with decreasing energy. The acceptance efficiency of a given w_{par} cut value is calculated using a set of fast pulser generated signals. For each of the three datasets, constant w_{par} cuts were applied with values ranging from 10 to 31 and the resulting spectra were efficiency corrected. Beyond a w_{par} cut value of 31, the acceptance efficiency of the cut drops off rapidly. The resulting spectra were then fit with a flat Compton continuum, an exponential to parametrize the slow pulse contamination, and two gaussians at the ^{65}Zn (1.096 keV) and the ^{68}Ge (1.299 keV) L lines. An example fit to the 89.5 kg-d dataset and the fit residual are shown in Figure 3.19. The number of counts remaining the L-shell capture peaks are then extracted from the fit.

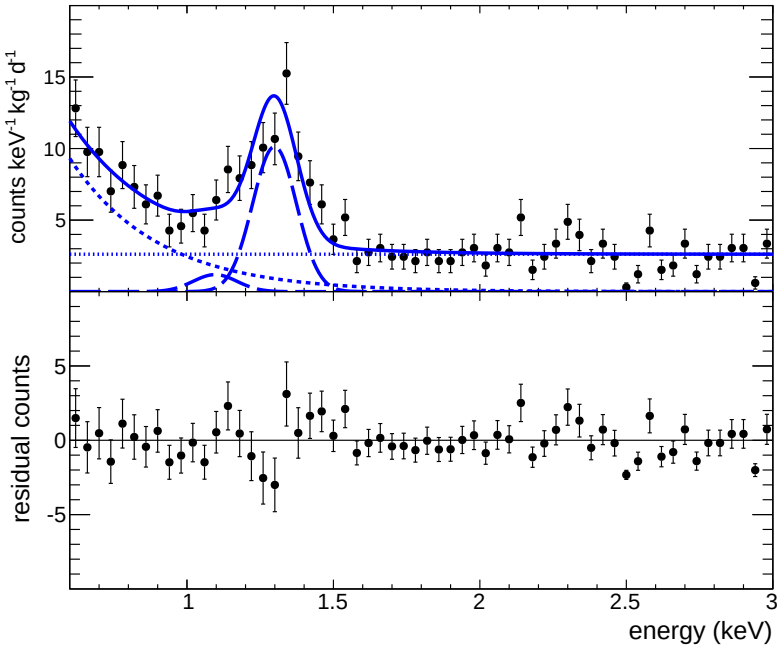

Figure 3.19: 89.5 kg-d spectrum after removing events with $w_{par} < 15$. Results from a fit to a flat Compton continuum (dotted), an exponential to parametrize the slow pulse contamination (dashed), and two gaussians (long dash) at the ^{65}Zn (1.096 keV) and the ^{68}Ge (1.299 keV) L lines are shown along with residuals of the fit.

The counts remaining in the ^{241}Am dataset as a function of the w_{par} cut value are shown in Figure 3.20. Below 60 keV, this dataset is composed primarily of slow events. The efficiency corrected counts remaining in the region from 0.6 to 0.9 keV decreases with an increasingly strict w_{par} cut value. This is the expected behavior in an energy region that is dominated by slow events. The same behavior is seen in the region from 1.6 to 3.6 keV. The efficiency corrected number of events decreases as a function of the w_{par} cut value, but this time only until a w_{par} cut value of 26 is reached. At this point, most of the slow events in the region have been removed and the remaining rate is due to fast events. The fact that the number of counts remains constant suggests that the efficiency correction is properly accounting for fast signal events removed by the cut. The two populations of events from the ^{241}Am data are shown in contrast to the combined counts remaining in the ^{65}Zn and ^{68}Ge lines extracted from the 89.5 kg-d dataset. The number of efficiency corrected counts in these peaks, which are all fast bulk events, remain constant with cut value, albeit with increasing uncertainty

due to larger efficiency corrections. These results demonstrate that the efficiency correction based on the fast pulser dataset is correctly weighting the remaining counts while the w_{par} cut is removing slow events.

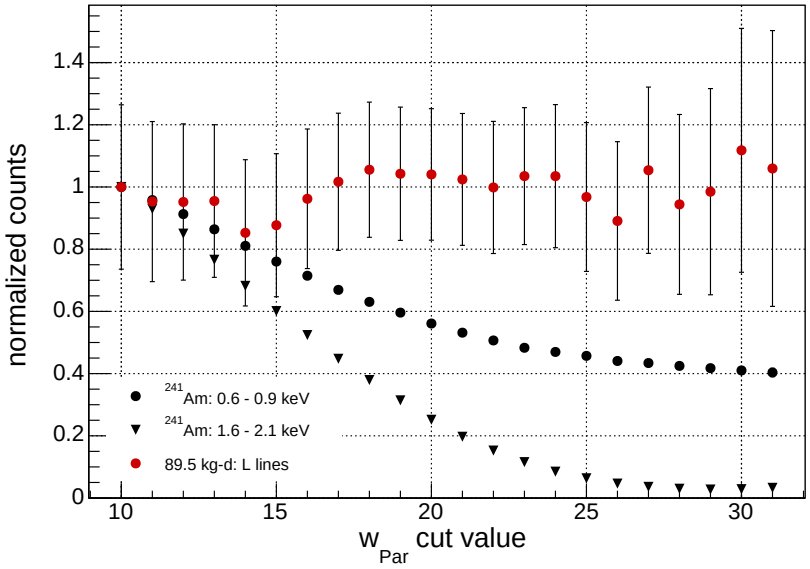

Figure 3.20: Counts remaining in the region from 0.6 to 0.9 keV (black circles) and 1.6 to 3.6 keV (black triangles) in the ^{241}Am source data as function of w_{par} cut value. The efficiency corrected counts in the 89.5 kg-d dataset L-shell capture peaks (red circles) remain constant as a function of the cut position. The error bars on the points include statistical uncertainty as well as uncertainty from the efficiency correction.

Figure 3.21 shows a similar analysis performed on the 40 days of data taken with lead shims inside the cryostat. Again, the number of counts in the region from $0.6 - 0.9$ keV drops with an increasingly strict cut. Because the w_{par} calculation doesn't perform as well at the lowest energies, not all of the slow events are removed, even when a w_{par} cut value of 31 is used. The counts in the region above the L lines decreases with increasing w_{par} and become constant at cut values greater than 25, when the majority of the slow events are removed. The counts in the L lines from the 89.5 kg-d dataset are shown in comparison.

Finally, Figure 3.22 shows the counts remaining between 0.5 and 0.9 keV as a function of w_{par} cut value for the 89.5 kg-d dataset. The number of counts in this region decrease until a w_{par} cut value of 25. At this point, most of the slow events have been removed from the data. This analysis shows that slow events are effectively removed with increasingly strict,

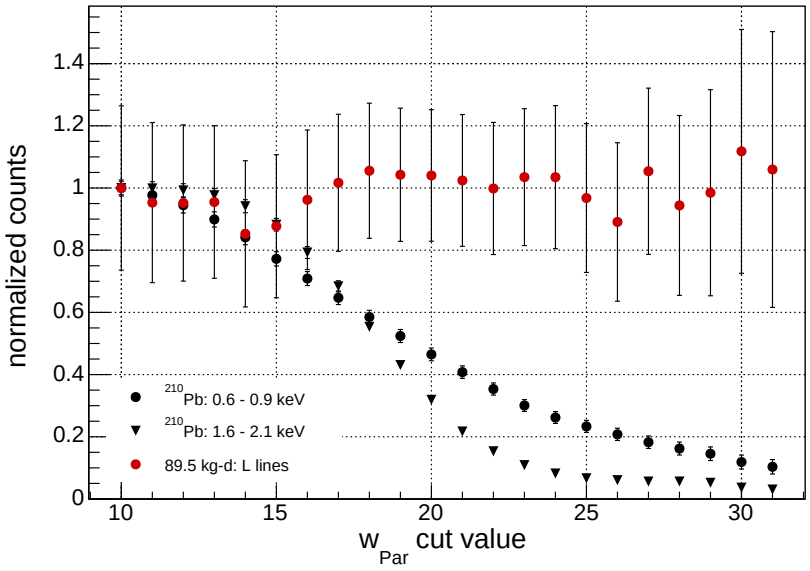

Figure 3.21: Counts remaining in region from 0.6 to 0.9 keV (black circles) and 1.6 to 3.6 keV (black triangles) in the lead source data as function of w_{par} cut value. The efficiency corrected counts in the 89.5 kg-d dataset L-shell capture peaks (red circles) remain constant as a function of the cut position.

constant valued w_{par} cuts, and that the efficiency correction calculated using the fast pulser dataset correctly accounts for the fast events removed by the cut.

3.4.3: Attenuated Waveform Study

An analysis similar to that described in Section 3.4.2 can be performed using higher energy waveforms that have been attenuated. At energies where the signal-to-noise ratio is high, the rise-time of waveforms can be reliably determined. These waveforms can then be digitally attenuated, combined with noise, and passed through the data analysis chain to recalculate an energy and w_{par} value. The resulting attenuated dataset consists of events with known rise-times at energies near the detector threshold, much like those generated using the waveform generator, but created by actual energy depositions in the detector. This dataset is another useful tool for checking the performance of the w_{par} based cut.

Waveforms from the 89.5 kg-d MABLEK dataset with energies between 24 and 84 keV were attenuated by a factor of 40. The unattenuated data are shown in Figure 3.23 and

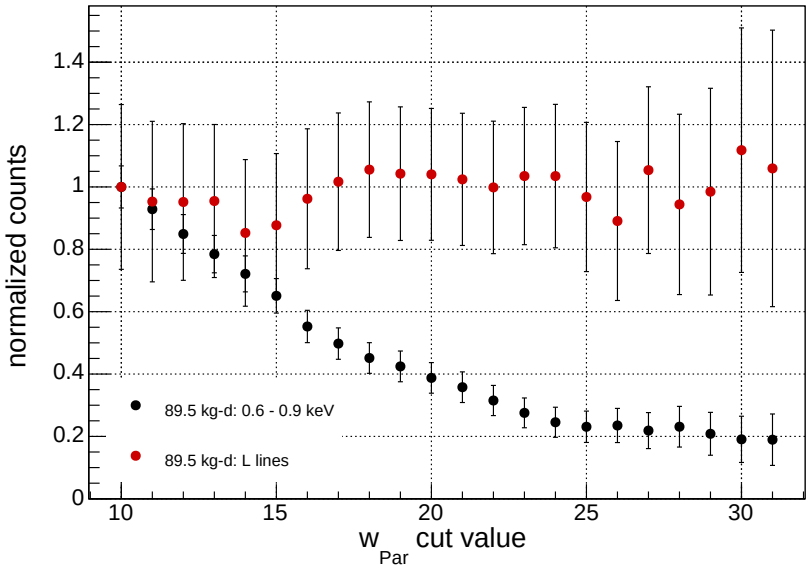

Figure 3.22: Counts remaining as function of the cut for three features in the 89.5 kg-d spectrum. The region from 0.6 to 0.9 keV (black circles) and the L-shell capture peaks (red circles).

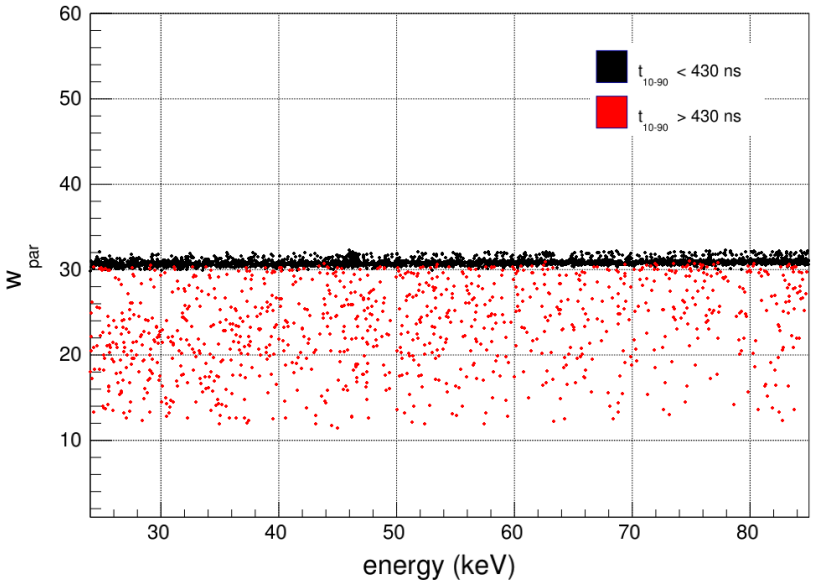

Figure 3.23: w_{par} versus energy for high energy data collected within the MALBEK shield. Events with t_{10-90} times less than 430 ns are shown in black. Events with t_{10-90} times greater than 430 ns are shown in red.

are colored based on their t_{10-90} rise-times. Fast events with t_{10-90} times less than 430 ns are shown in black. Slow surface events with t_{10-90} times greater than 430 ns are shown in red. To match the signal-to-noise ratio at the attenuated energy, noise is added to each signal. This was done by linearly combining every attenuated waveform with a pure noise waveform collected by force triggering the low energy channel of the SIS3302 digitizer. The force trigger waveforms were collected at several times throughout the 89.5 kg-d data taking period to more accurately reflect the noise characteristics of the system over time. The existing noise on the attenuated waveform, now 40 times smaller, is assumed to contribute negligibly. The attenuated data with added noise are then passed through the same data processing stream used to process raw data collected from the detector. The resulting w_{par} versus energy distribution is shown in Figure 3.24. Events with t_{10-90} rise-times greater than 430 ns calculated from the unattenuated waveform are shown in red. Events with t_{10-90} rise-times less than 430 ns are shown in black.

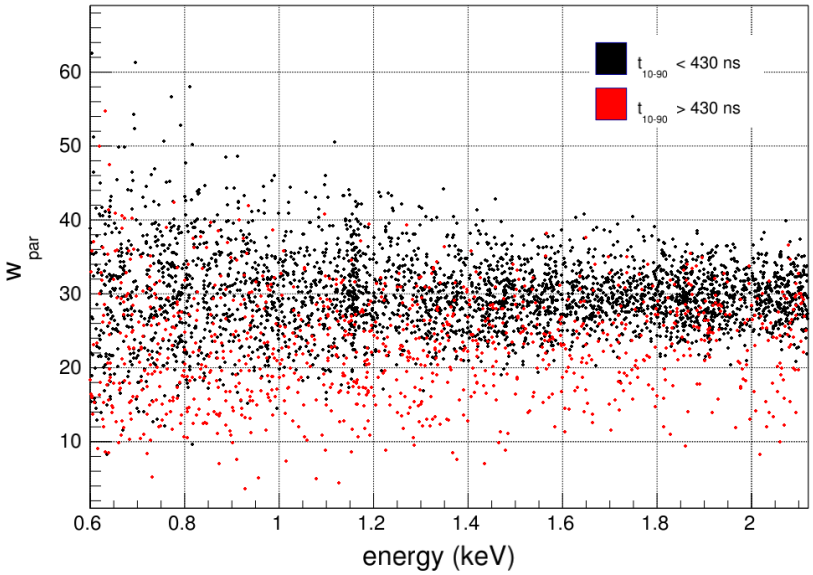

Figure 3.24: w_{par} versus energy for the data shown in Figure 3.23 attenuated by 40 and combined with noise. t_{10-90} rise-times were calculated for each event before attenuating. Events with t_{10-90} times less than 430 ns are shown in black. Events with t_{10-90} times greater than 430 ns are shown in red. The peak at 1.15 keV is from the ^{210}Pb peak originally at 46 keV.

The calculated w_{par} values for attenuated data falling between 0.6 to 0.9 keV are shown in Figure 3.25a. The attenuated data consists primarily of fast events so its distribution closely matches the waveform generator data. Figure 3.25b shows the energy range from 1.6 to 2.1 keV. Again, the attenuated data and pulser data distributions are very similar. A small number of slow rise-time events in the attenuated dataset extend below the fast event peak.

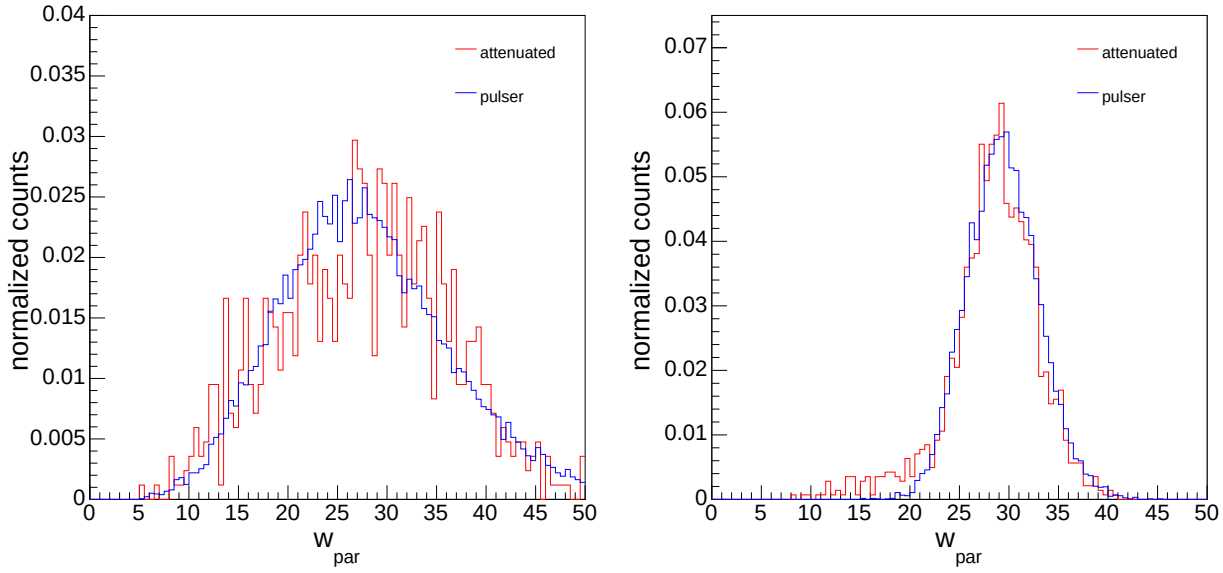

(a) $0.6 - 0.9$ keV (b) $1.6 - 2.1$ keV

Figure 3.25: Distributions of w_{par} values for events from the attenuated data (red) and fast waveform generator data (blue). The total counts in each distribution are normalized to one.

The attenuated dataset can be used as another means to evaluate the fast bulk event efficiency correction. Following the procedure outlined in Section 3.4.2, constant cuts in w_{par} were applied to attenuated data with t_{10-90} rise-times less than 430 ns followed by a correction for the bulk event acceptance calculated from the fast waveform generator dataset. Figure 3.26 shows the efficiency corrected, fast rise-time counts remaining in two energy windows as a function of cut position. The count rate in the two regions remain constant within errors, providing additional assurance that the acceptance efficiency calculated from the waveform generator data is correct.

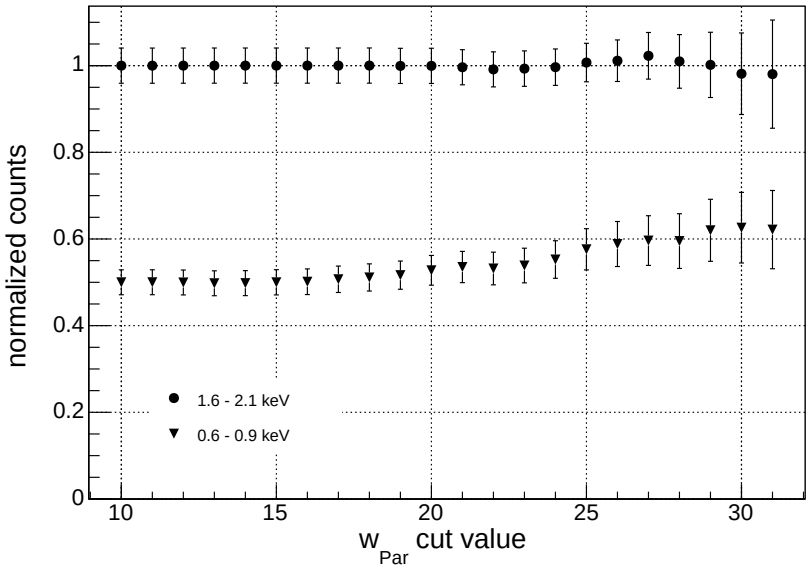

Figure 3.26: Efficiency corrected counts with $t_{10-90} < 430$ ns remaining in the attenuated dataset between 0.6 and 0.9 keV and 1.6 and 2.1 keV as a function of w_{par} cut position.

3.4.4: Defining a Surface Event Cut

The previous sections have illustrated the difficulties in identifying and removing surface event background events near the detector threshold. There have been a number of searches for WIMP dark matter using PPC detectors, all of which have approached slow event removal with differing strategies. In a previous MALBEK analysis [33] and an independent analysis of the CoGeNT PPC [51], a slow event cut was defined to accept 99% of fast events. The difficulty with this cut is that, while the bulk event acceptance is known, and the cut maximizes efficiency across the energy spectrum, it accepts slow events in the WIMP-nuclear recoil region of interest. Both analyses made attempts to quantify the number of surface events passing the cut, but ultimately treated the slow event contamination as an irreducible background parametrized by an exponential when fitting for a WIMP signal.

The CoGeNT collaboration [30], operating a detector very similar to MALBEK, begin with a similarly defined 99% cut, but then correct for slow pulse contamination by binning their data in 0.2 keV energy bins and fitting the resulting rise-time distribution with two log normal functions, one that parameterizes the slow event population and one for the fast event

population. These results are fit to determine the energy dependent fraction of slow events passing the cut and contaminating the signal region. The energy spectrum is then corrected for the calculated slow event contamination before fitting for a WIMP signal [30], or the slow event distribution is incorporated into a simultaneous maximum likelihood fit [21].

The TEXONO collaboration operates a PPC detector at a shallow site in Korea [58]. TEXONO calculates the fast event acceptance efficiency and the slow event suppression of their rise-time cut by examining the effects of the cut on populations of slow and fast events. Slow events datasets are defined using a combination of source data and Monte Carlo simulation. Pure bulk event data are collected using an n-type point-contact detector with identical dimensions to the PPC used for the source runs. The boron implanted p-contact that covers the surface of the n-type detector is less than a micron thick, eliminating slow events. A similar method for calculating the fast event acceptance and slow event rejection is adopted by CDEX, who operate at PPC at the China Jinping Underground Laboratory [59]. Unlike TEXONO, CDEX does not have an n-type point contact detector, so their analysis relies only on gamma-ray source calibrations with the p-type detector.

All of these analyses rely on a correction for the leakage of slow events into the fast event region of interest. The strategy adopted here will be to apply a cut that removes all events with w_{par} value less than 25, thereby eliminating the region where bulk and surface signals overlap while maintaining a reasonable signal acceptance efficiency. This cut only depends on the ability to correct for the fast event acceptance, a comparatively easier task than determining the slow event contribution from an unknown distribution of events. This is confirmed by the results presented in Section 3.4.2 and 3.4.3. The insensitivity of the number of efficiency corrected counts in the ^{68}Ge and ^{65}Zn L-shell capture peaks to the w_{par} cut placement, as shown in Figure 3.22, as well as the insensitivity of attenuated data to the w_{par} cut placement, as shown in Figure 3.26, indicate that the bulk event efficiency calculated from the waveform generator dataset is correct. To account for a possible systematic error in the fast event acceptance efficiency, the 24.7% uncertainty in the number of counts in

the efficiency corrected L peaks will be used as an estimate of the error in the fast event acceptance across the entire region of interest. The 89.5 kg-d spectra before and after the w_{par} cut and the acceptance efficiency of fast events after all cuts is shown in Figure 3.27.

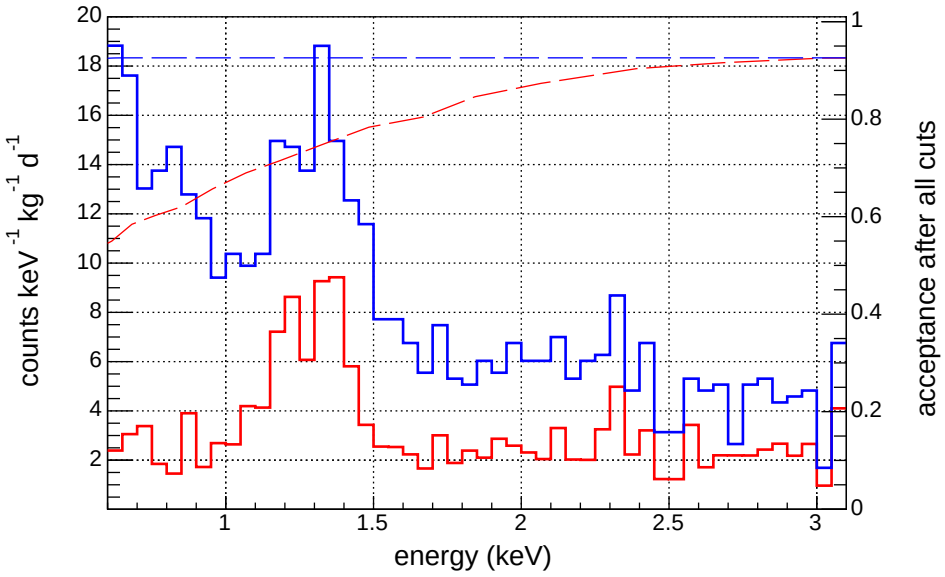

Figure 3.27: 89.5 kg-d data before (blue) and after (red) the application of a cut removing all of the events with w_{par} values less than 25. The acceptance after all cuts for both spectra is shown by dashed lines.

Section 3.5: Conclusions

Slow events that originate near the surface of PPC detectors are an important source of background for any experiment reliant on data collected below 50 keV. There are various techniques for identifying and subsequently removing these events, but all of them suffer at energies near the detector threshold due to the poor signal-to-noise ratio in this energy regime. Any cut that attempts to remove slow events must be studied to determine the rejection efficiency for slow events and the acceptance efficiency for fast events. An overestimation of the slow event cut efficiency or an underestimation of the fast event acceptance can result in artificially strict limits on WIMP interactions or the discovery of a signal that is in fact caused by background events.

Properly estimating the leakage of surface events after a cut requires either a pure population of surface events or a model of the slow event distributions from the various sources of slow events, both internal and external to the detector. This is very difficult, if not impossible to obtain. Preliminary efforts to model slow pulse formation and distributions are described in Chapter 4. As an alternative, the analyses presented here will utilize a cut that avoids areas where the rise-time calculation can not distinguish between bulk and surface events at the expense of the fast event acceptance efficiency.

CHAPTER 4: Surface Event Modeling

Events with long rise-times and degraded energy that result from interactions near the detector surface are a potentially significant source of background at low energies in PPC detectors. Chapter 3 described the origin of surface events and studied techniques for identifying and removing them. These techniques were validated using populations of events that are assumed to contain mostly fast bulk or slow surface events. Because of the limited statistics in these populations and the overlap between slow and fast distributions, the surface event removal cut becomes the dominant systematic uncertainty when looking for a rare-event signal near the detector threshold, as described in Chapter 5. A model of slow event formation would allow for further validation of the surface event removal cut and could potentially predict the background from surface events at low energies. This Chapter will describe attempts to construct a surface event model and compare predicted slow event distributions to experimental data collected using the MALBEK detector.

Section 4.1: Surface Event Signal Formation Model

The n^+ contact of a PPC detector is manufactured by diffusing lithium into the germanium crystal. This is often done by coating the outside of the crystal with lithium and baking the detector in an oven filled with inert gas. Some manufacturers simultaneously apply a voltage to the detector to accelerate the process. Figure 4.1 shows the estimated concentration of lithium within a crystal assuming an infinite source of lithium on the surface diffusing into the crystal at 300° C for ten minutes. Because the solubility of lithium increases rapidly with temperature [60], the concentration of lithium after the bake exceeds the room temperature solubility of lithium in germanium (1×10^{14} atoms/cm^3) in much

of the contact [61]. As the detector cools, this region becomes supersaturated and individual lithium atoms start to precipitate at defects within the crystal [62]. Images of lithium precipitates in a germanium crystal captured using x-ray topography can be found in [63]. These precipitates act as charge recombination sites, reducing the amount of charge from a surface event that reaches the depleted region of the detector.

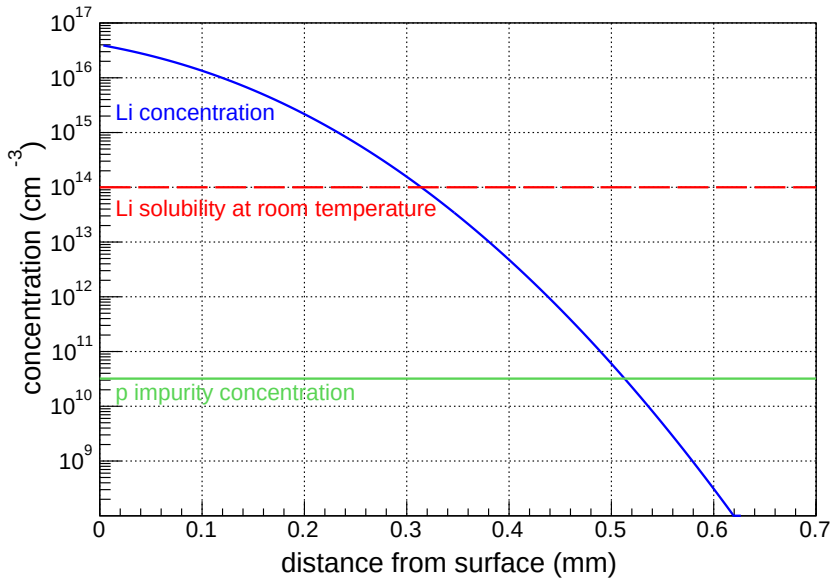

Figure 4.1: Calculation of the lithium concentration in a lithium drifted n^+ contact assuming a ten minute diffusion at 300° C from an infinite surface lithium source. The lithium solubility at room temperature is shown by the red dashed line. Lithium precipitates form at depths shallower than the intersection of the lithium concentration and the room temperature solubility. An example value of the p impurity concentration in a PPC is shown in green. The p-n junction is located at the intersection of the p impurity concentration curve and the lithium concentration curve. Figure adapted from [64].

When a PPC detector with a lithium diffused n^+ contact is fully biased, the layer of n^+ material closest to the crystal surface remains undepleted. This region, which extends between 0.5 mm and 1 mm into the crystal volume, is traditionally called the dead layer and is assumed to first order to be insensitive to incident radiation. This approximation was challenged as early as 1968, when events with long rise-times were observed from a lithium-drifted germanium detector and attributed to interactions occurring in a weak field region near the detector's surface [65]. In the following decades, there have been a number

of studies of lithium-diffused contacts, their effect on the detector active volume, and the origin of slow surface events [66–68]. An overview of these results can be found in [46].

David Radford of Oak Ridge National Lab has proposed a model for slow event formation in a PPC in which holes created in the undepleted lithium layer diffuse until they (1) recombine at the detector surface or a lithium precipitate site, or (2) move into the depleted detector bulk and are collected. In this model, the hole density is the relevant quantity, eliminating the computationally intensive task of tracking thousands of individual electron-hole pairs. The hole density, $\rho(\boldsymbol{r}, t)$, evolves according to the diffusion equation,

$$\frac{\partial \rho(\boldsymbol{r}, t)}{\partial t} = D\nabla^2 \rho(\boldsymbol{r}, t), \tag{4.1}$$

where D is the diffusion constant given by the Einstein relation

$$D = \frac{kT}{q}\mu. \tag{4.2}$$

In the Einstein relation, k is the Boltzmann constant, q is electronic charge, and μ is the hole mobility in germanium at temperature T. At 80 K, $\mu = 4.2 \times 10^4$ cm^{2}V^{-1}s^{-1} [69].

4.1.1: Basic Simulation

A basic implementation of the model illustrates the general characteristics of slow pulse formation. The simulation is performed on a $20 \times 20 \times 20$ micron grid using a finite difference approximation of Equation 4.1 with 1 ns time steps . The hole density is localized at a single lattice site at the beginning of the simulation and diffuses at each time step. Holes that reach the detector surface recombine and are removed from the simulation, holes that diffuse into the detector bulk are immediately collected, and the boundaries perpendicular to the detector surface are cyclic. This basic model does not include any charge recombination within the contact due to lithium precipitates and does not take into account the effects of the detector and preamplifier on the event rise-time.

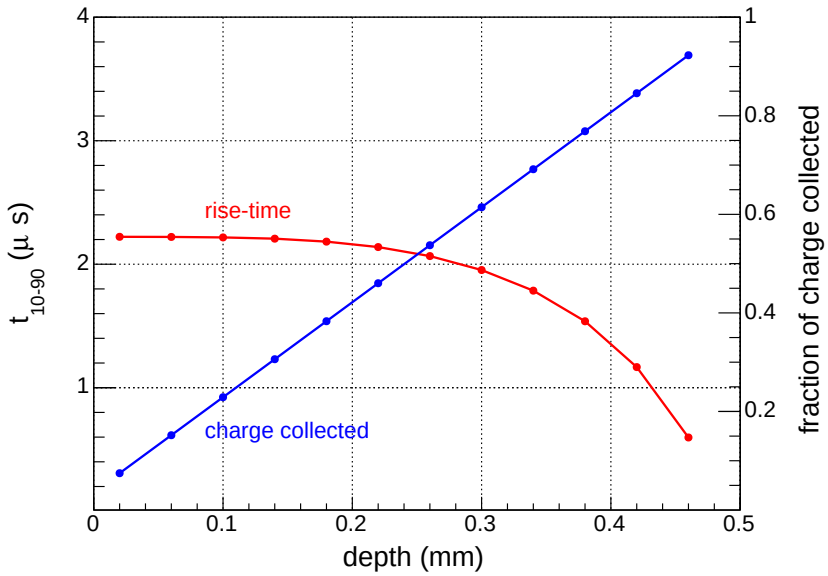

Figure 4.2: The simulated t_{10-90} rise-time and fractional charge collected for hole densities with varying initial positions within the n^+ contact. The model assumes a 0.5 mm dead layer. Holes that reach the detector surface are removed from the simulation. Holes that reach the surface-bulk interface are collected. Recombination within the contact is not considered.

Figure 4.2 shows the fractional charge collected and the t_{10-90} rise-time for simulated events starting at varying depths within a 0.5 mm thick lithium contact. The fraction of charge that reaches the detector bulk increases linearly as the initial event position moves deeper into the detector. The event rise-time shows the opposite behavior, asymptotically approaching a maximum rise-time for events originating close to the detector surface. This simulation qualitatively matches the behavior of data, where the lowest energy slow events also have the longest rise-times. However, the simple model does not replicate the variation in slow event rise-time observed in data and described in Chapter 3. This deficiency can be remedied by including lithium recombination sites in the model.

4.1.2: Simulation with Lithium Precipitates

The basic model described in Section 4.1.1 can be extended by including lithium precipitates dispersed throughout the n^+ contact. In this model, precipitates are distributed randomly within the lithium layer. After each time step, holes that diffuse to a grid site

occupied by a precipitate are assumed to recombine and are removed from the simulation. Instead of generating a lithium layer with the same dimensions as the detector and varying the initial position of the hole density, a new, smaller lithium distribution is generated for every simulated event. An example $2 \times 2 \times 2$ mm lithium distribution is shown in Figure 4.3. In this distribution, the sites are placed randomly within the lithium layer. The average lithium density decreases linearly with depth, from 0.5% at the detector surface to 0.0% at a depth of 1.0 mm.

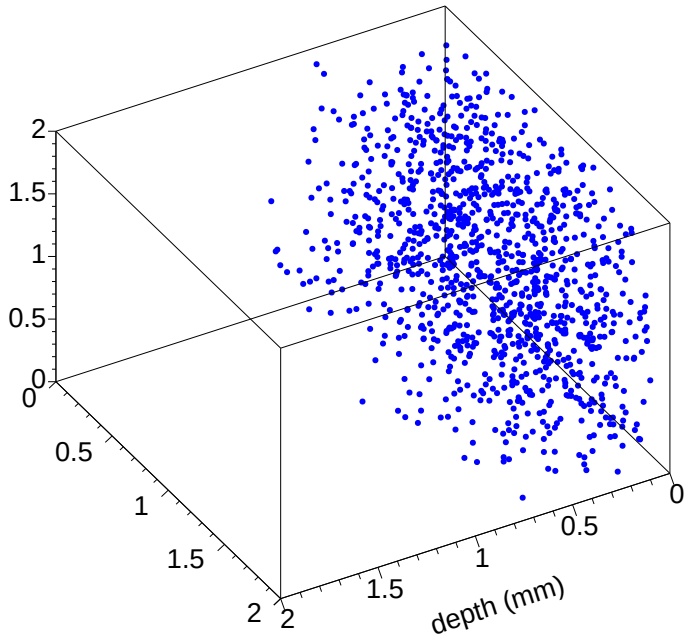

Figure 4.3: Example simulated lithium distribution. Lithium sites are placed randomly within the lithium layer. The lithium concentration decreases linearly from 0.5% at the detector surface to 0.0% at a depth of 1.0 mm.

Figure 4.4 shows results from a simulation performed with $20 \times 20 \times 20$ micron lithium precipitates distributed within a 0.5 mm deep lithium layer at a concentration of 0.5%. The depleted region starts 0.94 mm into the detector. The inclusion of the recombination sites results in two changes from the basic model simulation presented in Figure 4.2. First, the fraction of charge collected is no longer linear with the initial event position. This is due to the recombination of holes within the lithium layer. Second, the rise-time and the fraction

of initial charge collected varies for events with the same initial position, and the variation increases as the initial position approaches the detector surface. This more closely matches the behavior seen in data collected with the MALBEK detector.

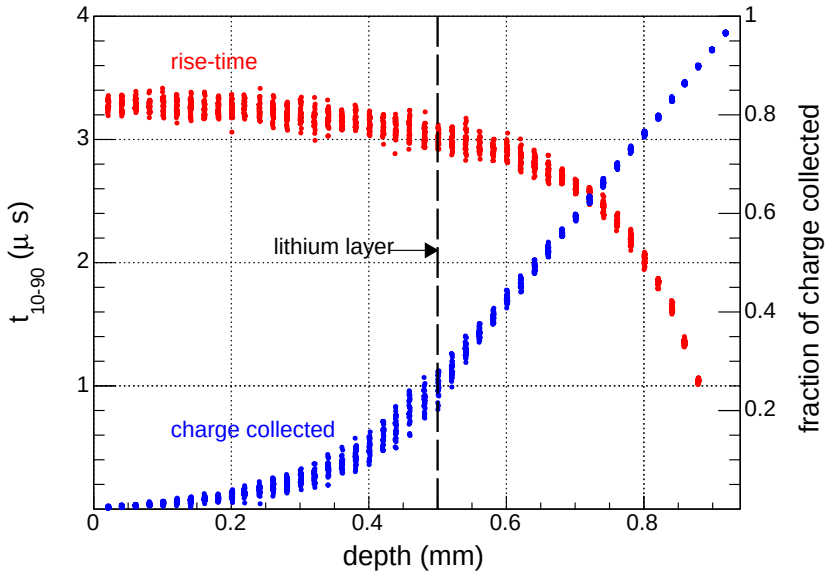

Figure 4.4: Results from a surface event model that includes lithium recombination sites. The depleted region of the detector begins at 0.94 mm. Lithium precipitates are uniformly distributed with a 0.5 % concentration at depths less than 0.5 mm.

Section 4.2: Properties of the Model

The lithium precipitate concentration, distribution, and size can significantly effect the simulation results. To better understand this, a set of simulations were performed where each of these model parameters were varied. Figure 4.5 shows results from three simulations performed with different lithium precipitate sizes, 20 microns, 60 microns, and 120 microns on a side. For each simulation, ten events are simulated at 20 micron intervals ranging from the detector surface to the depleted volume boundary at 1.0 mm. Lithium precipitates are randomly distributed within a 0.5 mm deep lithium layer for every simulated event. The total lithium concentration within the lithium layer is fixed at 1.0% for all three models based on [63], so as the precipitates get larger, the density of the precipitate sites decreases.

Two general properties are clear in the bottom panel of Figure 4.5. Both the mean t_{10-90} rise-time and the variability of the rise-time increases as the precipitates grow larger. This effect is more significant for events that occur closer to the detector surface and can be understood by examining the charge collected as a function of depth in the top panel of Figure 4.5. When the precipitates are 20 microns on a side, a larger fraction of the holes that drift through the lithium region recombine, effectively removing the holes that would require the longest time to reach the depleted region, thereby decreasing the rise-time of the event. As the precipitate size increases and the precipitate density decreases, a smaller fraction of the holes that pass through the lithium region recombine. There is also greater variability in the probability that holes will move out of the region due to the smaller number of lithium sites, increasing the variability in the t_{10-90} rise-time.

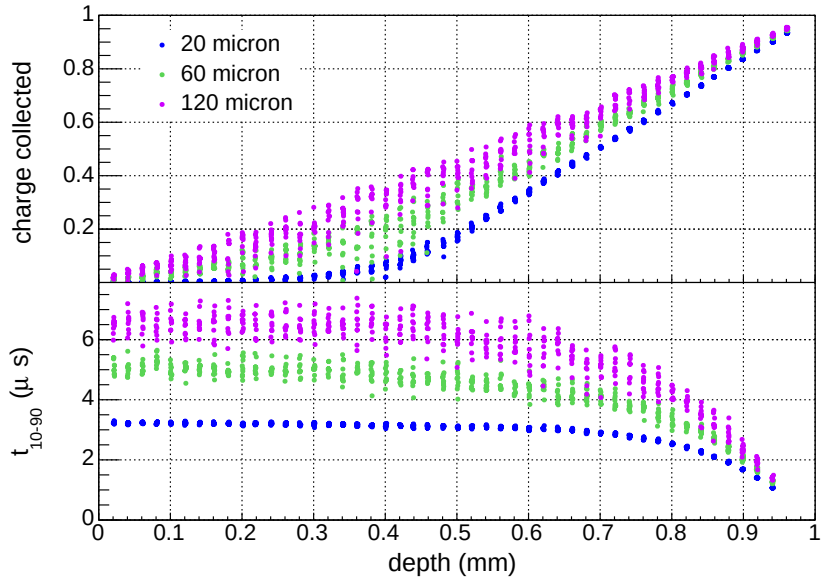

Figure 4.5: Results from simulations using precipitates that are 20 microns, 60 microns, and 120 microns on a side. The lithium precipitates are randomly distributed within a 0.5 mm deep lithium region. The total lithium density is 1.0% for all simulations, so the precipitate density varies with the precipitate size. Charge is collected at a depth of 1 mm.

Figure 4.6 shows the results from three simulations performed with total lithium concentrations of 0.5%, 1.0%, and 2.0%. In each simulation, 60 micron precipitates are randomly distributed between the detector surface and the lithium layer boundary at 0.5 mm. As the

lithium concentration used in the surface layer model increases, the mean rise-time predicted by the surface event simulation gets shorter. This is due to the larger probability of holes recombining within the lithium region. A higher lithium concentration also decreases the variability of the event rise-time. This is a smaller effect than was observed in Figure 4.5 because of the smaller relative change in the three modeled lithium site densities.

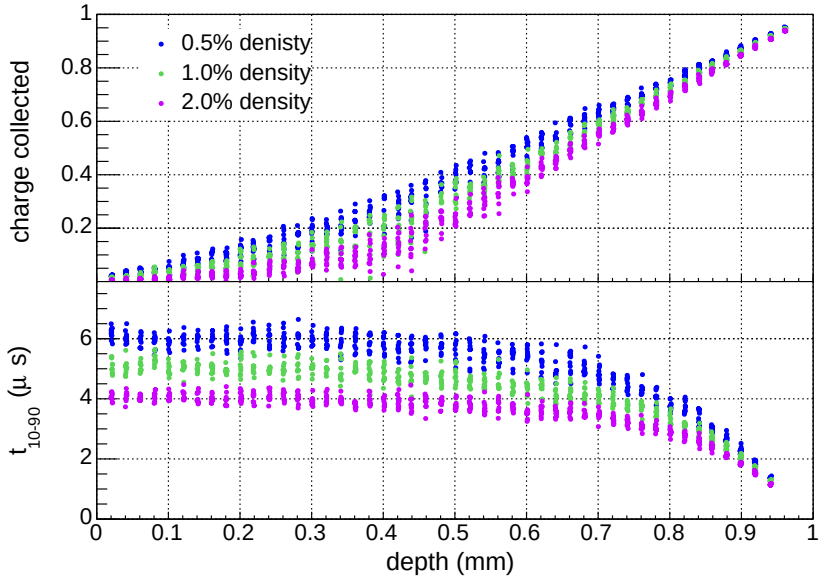

Figure 4.6: Simulation results from models with 0.5%, 1.0%, and 2.0% lithium concentrations within the 0.5 mm deep lithium layer. All three models use precipitates that are 60 microns on a side and a depletion region that begins at 1.0 mm.

Figure 4.7 compares simulation results from three models that use different precipitate distributions. In the first model, the lithium precipitates decrease linearly in size from 120 microns to 20 microns over the 0.5 mm lithium depth. The second model uses 60 micron precipitates throughout the entire lithium layer, but the lithium density decreases linearly with depth. The last model keeps the lithium size and density constant. All three models use the same total lithium concentration within the lithium layer. A changing lithium distribution more closely matches the expected lithium concentration calculated in Figure 4.1. However, including variation in the precipitate density or size has a relatively small impact on the simulation results, with the rise-time and charge collected closely matching results from the constant lithium density model.

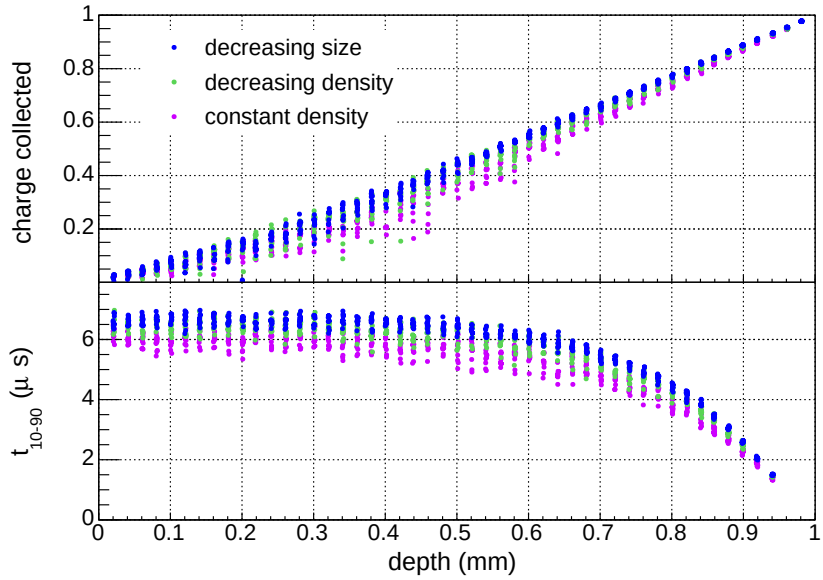

Figure 4.7: Simulation results for three different precipitate distributions, (1) linearly decreasing in size from 120 micron precipitates at the surface to 20 micron precipitates at 0.5 mm, (2) 60 micron precipitates linearly decreasing in density from the surface to 0.5 mm, and (3) constant density to 0.5 mm. All three distributions have a total lithium concentration of 0.5%.

The depth of the lithium region has a much greater effect on the simulation results than the distribution of the lithium sites within the layer. This is demonstrated in Figure 4.8, which shows three models with 1.0% lithium density, 60 micron precipitates, and lithium layer depths of 0.5 mm, 0.75 mm, and 1.0 mm. Increasing the lithium layer depth decreases the mean rise-time and reduces the fraction of charge that is collected from a given initial position.

Section 4.3: Comparison of Simulation Results to Data

The parameters of the surface event model described in Section 4.2 can be selected to achieve agreement between the slow event simulation and data. Two MALBEK datasets were used to do this, both collected while the detector was outside of the lead shield. The first dataset was collected with a 10 μC ^{241}Am source positioned 5 cm above the top of the MALBEK cryostat and co-axial with the detector. The second dataset was collected

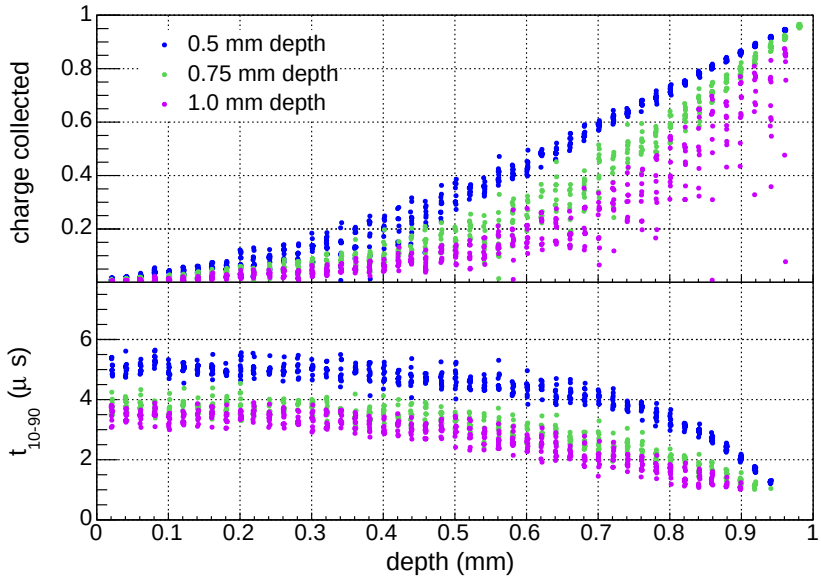

Figure 4.8: Simulation results for three different lithium layer depths, 0.5 mm, 0.75 mm, and 1.0 mm. All three models use a 1% lithium density, 60 micron precipitates, and a 1.0 mm deep depletion region.

with a 10 μC ^{109}Cd source in the same position. Both sources emit low energy gamma-rays, 59.5 keV and 88.0 keV respectively, that have a high probability of interacting near the detector surface. This results in a slow surface event rate that is about 100 times greater than the unshielded background rate. The high source event rate, which eliminates the need to perform a background subtraction of slow events originating from background sources, and the relative simplicity of the mono-energetic gamma-ray make these ideal datasets for optimizing the surface event model, with the caveat that the source only illuminates one surface of the detector. The t_{10-90} distribution for the ^{241}Am dataset is shown in Figure 4.9. Included in the figure are curves showing the median value of the slow-event rise-time as a function of energy and curves that bracket 68% and 95% of the events. The curves are not calculated below 5 keV where the t_{10-90} calculation begins to give inconsistent results. Figure 4.10 shows the t_{10-90} distribution for the ^{109}Cd data.

The simulations of surface events due to external ^{241}Am and ^{109}Cd sources assume mono-energetic gamma-rays incident on the detector surface. The effects of attenuating material between the calibration source and the detector or contributions from other background

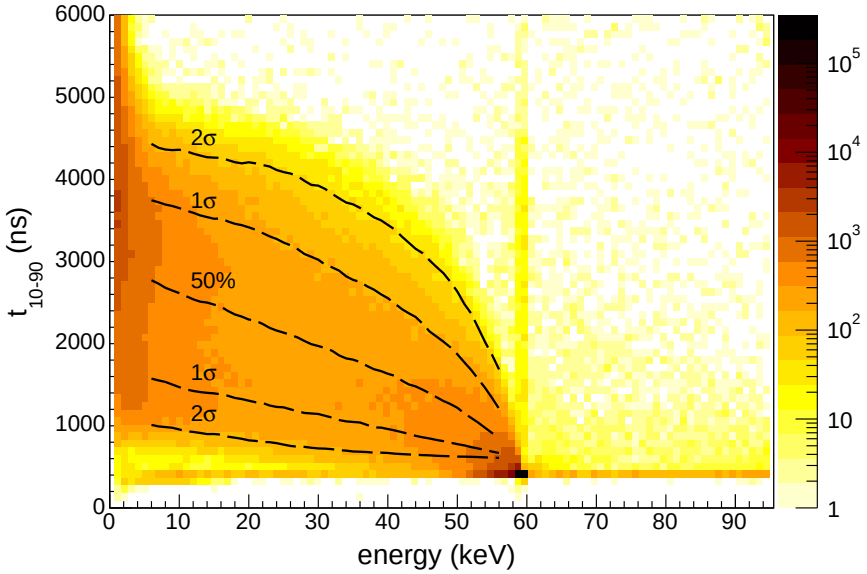

Figure 4.9: Rise-time distribution for ^{241}Am data. The median value is shown as well as 1σ and 2σ contours. The coloring indicates the number of events per bin.

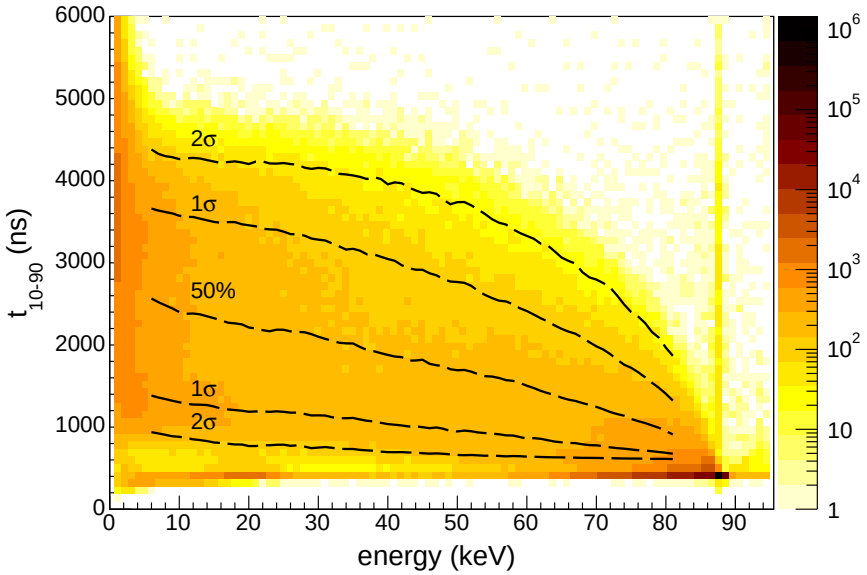

Figure 4.10: Rise-time distribution for ^{109}Cd data. The median value is shown as well as 1σ and 2σ contours. The coloring indicates the number of events per bin.

sources are not included. If the gamma-ray interacts within the lithium drifted contact, a surface event simulation is performed using the gamma-ray interaction depth as the initial location of the hole density. The amount of charge that moves into the detector bulk is recorded at each 1 ns time step to create a charge arrival signal. A waveform is then generated by convolving the charge arrival signal with a simulated bulk event waveform generated using `siggen` [44]. Finally, the event waveform is scaled based on the event energy and passed through an RC integrator to approximate the effect of the detector preamplifier. At this point, the simulated waveform data can be processed identically to data collected with the MALBEK detector. Noise can also be added to the simulated waveforms to more closely approximate real data. It was found that the addition of noise has limited effect on the energy distribution of the simulated event and only modifies the rise-time distribution below 2.5 keV. To avoid complicating the results of the basic simulation, no noise is added to the waveforms during this analysis.

The surface event simulation used to generate slow events from the sources uses parameters that maximize the agreement between the simulated data and the measurements. The depleted region of MALBEK is defined in the simulation to begin at a depth of 0.94 mm, the value calculated by Alexis Schubert based on a comparison between a ^{133}Ba source measurement and a detailed `Geant4` detector simulation [31]. Several lithium distributions were considered for use in the model. While distributions that vary with depth are likely more physically realistic, they were found to have a minimal effect on the final simulation results. For simplicity, the lithium precipitates were distributed uniformly throughout the lithium layer. The best agreement with data was achieved using lithium precipitates 60 microns on a side and a total lithium concentration of 1.5% within a 0.7 mm deep lithium layer. These values are within the range of precipitate sizes and densities observed in [63]. The 0.7 mm lithium layer depth simulation results most closely match the median rise-time observed in the source data but fail to replicate the variation in the t_{10-90} rise-time. This is improved by allowing the lithium layer depth to vary across the surface of the detector. In the model,

the lithium layer is assumed to be gaussian distributed with a 0.7 mm mean and a 0.01 mm^2 variance.

The simulated rise-time distribution from the ^{241}Am source is shown in Figure 4.11 alongside contours calculated from the MALBEK ^{241}Am data. The distribution agrees relatively well with the curves, closely matching the median t_{10-90} value and approximately following the observed rise-time variation. The simulated ^{241}Am energy spectrum is shown in Figure 4.12. Both spectra are normalized by the number of events in the 59.5 keV gamma peak. The simulation overestimates the number of slow surface events below 5 keV by about 50%. The two spectra can be brought into better agreement by reducing the concentration of lithium precipitates in the model, but not without modifying the simulated median rise-time and decreasing agreement with data.

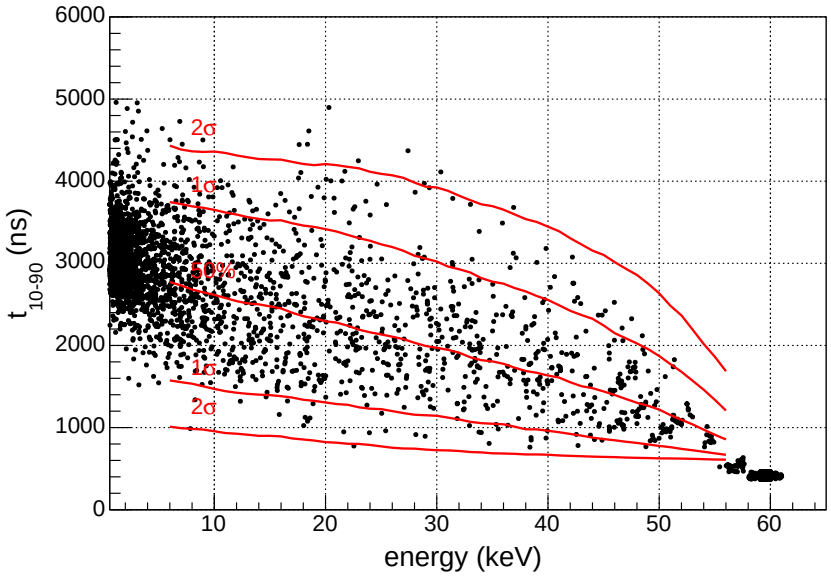

Figure 4.11: Rise-time distribution for simulated ^{241}Am data (black points). The median value and 1σ and 2σ contours calculated from the data displayed in Figure 4.9 are shown for comparison (red curves).

Figure 4.13 shows the rise-time distribution for the ^{109}Cd simulation. The simulation shows fair agreement with the curves calculated from the ^{109}Cd data, but predicts a median rise-time slower than what was measured. This may be due to ^{109}Cd gamma-rays that scatter and lose energy in other detector components before interacting in the crystal, driving the

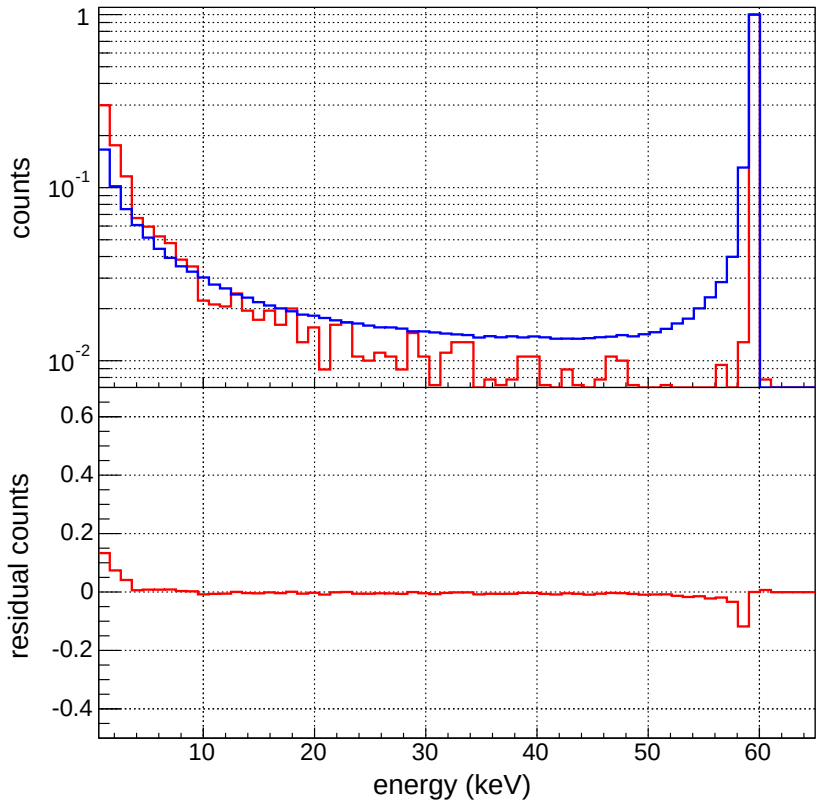

Figure 4.12: Simulated energy spectrum from a ^{241}Am source (red) compared to a measured spectrum (blue). Both spectra are normalized by the counts in the full energy peak. Residuals are shown in the bottom panel. The deficit of simulated events immediately below the full energy peak is due to the discrete depths used in the simulation.

median rise-time lower. This effect would be more significant for the higher energy ^{109}Cd gamma-rays than the ^{241}Am gamma-rays and is not captured in the simulation. Figure 4.14 compares the simulated energy spectrum to the measured one. Both spectra are normalized by the number of events in the 88.0 keV peak and, in contrast to the ^{241}Am data, are in good agreement below 5 keV. This may also be due to down-scattered gamma-rays that are not included in the simulation.

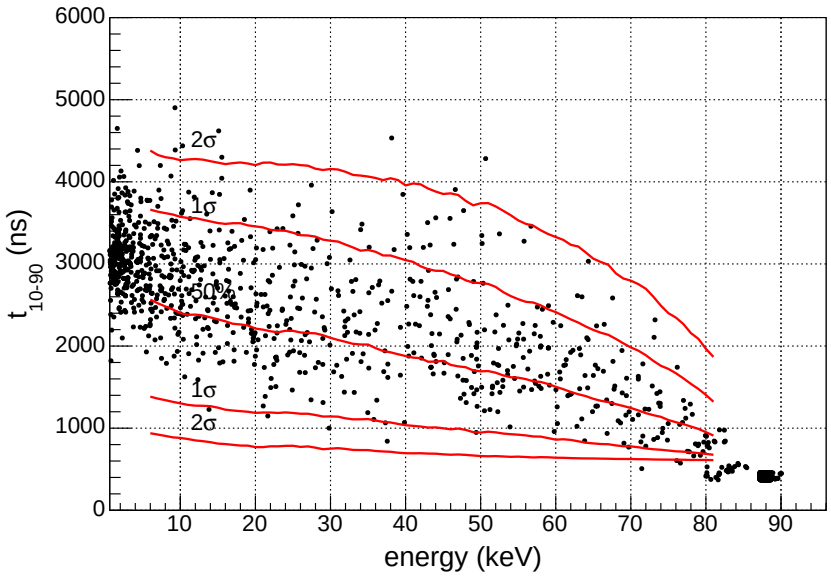

Figure 4.13: Rise-time distribution for simulated ^{109}Cd data (black points). The median value and 1σ and 2σ contours calculated from the data displayed in Figure 4.10 are shown for comparison (red curves).

Section 4.4: Conclusion

Despite its relative simplicity, the surface event model captures the general characteristics of slow events observed with the MALBEK detector, and it does so without requiring significant computational overhead. The exact prediction of the model depends critically on the distribution of lithium within the lithium contact. The ^{241}Am and ^{109}Cd source data only probe the n^+ contact on the top face of the detector. Variations of the contact over the crystal sides and bottom face would result in deviations from the simulations presented

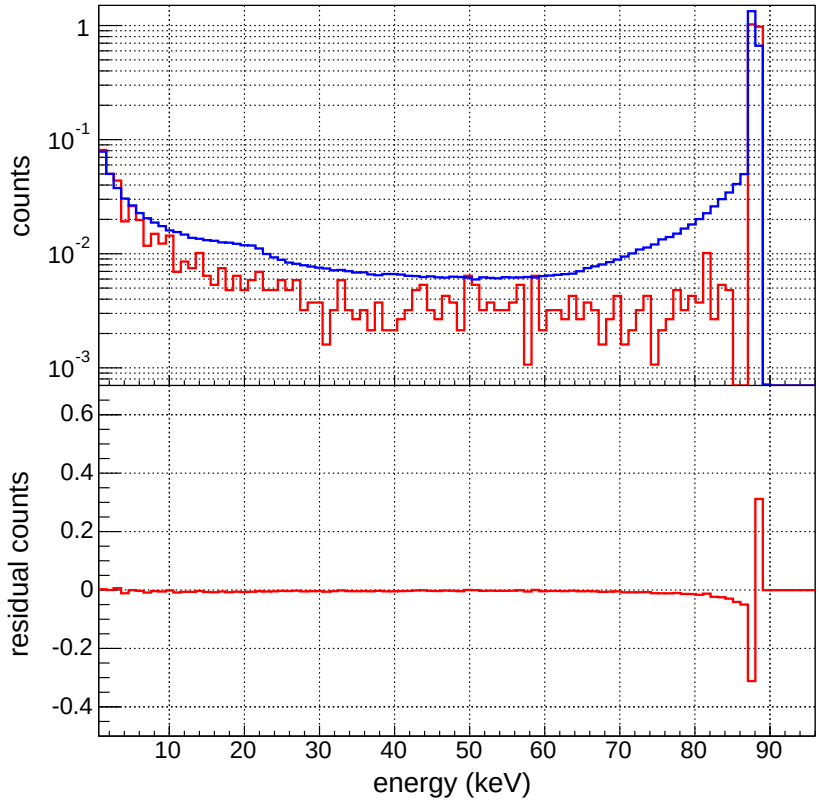

Figure 4.14: Simulated energy spectrum from a ^{109}Cd source (red) compared to a measured spectrum (blue). Both spectra are normalized by the counts in the full energy peak. Residuals are shown in the bottom panel. The deficit of simulated events immediately below the full energy peak is due to the discrete depths used in the simulation.

here.

Further validation of the surface event model could be done using collimated source measurements at various locations along the detector surface, similar to the α source measurements performed in [45]. This data could then be compared to a model that incorporates a Monte Carlo simulation of the detector and its components, like that developed in [31]. As it stands, the surface event model provides a convincing explanation for the physical origin of slow surface events and a promising path towards a complete understanding of this significant source of background in PPC detectors.

CHAPTER 5: Rare-Event Searches with MALBEK

The very characteristics that make p-type point contact detectors advantageous for MAJORANA, low energy thresholds and excellent energy resolution, also make them sensitive to signals from a number of hypothetical rare processes. These include WIMP-nuclear scattering, solar axion-electron interactions, and Pauli exclusion principle violating electron transitions. This Chapter will utilize 89.5 kg-d of data collected at KURF with the MALBEK detector to search for these types of decays.

Section 5.1: The 89.5 kg-d Dataset

The MALBEK detector began collecting shielded data at KURF on 15 November 2011. Data taking proceeded for 288 days, ending on 8 August 2012. Due to a period of frequent power outages at KURF, the dataset is divided into two distinct run periods, 15 November 2011 to 12 March 2012 and 9 April 2012 to 29 August 2012. There were additional intervals of down-time within the two run periods caused by intermittent power outages at the mine, reducing the total live-time of the detector to 221.5 days.

Daily operation of the detector was handled remotely from UNC-Chapel Hill. Bimonthly visits to KURF were necessary to refill the liquid nitrogen buffer dewars and perform periodic calibration runs. MALBEK remained in the nitrogen purged shield for the duration of the 288 day period and, despite the power outages, remained cold for the entirety of the 288 day operation. An `OrcaScript` automated run controls and provided daily emails to operators with run statistics, including trigger rate, run length, and preliminary energy spectra, as well as alerts about excursions from standard operating conditions, e.g. liquid nitrogen fills or loss of bias voltage. Data files saved on the local data acquisition machine at KURF were

transferred nightly to UNC-Chapel Hill where they were processed and saved to disk.

5.1.1: Overview of Data Processing

A detailed description of the MALBEK data processing chain and data selection cuts can be found in Chapter 2. In brief, MALBEK analysis is done using the Germanium Analysis Toolkit (`GAT`), a modular data analysis framework developed by the MAJORANA collaboration [39]. `GAT` processors calculate event properties, e.g. energy and w_{par}, on an event by event basis. After the data are processed, a set of basic data selection cuts are applied. First, periods of high noise are removed from the dataset, e.g. data collected immediately following a power outage. Then a set of timing cuts are performed to remove events coincident with preamplifier inhibit pulses, waveform generator events, and events occurring within 15 minutes of a liquid nitrogen dewar fill. Finally, cuts based on the waveform shape are applied to eliminate non-physics events caused by microphonics and bias voltage micro-discharges.

Pulser generated fast events were used to determine the trigger efficiency of the SIS3302 digitizer. Based on these results, the analysis threshold was defined to be 600 eV, 50 eV above the point at which the trigger efficiency drops below 99%. This avoids possible systematic effects from rapidly changing efficiencies due to small gain shifts at the analysis threshold. The two data periods are calibrated separately using a set of low energy lines from ^{68}Ge, ^{55}Fe, and ^{65}Zn as described in Section 2.4.1.

In addition to the basic data selection cuts, a w_{par} cut is applied to remove slow event contamination. Slow surface events and methods for slow event identification are described in Chapter 3. The w_{par} cut removes events from the region where slow event leakage is most significant at the expense of a reduced efficiency for accepting fast events. The placement of the w_{par} cut was determined by examining the number of efficiency corrected events remaining in different features of calibration energy spectra as a function of the cut definition. Figure 5.1 shows the efficiency corrected energy spectrum after the application of all data

selection cuts alongside the total signal acceptance curve. The acceptance curve includes the calculated efficiency for the data selection cuts and the measured trigger efficiency of the SIS3302 digitizer.

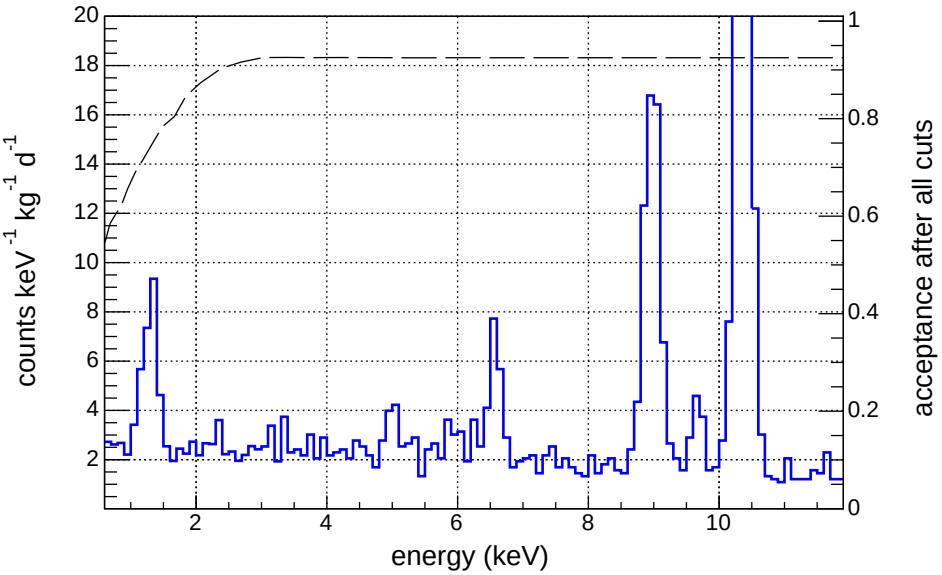

Figure 5.1: Efficiency corrected 89.5 kg-d day spectrum collected in the MALBEK shield at KURF. The signal acceptance after the application of all cuts and including the trigger efficiency is shown by the dashed line.

5.1.2: Detector Backgrounds

Two sets of features are immediately evident when examining Figure 5.1, a series of peaks and a continuum that is roughly constant with energy. These two components comprise the most significant backgrounds in the region of interest for WIMP dark matter, solar axions, and Pauli exclusion principle violating decays, and must be considered when performing a search for these phenomena.

At these energies, photons have a few micron attenuation length in germanium, meaning x-rays external to the detector are entirely shielded by the ∼1 mm Li surface contact. The peaks present in the spectrum must then originate from nuclei within the crystal decaying via electron capture and the subsequent cascade of Auger electrons and x-rays emitted as the electrons in the daughter nucleus fill the resulting electronic vacancy. These nuclei are formed

by cosmogenic activation, which occurs primarily due to spallation reactions of fast neutrons on germanium. The formation of cosmogenic impurities can be reduced by minimizing the surface exposure of the detector, shielding the detector when it is on the surface, and avoiding transport of the detector by plane, where the higher neutron and proton fluxes increase the activation rate. Studies of the activation rates of germanium and methods for shielding detector material can be found in [70, 71].

The MALBEK detector moved underground on 12 January 2010 and remained there for 650 days. On 24 October 2011 the detector was removed from the shield, transported to the surface, and driven to CANBERRA in Meriden, Connecticut to remove the lead shims described in Section 2.3 from the cryostat. The detector went back underground three days later and data taking commenced 12 days after the detector's return to the laboratory. Because of the few day surface exposure, short lived ^{71}Ge events are present in the data alongside isotopes with relatively longer life-times. The identifiable peaks in the spectrum are listed in Table 5.1.

Table 5.1: Peaks in the 89.5 kg-d spectrum.

Isotope	**Peaks (keV)**	**Half-life**
^{49}V	4.97	330 d
^{55}Fe	6.54	2.74 y
^{65}Zn	1.10, 8.98	243.9 d
^{68}Ga†	9.66	67.7 m
^{68}Ge	1.30, 10.37	271.0 d
^{71}Ge	1.30, 10.37	11.4 d

† daughter of ^{68}Ge

Figure 5.2 shows the counts in the ^{68,71}Ge K-shell capture peak beginning 12 days after the detector returned to KURF after the trip to Canberra. The data are well fit by two exponentials with fixed decay constants for the 11.4 d ^{71}Ge half-life and the 271.0 d ^{68}Ge half-life. The statistics are too low in the other capture peaks to perform similar analyses of

their decay over time. The transition region fills approximately 8.7% of the detector volume, so it is reasonable to expect that an observable component of the surface event rate should decay with the ^{71}Ge cosmogenic peak. However, less than 2.3 surface events per day are expected from ^{71}Ge during the first five days of data collection, even before accounting for surface events that fall below the detector threshold, and this is smaller than the poisson fluctuation in the baseline surface event rate.

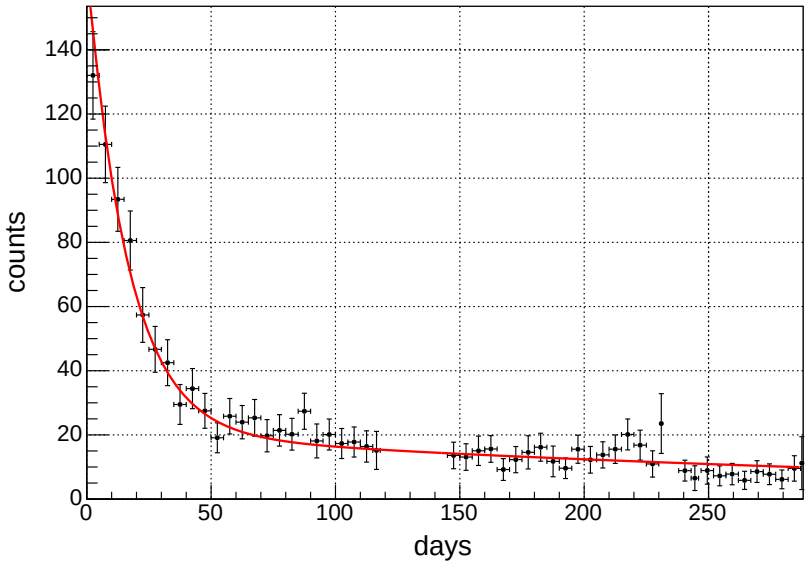

Figure 5.2: Counts in the ^{68,71}Ge K-shell capture peak (10.37 keV) over the 288 day run period that began 12 days after the detector went underground. The data are fit with two exponential functions with fixed decay times for ^{68}Ge, which has a 271.0 d half-life, and the shorter lived ^{71}Ge, which decays with an 11.4 d half-life. The fit has χ^2/NDF = 31.9/51 and a p-value = 0.98.

The second feature in the spectrum is a continuum with a rate of ∼2 counts/keV/kg/d. The majority of the events in this spectral feature arise from the forward Compton scattering of gamma-rays emitted by primordial contaminants, ^{238}U, ^{232}Th, and ^{40}K, as well as cosmogenic cobalt isotopes in MALBEK detector components [31]. In addition, there is a sub-dominant contribution to the continuum from beta-decays, bremsstrahlung, tritium, and slow surface events that are not removed by the w_{par} cut. The continuum shows no variation in rate over time after surface event removal.

The final contributor to the low energy MALBEK spectrum are neutron nuclear recoil

events. This source of background is particularly problematic for WIMP searches because a neutron nuclear recoil signature is similar to the expected signal from a WIMP. A series of `GEANT4` Monte Carlo Simulations of the MALBEK detector were performed by A. Schubert [31]. These simulations focus on sources of backgrounds over a wide energy range, up to the saturation of the MALBEK preamplifier at 2.5 MeV, but can be used to estimate the expected neutron contribution near the detector threshold. The majority of neutron events in MALBEK are due to cosmic-ray muon induced neutrons created by spallation reactions in the detector shielding. These events are estimated to occur at a rate less than 1 count/kg/day between the detector threshold and 10 keV, and may contribute to the WIMP signal rate measured in Section 5.2. There is also a contribution due to neutrons from spontaneous fission and (α, n) reactions in the cavern rock and shielding material, but at the MALBEK background levels, signals from these neutrons are negligible. This may not be the case for the Majorana Demonstrator, which should have an event rate in the continuum near the detector threshold three orders of magnitude lower than MALBEK.

The capture peaks and the continuum background will be included as nuisance parameters in the maximum likelihood fits described in the following sections. Due to the lack of a detailed simulation of the neutron spectrum below 10 keV, contributions from muon induced neutrons will not be included in the background model. If a statistically significant WIMP signal had been found in the data, a careful examination of this background would be required.

5.1.3: Systematic Effects

In addition to understanding the various sources of background in the low energy region, one must consider systematic effects that can modify the sensitivity of the measurement. These include uncertainties inherent to the experimental hardware, like the active mass of the detector or the efficiency of the data acquisition trigger, as well as uncertainties in the analysis, including incorrect cut efficiencies or unaccounted for sources of background.

The largest source of systematic uncertainty in the analysis described here is the signal acceptance of the of w_{par} cut. Unlike the basic data selection cuts described in Chapter 2, where the cut distinguishes between clear populations of events or removes a fractionally small number of events, the w_{par} cut is placed in a region where there is significant overlap between the signal and surface backgrounds. The studies of calibration data described in Chapter 3 provide convincing evidence that the acceptance of the w_{par} cut is correctly determined using the pulser dataset. However, without a pure population of physics signal events at threshold or a validated model that describes the surface event population in the region, the accuracy of the calculated cut acceptance can not be verified. Independent of the pulser, the closest pure population of fast events near the detector energy threshold are the L-shell capture peaks at 1.10 keV and 1.30 keV. Figure 3.22 shows the event rate of the L-capture peaks as a function of the w_{par} cut placement. This analysis will use the 24.7% uncertainty in the number of counts in these peaks peak after a $w_{par} < 25$ cut as an estimate of the systematic error of the cut signal acceptance. It should be noted that this error estimate is limited by the statistics of the two peaks and is likely conservative. An additional difficulty arises when trying to assign a systematic uncertainty to the w_{par} signal acceptance in the energy range between the L-shell peaks and 2.5 keV, above which there is clear separation between bulk and surface events. Without features in the spectrum below the K-shell that contain sufficient statistics to characterize the evolution of the acceptance uncertainty with energy, the 24.7% value is applied over the entire region of interest, even in regions with clear surface and bulk discrimination. Because of the unambiguous interpretation of L-shell counts as bulk events and the modest effect on the detector sensitivity, a 24.7% error will be used as the uncertainty in the fast event acceptance of the w_{par} cut for the searches performed here.

In addition to the uncertainty in the signal acceptance of the w_{par} cut, there may be some contribution to the MALBEK spectrum from surface events that are not removed. The cut is placed to minimize surface event leakage into the signal region, but without a pure population

of surface events, the actual contribution is difficult to determine. No correction for surface event leakage or an additional background model component parameterizing the leakage is used in this analysis, in contrast to [33, 51].

The data selection cuts described in Chapter 2 each have systematic uncertainties that must be considered. The A/E parameter used to make the preliminary cut of noise-like events defines two distinct populations of events, and the uncertainty associated with the cut is negligible. The microphonics cut and integral cut are defined to accept 99% of the events in the pulser dataset. The signal acceptance of these cuts, in contrast to the w_{par} cut, are relatively insensitive to a change in cut position. A shift in the cut value of 5% results in a corresponding change in acceptance of 1.5%. The effect of these cuts on the spectrum was also evaluated in [33] by comparing the events remaining in the L-capture peak after the cut application. Based on these results, the uncertainty of the acceptance efficiencies for the microphonics and micro-discharge cuts are considered negligible and are not included in the analysis. Any leakage of microphonic events or other noise induced triggers into the region of interest is small relative to other background sources and is not included in the background model.

Timing cuts that remove events coincident with pulser events, liquid nitrogen fills, and preamplifier resets reduce the live-time, and hence the total exposure of the detector. Any uncertainty in this quantity is due to misalignment of the run start time relative to the digitizer clock. This is constrained to be less than the preamplifier reset period, or 40 ms, for every run. At worst, the live-time deviates from the calculated value by 2.9 minutes over the duration of the 288 day run period, an inconsequential amount. The dominant uncertainty in the detector exposure is the active volume of the detector. This was calculated in [31] by comparing the ratio of events observed in the 81 keV and 356 keV peaks from a ^{133}Ba source to a detailed Monte Carlo simulation. It was determined that the full charge collection depth within the detector is 933 ± 120 μm. This reduces the active mass of the detector from 465 g to 404.2 ± 15 g and results in a total exposure of 89.5 ± 3.3 kg-d.

Unaccounted for non-linearities or gain shifts in the data acquisition system or the preamplifier could introduce systematics that alter the spectrum or change the trigger efficiency over time. The gain stability of the system can be checked by monitoring the location of the pulser peak in the spectrum. The centroid of the pulser peak, which is nominally at 35 keV, deviates by no more than 400 eV over the duration of data taking. This corresponds to a gain shift at the threshold less than 7 eV, meaning the analysis threshold remains 50 eV above the point at which the trigger efficiency drops below 99%. The use of the SIS3302 onboard trapezoidal filter for triggering eliminates any effect that baseline drift might have on the triggering efficiency. The attenuator and waveform generators provide a useful tool for evaluating the linearity in the region of interest, particularly below the L-capture lines where there are no spectral features to calibrate from. A waveform generator pulse of fixed amplitude was reduced in dB steps using the step attenuators with precision better than 0.01 dB and injected into the test input of the preamplifier. The absolute error in the linearity from 7 keV down to the detector threshold is 20 eV, negligible compared to the 160 keV FWHM resolution at 0.6 keV. An additional energy dependent efficiency correction is imposed by the pulse reset preamplifier. An event that causes a preamplifier reset will be eliminated by the timing cuts, and larger amplitude events are more likely to do this. At low rates, the probability of an event causing a reset is roughly linear, spanning from $\sim$0% at 0 keV to $\sim$100% at 2.7 MeV. At 10 keV, the efficiency correction from this effect is 0.3% and will be ignored in this analysis.

The final class of systematic effects arise from sources of unaccounted background in the data. These backgrounds, be they from noise, physics, or poorly understood detector response, are difficult to handle. This is especially true in experiments operating near the detector threshold, where the detector performance and physics backgrounds are often not as well understood as at higher energies. This can be compounded in a single channel detector lacking the ability to discriminate between electronic recoils and nuclear recoils, especially when looking for an astrophysical signal that doesn't allow a 'signal off' measurement. When

searching for low-mass WIMPs, experiments must rely on a well characterized background spectra to make any convincing claim of discovery. This should be kept in mind when interpreting the results from detectors searching for rare-events and operating near the limits of their capabilities. Table 5.2 summarizes the systematics described in this section.

Table 5.2: Summary of systematic errors

Source	**Error estimate**	**Comments**
signal acceptance of w_{par} cut	24.7%	estimated from the uncertainty in L-shell peak counts, included in likelihood analysis
slow event leakage after cut	-	not accounted for
signal acceptance of data selection cuts	-	negligible
noise event leakage after cut	-	negligible
live-time calculation error	< 3 minutes	negligible
fiducial volume calculation error	± 15 g	determined in [31], included in likelihood analysis
energy non-linearity	< 20 eV	estimated using attenuator and pulser over the region of interest, negligible relative to detector resolution
gain change at threshold	< 7 eV	estimated by tracking pulser peak position during running, negligible effect on trigger efficiency and on spectral shape relative to the detector resolution
energy dependent preamplifier efficiency	$< 0.3\%$	negligible
error in signal model	-	discussed in Sections 5.2.1, 5.3.1, and 5.4.1

Section 5.2: Search for Weakly Interacting Massive Particles

5.2.1: Expected Signal

The expected differential rate for a WIMP recoiling from a nucleus within the detector is

$$\frac{dR}{dE_{ee}} = \left(\frac{dR}{dE_{nr}}\right)\left(\frac{dE_{nr}}{dE_{ee}}\right)F^2 \tag{5.1}$$

where $\frac{dR}{dE_{nr}}$ is the WIMP interaction rate per recoil energy, including detector characteristics and the properties of the WIMP halo, $\frac{dE_{nr}}{dE_{ee}}$ relates the energy of the recoiling nucleus to the measured ionization energy within the detector, and F^2 is a form factor characterizing the energy dependence of the coherent-nuclear-recoil cross section. The rate depends on two free parameters, M_W, the mass of the WIMP, and σ_{nuc}, the WIMP-nuclear cross section.

The WIMP interaction rate in a detector was calculated by Lewin and Smith [17] and is:

$$\frac{dR}{dE_{nr}} = \frac{k_0}{k_1}\frac{R_0}{E_0 r}\left\{\frac{v_0\sqrt{\pi}}{4v_E(t)}\left[\mathrm{erf}\left(\frac{v_{min}+v_E(t)}{v_0}\right) - \mathrm{erf}\left(\frac{v_{min}-v_E(t)}{v_0}\right)\right] - e^{-v_{esc}^2/v_0^2}\right\} \tag{5.2}$$

with

$$v_E(t) = v_{E_0} + v_{E_1}\sin(2\pi t),$$

$$\frac{k_0}{k_1} = \left[\mathrm{erf}\left(\frac{v_{esc}}{v_0}\right) - \frac{2}{\sqrt{\pi}}\frac{v_{esc}}{v_0}e^{-v_{esc}^2/v_0^2}\right]^{-1},$$

and

$$R_0 = \frac{2}{\sqrt{\pi}}\frac{N_A}{A}\frac{\rho_D}{M_W}\sigma_{nuc}v_0.$$

The parameters in Equation 5.2 are:

R – event rate per unit mass

E_{nr} – recoil energy of the nucleus

R_0 – total event rate

E_0 – energy of a WIMP moving with velocity v_0

v_0 – halo velocity dispersion

r – reduced mass, $\frac{4M_W M_T}{(M_W+M_T)^2}$

M_W – WIMP mass

M_T – detector material nuclear mass

v_{min} – minimum WIMP velocity that can produce recoil energy E_{nr}

v_{esc} – halo escape velocity

v_{E_0}, v_{E_1} – velocities of the Earth

N_A – Avogadro's number

A – atomic number of detector material

ρ_D – dark matter halo density

σ_{nuc} – WIMP-nuclear cross section at zero velocity

Equation 5.2 includes the time dependence of the WIMP interaction rate due to the Earth's rotation about the sun. In this analysis, the time dependence of the rate is not considered and t is held constant. To compare results obtained from experiments with different target nuclei, the WIMP-nuclear cross section can be converted to a WIMP-nucleon cross section following [72],

$$\sigma_{W-n} = \left(\frac{\mu_1}{\mu_A}\right)^2 \frac{1}{A^2}\sigma_{nuc} \tag{5.3}$$

where $\mu_A = \frac{M_W M_T}{M_W+M_T}$ is the reduced mass of the WIMP-target system and μ_1 is defined at $A = 1$.

A nuclear recoil and an electronic recoil of equivalent energy will create different amounts of measurable ionization in the detector. To accommodate this difference, the relative signal efficiency for a nuclear recoil event, also called the quenching factor or yield, must be

accounted for. A commonly used theoretical model relating E_{nr} and E_{ee} in an ionization detector is given by Lindhard et al. [17, 73]. For a target nucleus with Z protons and atomic mass A,

$$E_{ee} = \frac{kE_{nr}g(\epsilon)}{1 + kg(\epsilon)} \tag{5.4}$$

with

$$g(\epsilon) = 3\epsilon^{0.15} + 0.7\epsilon^{0.6} + \epsilon,$$

$$\epsilon = 11.5E_{nr}Z^{-7/3},$$

and

$$k = 0.133Z^{2/3}A^{-1/2}.$$

The Lindhard model predicts that a germanium target, which has $Z = 32$ and $A = 72.6$, will have $k = 0.157$. Several measurements of the germanium quenching factor performed using neutron scattering have found deviations from the Lindhard model prediction, with most results falling between $k = 0.1$ and $k = 0.2$ [74]. Figure 5.3 shows the quenching factor calculated from Lindhard theory for several k values. Below 20 keV recoil energy, Lindhard theory is well approximated by the function $E_{ee} = \alpha E_{nr}^{\beta}$ [51]. Fits of this function to the Lindhard model are also shown in Figure 5.3. Below 4.5 keV ionization energy, these power law parameterizations agree with Lindhard theory within 1%, and in this analysis, $\frac{dE_{nr}}{dE_{ee}}$ in Equation 5.1 is calculated by inverting these fits to the theory. Figure 5.3 also shows the parameterization used by CoGeNT, with $\alpha = 0.2$ and $\beta = 1.12$ [30], that is based on the quenching factor measurement performed in [75]. Because the quenching factor can significantly alter the sensitivity of the experiment to a particular WIMP mass, results are presented using parameterizations of Lindhard theory with $k = 0.1$, $k = 0.157$, $k = 0.2$, and the CoGeNT parameterization.

The last term in Equation 5.1 is the nuclear form factor, F^2, which modifies the WIMP nuclear cross section to account for loss of coherence as the momentum transfer between the

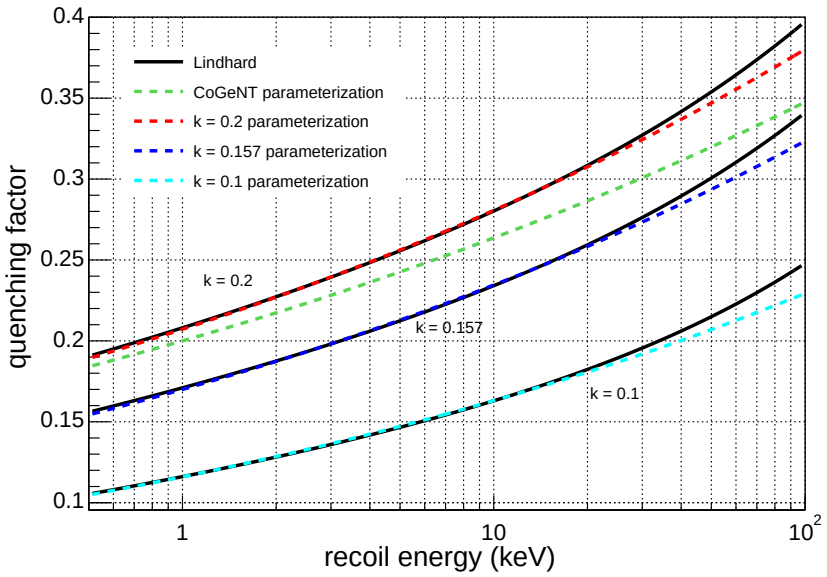

Figure 5.3: Lindhard theory quenching factor versus energy for $k = 0.2$, $k = 0.157$, and $k = 0.1$ and a parameterization of Lindhard theory of the form $E_{ee} = \alpha E_{nr}^{\beta}$. The $k = 0.2$ and $k = 0.157$ parameterization were determined by a fit to the theory. The CoGeNT parameterization is from [30].

WIMP and nucleus increases. The Helm form factor suggested in [17, 76] is used here, where

$$F(qr_n) = 3\frac{j_1(qr_n)}{qr_n}e^{-(qs)^2/s} \tag{5.5}$$

with

$$qr_n = \frac{\sqrt{2M_T E_{nr}}}{197.3}1.14A^{1/3},$$

where j_1 is a Bessel function, $s = 0.9$ fm is the nuclear skin thickness, q is the momentum transferred, and r_n is the effective nuclear radius.

While there is uncertainty on many of the parameters that contribute to Equation 5.1, this analysis will assume the standard values used in the literature to simplify comparison with other experiments, $v_o = 220$ km/s, $v_{esc} = 544$ km/s, $v_{E_0} = 244$ km/s, $\rho_D = 0.3$ GeV/c^2/cm^3, and the Helm form factor.

5.2.2: Statistical Method

The profile likelihood approach is used to search for signals in the MALBEK data [77]. This type of analysis allows one to include backgrounds and other unknown quantities into the statistical model as nuisance parameters and maximize the parameter space used for the search. This is a particularly desirable feature in an experiment where the background signal distribution is not well known or there is overlap between the signal and background regions, common problems in dark matter experiments. Use of the profile likelihood approach can increase the sensitivity of the experiment, but also makes the result more susceptible to systematic uncertainties or incorrect background assumptions. It is therefore important for the experimentalist to correctly incorporate uncertainties into the model. The application of profile likelihood analyses to dark matter experiments can be found in [51, 78, 79] among others.

Application of the profile likelihood ratio test statistic begins with construction of the likelihood function,

$$\mathcal{L}\left(\mu,\theta\right)=\prod_{n}f\left(x_{n}|\mu,\theta\right), \tag{5.6}$$

where $f\left(x_{n}|\mu,\theta\right)$ is a probability distribution function (pdf) describing the data, x_n, with the set of parameters $\{\mu,\theta\}$. The likelihood function can include additional terms that constrain the parameters based on external measurements or simulations. Assuming μ is the parameter of interest and θ is a nuisance parameter or set of nuisance parameters, the profile likelihood ratio is written as

$$\lambda\left(\mu\right)=\frac{\mathcal{L}(\mu,\hat{\hat{\theta}})}{\mathcal{L}(\hat{\mu},\hat{\theta})}, \tag{5.7}$$

where $\hat{\mu}$ and $\hat{\theta}$ are the maximum likelihood estimators found by maximizing $\mathcal{L}$, and $\hat{\hat{\theta}}$ is the conditional maximum likelihood estimator found when $\mathcal{L}$ is maximized for a given value of μ. The profile likelihood ratio is no longer a function of θ and will evaluate to one when the

hypothesized value of μ is equal to $\hat{\mu}$. $\lambda(\mu)$ will approach zero as the hypothesis becomes less compatible with the data. According to Wilks' theorem, the quantity $-2\log\lambda(\mu)$ is asymptotically distributed according to a chi-square distribution with number-of-degrees-of-freedom equal to the number of parameters of interest, in this case one. Using this quantity as a test statistic, the profile likelihood ratio can be used to find a signal or, in the absence of one, place limits on its strength.

The task of searching for a signal using the profile likelihood ratio method then amounts to defining a likelihood function based on a set of pdfs that describe the signal of interest and any backgrounds, adding constraints to the likelihood based on external measurements, constructing the profile likelihood ratio in terms of the parameter of interest, and finally, for a given confidence level (C.L.), determining the upper and lower bounds of the confidence interval, μ_{upper} and μ_{lower}. This is done by starting at the minimum of the likelihood curve, $\lambda(\mu = \hat{\mu})$, and scanning in μ to find the values at which

$$-2\log\lambda(\mu_{upper}) = -2\log\lambda(\mu_{lower}) = \frac{1}{2}\chi^2(C.L.). \tag{5.8}$$

In the event that the lower bound, μ_{lower}, is less than zero, only an upper limit is set.

When searching for a rare event, there is the possibility that the best fit value for the parameter of interest, $\hat{\mu}$, will have an unphysical value, e.g. a WIMP interaction with a cross section less than zero. In this case, the profile likelihood curve is no longer parabolic and a special method must be adopted to determine the confidence interval. The rare event searches presented here will use the bounded likelihood method present in [80]. In the event that $\hat{\mu}$ is less than zero, a new profile likelihood curve is created,

$$-2\log\lambda'(\mu) = -2\log\lambda(\mu) + 2\log\lambda(0) \tag{5.9}$$

such that $-2\log\lambda'(\mu = 0) = 0$. The upper limit is then found by scanning from $-2\log\lambda'(\mu = 0)$ to the point where the curve is equal to the desired C.L. percentile of a chi-squared

distribution.

The profile likelihood analyses are performed using the `RooFit` package, a `ROOT`-based toolkit for modeling event distributions [81]. `RooFit` includes a library of standard pdfs that can be used to construct models and likelihood functions and includes tools that allow users to build their own custom pdfs. `PyWIMP`, a framework for generating limits on a WIMP signal built around `RooFit` written by Michael Marino [51, 82], includes a WIMP pdf that will be used in Section 5.2.3. `RooFit` can also generate a pdf by sampling from a distribution. This functionality is used in the solar axion search described in Section 5.3.2.

5.2.3: Model and Fit Results

The WIMP search was performed using data between 0.6 keV and 4.5 keV. Extending the region to higher energies does not significantly alter the results but requires the use of an additional set of nuisance parameters to describe the ^{49}V peak. The dominant background features in this region of the energy spectrum are a flat continuum and the L-shell capture lines from ^{65}Zn (1.10 keV) and ^{68}Ge (1.30 keV). Both are included in the background model. Other background contributions in this region that are not considered might include neutrons, slow events, and sub-dominant cosmogenic L-capture lines. The likelihood function includes the following pdfs:

- Flat background: $f_{flat}(E) = 1$
- L-shell background peaks: $f_{peak_i} = \dfrac{1}{\sigma_L\sqrt{2\pi}} \exp\left(-\dfrac{(E-\mu_i)^2}{2\sigma_L^2}\right)$
- WIMP signal pdf: f_{WIMP} = Equation 5.1

A parameter that describes the number of events in each feature, N_{flat}, N_i, and N_{WIMP}, is included in the likelihood function in an extended likelihood term, Poisson $(\sum_x N_x, N_{obs})$, where the sum is over the pdfs. Unlike N_{flat} and N_i, N_{WIMP} is not an independent parameter. It is determined by the WIMP-nuclear cross section, σ_{nuc}, and the WIMP mass, M_W. The number of events in the background pdfs and σ_{nuc} are allowed to float during the analysis.

Additional constraints are included in the likelihood function to incorporate possible sources of systematic error. To accommodate the 1.6% error in the detector non-linearity near threshold, a Gaussian constraint $0.5([\mu_i - \mu_{i,0}]/0.016\mu_{i,0})^2$ with expected value $\mu_{i,0}$ is included in the likelihood function for both peak pdfs. Ideally, the width of the L-shell peaks would be constrained based on a fit of the data to the empirical resolution function,

$$\sigma(E) = \sqrt{\sigma_e^2 + 2.96FE} \tag{5.10}$$

where $\sigma(E)$ is the peak width at energy E, $\sigma_e = 69.8$ eV is the electronic noise measured with a pulser, and F is the Fano factor. Figure 5.4 shows the widths of the peaks in the low energy region and the best fit to Equation 5.10. Because of the poor fit, no term is included in the likelihood function to constrain the L-capture peak widths. Instead, a single width, σ_L, is used for both peaks and is allowed to float during the analysis.

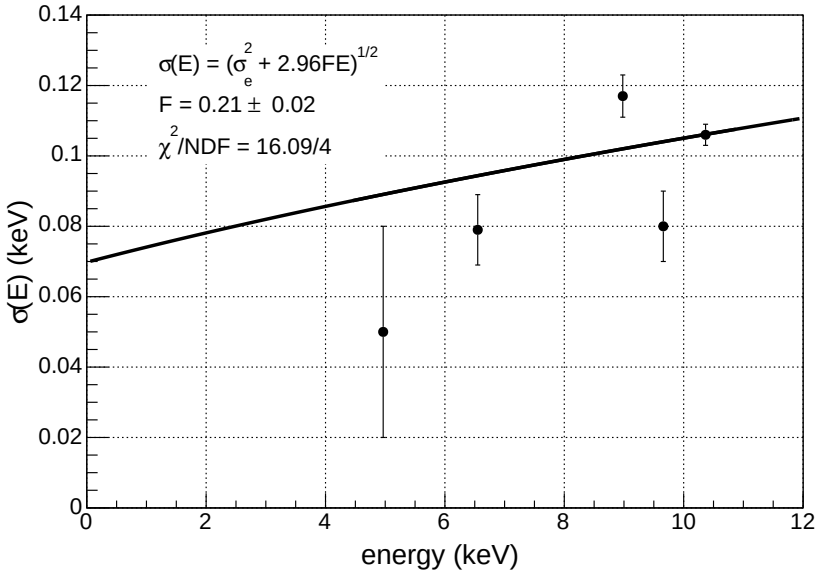

Figure 5.4: Widths of the peaks in the low energy region fit to Equation 5.10.

The dominant systematic uncertainty in this region of the spectrum arises from the acceptance efficiency of the slow event cut. A 24.7% error, estimated from the uncertainty on the number of counts remaining in the L-peaks after the slow event cut and efficiency

correction, is assigned to the signal efficiency over the entire region of interest. This clearly overestimates the error in the signal efficiency at energies above 2.5 keV, where slow and fast events are easily distinguishable, and correspondingly decreases the sensitivity of the experiment to WIMPs with masses above 20 GeV. However, it is difficult to motivate assigning a particular energy dependent error to the signal efficiency, so only the energy independent case is considered here. An additional uncertainty on the signal efficiency comes from the 3.7% error on the detector volume calculation. These uncertainties are included by incorporating the constraint $0.5([\eta-1]/0.242)^2$, where η is the total signal efficiency, in the likelihood function. The total likelihood function is

$$-\log\mathcal{L} = -\log\left(\text{Poisson}\left(\sum_x \eta N_x, N_{obs}\right)\right) - \sum_n \log\left(\frac{1}{\sum_x N_x}\left(\sum_x N_x f_x\right)\right) - \sum_i 0.5\left(\frac{\mu_i-\mu_{i,0}}{0.016\mu_{i,0}}\right)^2 - 0.5\left(\frac{\eta-1}{0.242}\right)^2, \tag{5.11}$$

where the sum over n is over each event in the energy region, the sums over x include all of the background and signal pdfs, and the sum over i sums over the gaussian L-shell capture peak pdfs. A summary of the parameters used in the fit, their allowed values, and the systematic uncertainty used to constrain the values can be found in Table 5.3.

The search was performed for a set of WIMP masses ranging from 5.5 to 100 GeV. For each WIMP mass, the profile likelihood curve is calculated and the 90% C.L. limits are determined. The profile likelihood curves calculated for an 8.0 GeV WIMP, $\lambda(\sigma_{nuclear})$, both with and without systematic uncertainties, are shown in Figure 5.6. The increase in width of the profile likelihood curve including systematic errors is due almost entirely to the uncertainty on the signal efficiency. An example fit of an 8.0 GeV WIMP to the data is shown in Figure 5.5. In this fit, σ_{W-n} is fixed at 2.62×10^{-41} cm^2, the 90% C.L. exclusion limit determined from the profile likelihood curve.

The number of events attributed to the signal and background model as a function of the WIMP mass are shown in Figures 5.7, 5.8, and 5.9. Independent of the WIMP mass, the

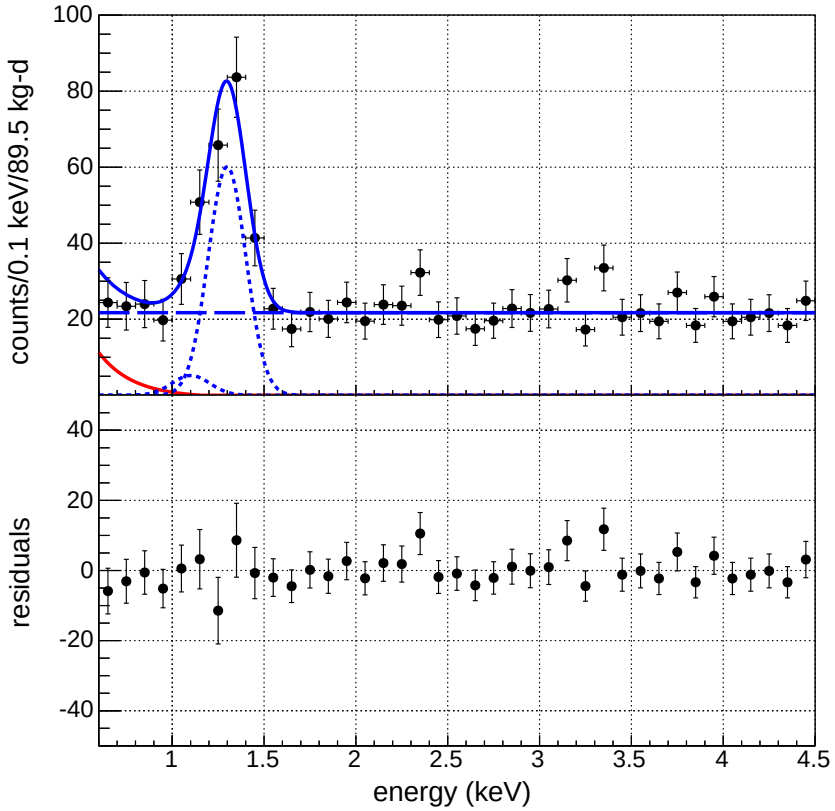

Figure 5.5: Fit of an 8.0 GeV WIMP with $\sigma_{W-n} = 2.62\times10^{-41}$ cm^2, the cross section excluded at 90% C.L., to the MALBEK 89.5 kg-d dataset. The fit model includes a flat background (blue dashed), the ^{65}Zn and ^{68}Ge L capture peaks (blue dotted), and an 8.0 GeV WIMP (red). The signal plus background model is shown in blue. The fit residuals are shown in the bottom panel.

Table 5.3: Parameters used in the WIMP analysis, their allowed ranges, and, when relevant, the systematic uncertainty used to constrain the value. The allowed ranges for the number of events in each pdf, σ_{nuc}, and the L-capture width were chosen so that the parameters never reached the range boundary during the analysis.

Parameter	**Value**	**Uncertainty**
Zn L-capture mean, μ_{Zn}	1.10 keV	1.6%
Ge L-capture mean, μ_{Ga}	1.30 keV	1.6%
L-capture width, σ_L	$0 \rightarrow 1$ keV	
N_{flat}	$0 \rightarrow 10^4$	
N_{Zn}	$0 \rightarrow 10^4$	
N_{Ge}	$0 \rightarrow 10^4$	
σ_{nuc}[†]	$-20 \rightarrow 200$	
Signal efficiency, η	1	24.2%

[†] range includes unphysical values to prevent fits at the parameter boundary

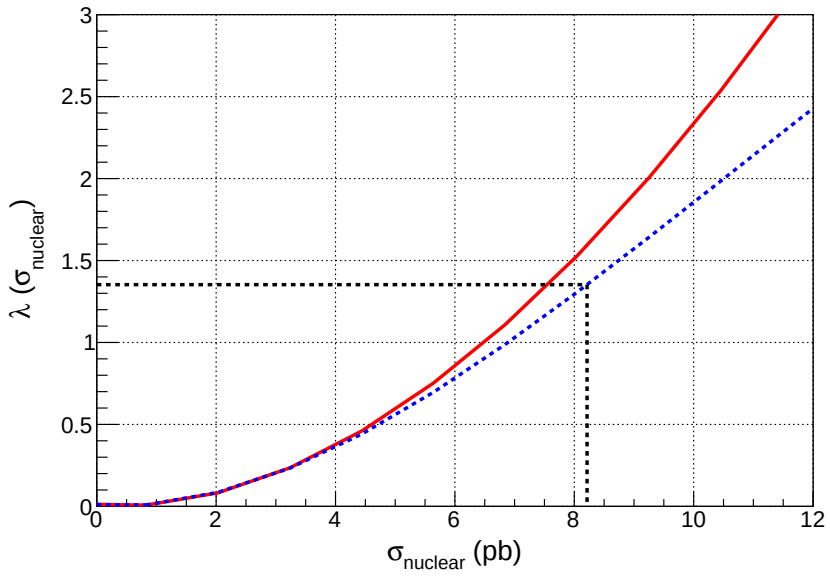

Figure 5.6: Profile likelihood curves for the WIMP-nuclear cross section of an 8.0 GeV WIMP. The blue dashed curve includes the systematic uncertainties described in the text. The red curve does not. The 90% C.L. including the systematic uncertainties is shown by the black dashed lines.

best fit results favor no WIMP signal. When a fit is performed at the 90% C.L. exclusion limit, the number of events in the background model decreases to accommodate the WIMP signal. At masses below 10 GeV, most of these counts come from the Zn L-capture line with a small contribution from the flat background. As the WIMP mass increases, counts are also removed from the flat background component.

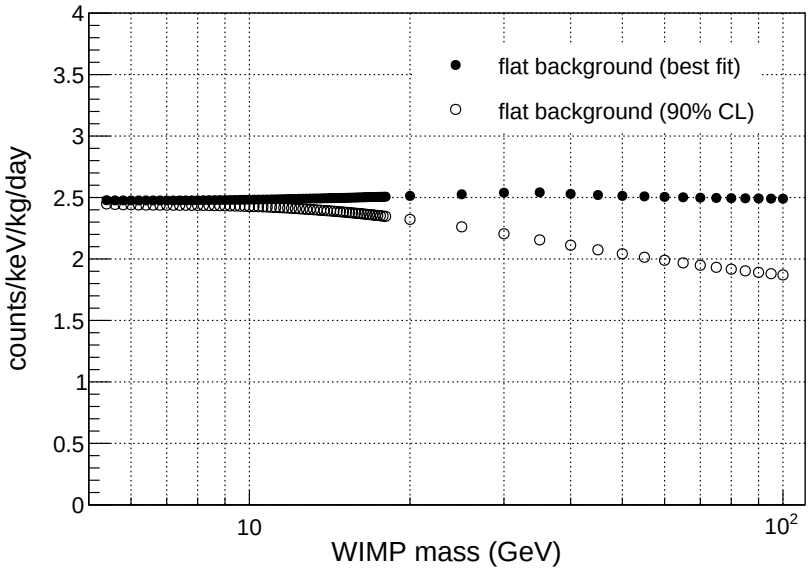

Figure 5.7: Number of events in the flat background component for the best fit and at the 90% σ_{nuc} exclusion limit for each WIMP mass analyzed.

Because no statistically significant evidence for a WIMP signal was found within the MALBEK data, 90% exclusion curves were determined using the profile likelihood method. These curves are shown in Figure 5.10 for several parameterizations of the Lindhard model. The choice of quenching factor can alter the sensitivity of the experiment up to a factor of a few. The MALBEK result from [33] is shown in Figure 5.10 for comparison. This alternative MALBEK analysis used a slow event cut with a 99% fast event acceptance, then included an exponential pdf in the likelihood function to model the slow event leakage. At masses below 20 GeV, this analysis is more sensitive than the MALBEK result in [33] by a factor of approximately two, despite the much larger systematic uncertainty from the w_{par} cut. This is because the slow event background, whose spectral shape is very similar to that expected

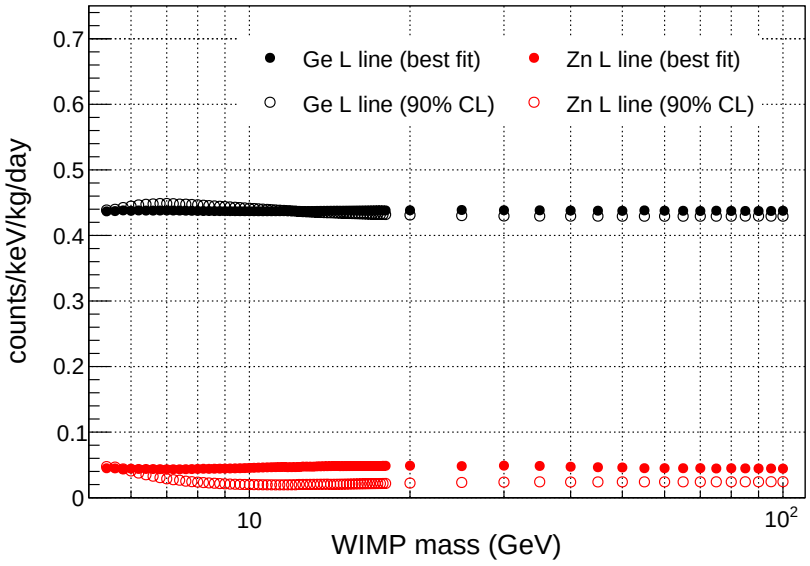

Figure 5.8: Number of events in the L-capture peaks for the best fit and at the 90% σ_{nuc} exclusion limit for each WIMP mass analyzed.

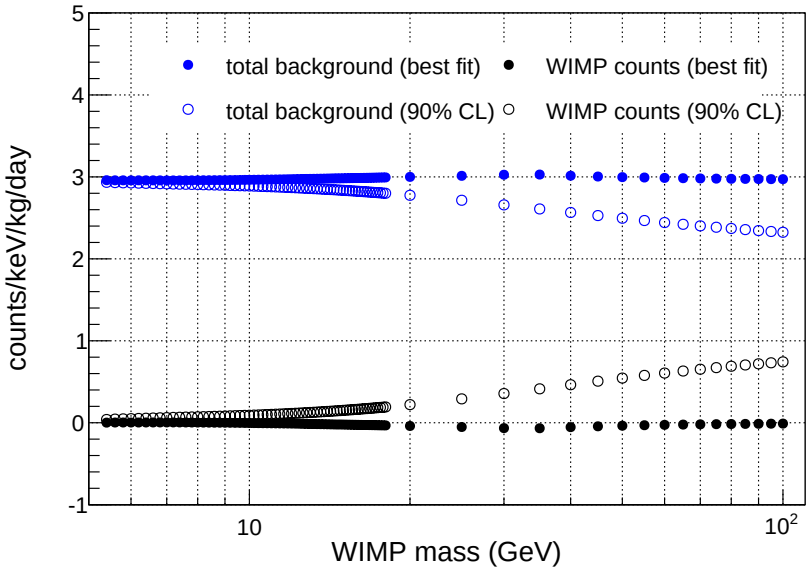

Figure 5.9: Number of events in the in the background model, which includes the L-capture peaks and the flat continuum, and the WIMP signal model at the 90% σ_{nuc} exclusion limit for each WIMP mass analyzed.

from a low-mass WIMP, is almost completely removed. At higher WIMP masses, where the slow cut placement for both approaches is roughly identical, the 99% cut from [33] is free from the large systematic uncertainty and results in a stricter limit on the WIMP-nucleon cross section.

The MALBEK limits are shown in comparison to a selection of current WIMP dark matter experiments in Figure 5.10. Two of the limits shown in the figure, CoGeNT [21] and CDEX [59], use PPC detectors very similar to MALBEK. The CoGeNT result from [30], which finds a possible WIMP signal using a different background model and analysis technique from [21], is also shown. Additional limits using germanium as the target nucleus comes from CDMSLite [27] and SuperCDMS [83]. CDMSLite is a SuperCDMS iZip detector operated at high bias to increase its sensitivity to light WIMPs. The limits found with CDMSLite are in tension with the CoGeNT signal region despite the low exposure, 6.3 kg-days, and the lack of any background subtraction during the analysis. In addition to the CoGeNT signal region, hints at a WIMP signal from CDMS II Si [25] and the long standing modulation signal from DAMA [84] are shown. The strictest limits on spin-independent WIMP scattering come from large noble liquid detectors. Results are shown from the first 85 days of data collected with LUX [26], a 350 kg dual phase xenon time projection chamber (TPC) operating at the Sanford Underground Laboratory, and 225 days of data collected with XENON100 [85], a 62 kg dual phase xenon TPC at Gran Sasso National Laboratory. LUX, XENON100, and SuperCDMS exclude WIMPs in this mass region with cross sections several orders of magnitude lower than the PPC-based experiments. The Majorana Demonstrator should have significantly lower backgrounds and much larger mass than the PPC experiments shown here, and the projected sensitivity of the Demonstrator to a WIMP signal can be found in [51, 86].

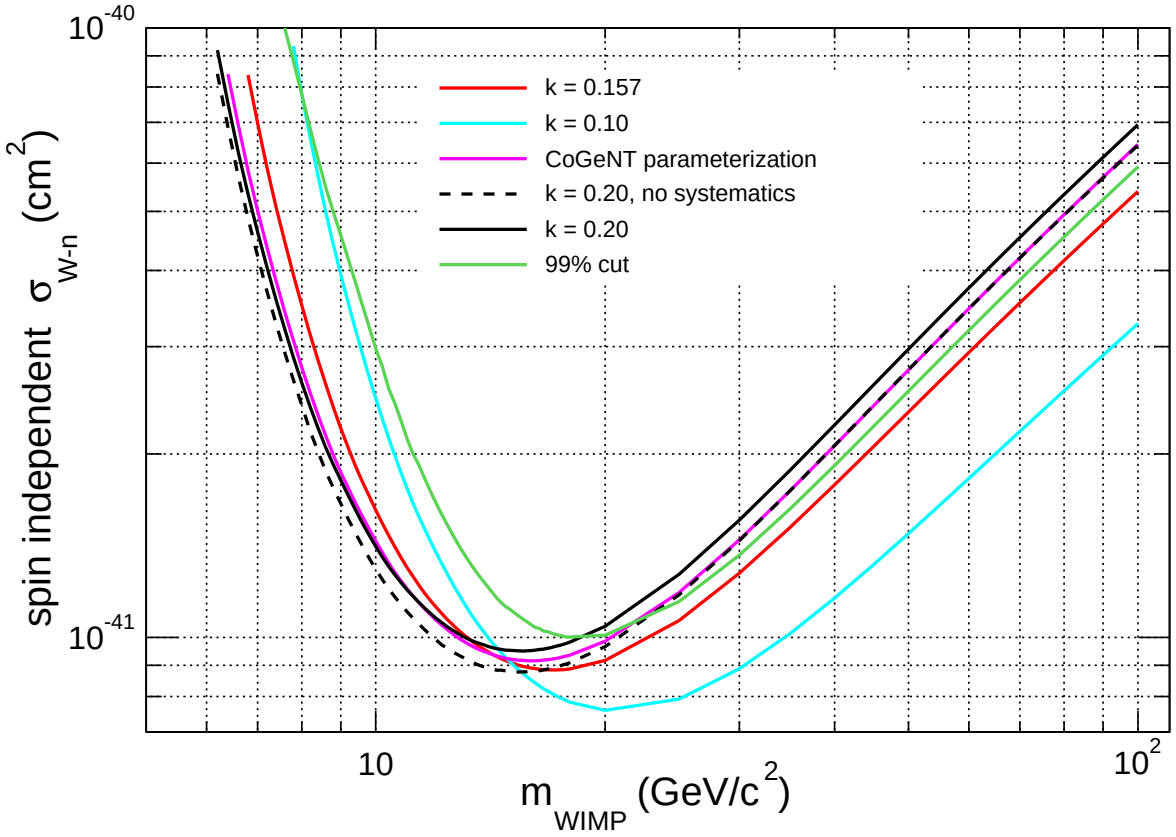

Figure 5.10: 90% C.L. WIMP exclusion curves from the 89.5 kg-d dataset. The black curves use a parametrization of Lindhard theory with $k = 0.20$ for the quenching factor. The black dashed curve includes no systematic uncertainties. The red curve uses a parameterization of Lindhard theory with $k = 0.20$, the light blue curves uses $k = 0.1$, and the magenta curve uses the parameterization from CoGeNT [30]. The green curve shows the MALBEK limit from [33] that uses a 99% slow event acceptance cut and the CoGeNT quenching factor parameterization.

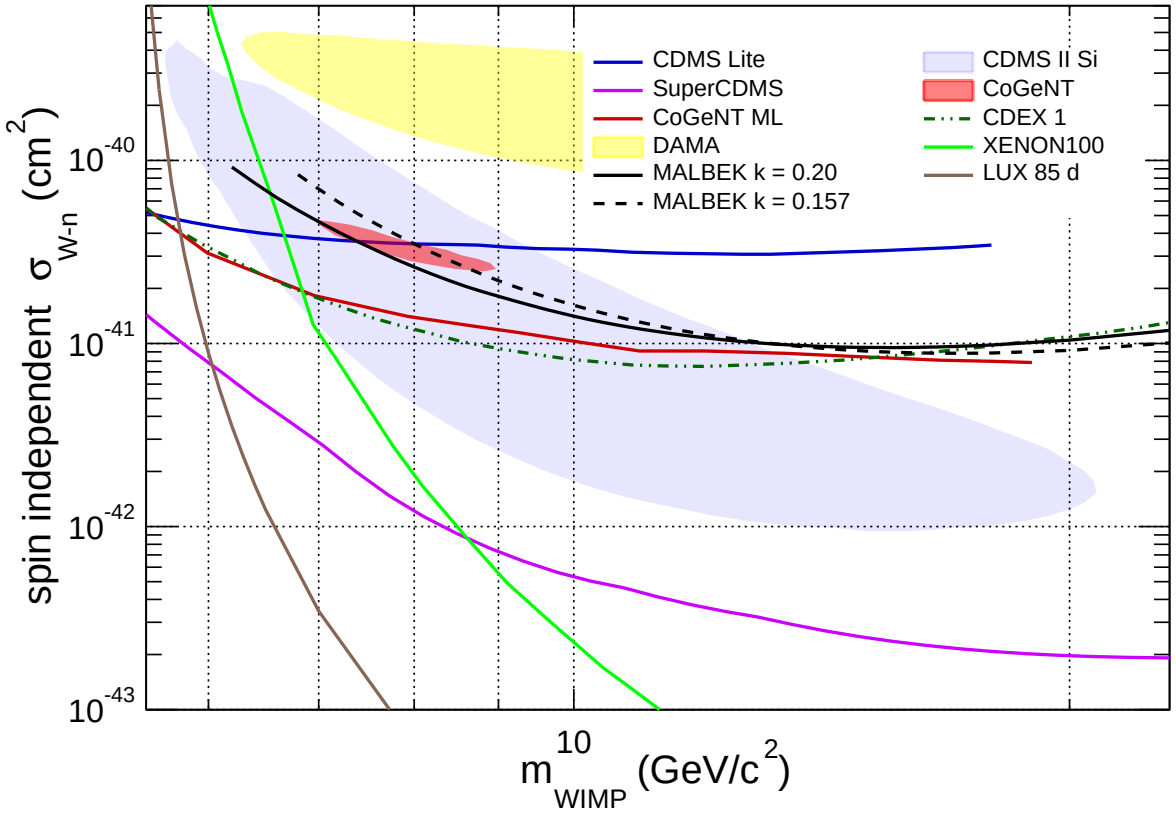

Figure 5.11: 90% C.L. MABLEK WIMP exclusion limit compared to WIMP limits from the CoGeNT maximum likelihood analysis [21], CDEX-1 [59], LUX [26], CDMS Lite [27], SuperCDMS [83], and XENON100 [85] and WIMP signal regions from DAMA [84], CDMSII-Si [25], and CoGeNT [30].

Section 5.3: Search for Solar Axions

The strong force described by quantum chromodynamics (QCD) has a CP-violating term in the Lagrangian, the strength of which is fixed by a complex phase. To explain the apparent lack of CP-violation in strong interactions, Roberto Peccei and Helen Quinn postulated a new global $U(1)$ symmetry that is spontaneously broken at a high-energy scale [87] and produces a term that cancels the problematic one. The Peccei-Quinn solution to the strong CP problem also produces a particle, the axion, the properties of which were discussed in the context of the Standard Model in 1978 in independent articles by Weinberg [88] and by Wilczek [89].

The standard axion from the Peccei-Quinn solution, which has a symmetry breaking scale, f_A, comparable to the electroweak symmetry breaking scale, was quickly ruled out by early experiments. In light of these results, models for an "invisible" axion were introduced with f_A much larger than the electroweak symmetry breaking scale. Kim [90] and Shifman, Vainstein, and Zakharov [91] proposed a model in which the axion couples directly to hadrons and photons but only couples to electrons through a radiatively-induced axion-electron coupling at the one-loop level (the KSVZ model). Zhitnitsky [92] and Dine, Fischler, and Srednicki [93] introduced a model in which the axion couples directly to hadrons, photons, and electrons (the DFSZ model).

While the coupling strength of the axion to photons ($g_{A\gamma}$), electrons (g_{Ae}), and nucleons (g_{AN}) is model dependent, the mass of the invisible axion, m_a, is consistently defined as being inversely proportional to the Peccei-Quinn symmetry breaking scale, f_A,

$$m_a = \frac{f_\pi m_\pi}{f_A}\left(\frac{z}{(1+z+w)(1+z)}\right)^{1/2} \simeq 6.0(\text{eV})\frac{10^6(\text{GeV})}{f_A(\text{GeV})}. \tag{5.12}$$

where $f_\pi = 93$ MeV is the pion decay constant, $z = m_u/m_d \simeq 0.56$ is the ratio of the masses of the up and down quarks, and $w = m_u/m_s \simeq 0.029$ is the ratio of the masses of the up and strange quarks. If axions couple to electrons, either directly or radiatively, they would

be produced in the solar core by atomic recombination and de-excitation, bremsstrahlung, and Compton-like scattering [94] and could be observable in a low-background detector via the axio-electric effect, an analog of the photo-electric effect.

A model independent search for the axio-electric absorption of solar axions was performed using the 89.5 kg-d MALBEK dataset. This analysis places a constraint on the electron axion coupling, g_{Ae}, which can be converted within the context of a particular model to a symmetry breaking scale. In the DFSZ model, the axion electron coupling is related to the symmetry breaking scale by

$$(g_{Ae})_{DFSZ} = \frac{m_e}{3f_A}\cos^2\beta_{DFSZ} \tag{5.13}$$

where $\cos^2\beta_{DFSZ}$ parameterizes the relative size of the vacuum expectation values that comprise the axion in the DFSZ model. It is customary to set $\cos^2\beta_{DFSZ} = 1$. In the KSVZ model, where the axion only radiatively couples to electrons, g_{Ae} is smaller by a factor of $\sim \alpha^2$. In this case, a constraint on g_{Ae} only weakly limits possible axion mass values.

Axions coupling to photons or nucleons introduces the possibility of alternative solar axion production mechanisms. An effective axion-photon coupling would result in axions produced by inverse Primakoff conversion. These axions could be detected in a crystal detector via the Primakoff effect, with the signal modulating as the orientation of the detector's crystal axes change relative to the position of the sun [95, 96]. There is an ongoing program within the MAJORANA collaboration to determine the crystal axes of the DEMONSTRATOR PPCs and perform a search for Primakoff generated solar axions with the DEMONSTRATOR. If axions couple to nucleons, axions would be emitted during the de-excitation of thermally excited nuclei. The largest flux of solar de-excitation axions would come from the M1 transition of ^{57}Fe nuclei [97] and could be detected by resonant absorption on an iron target [98], or, for a non-zero axion-electron coupling, as a 14.4 keV peak in the detector spectrum. The MALBEK background at 14.4 keV is approximately an order of magnitude larger than the EDELWEISS detector [96], which sets the strictest limit on a 14.4 keV axion peak, but the DEMONSTRATOR should have better sensitivity to this type of solar axion. The DEMON-

STRATOR may also search for axions that were produced early in the Universe and comprise some portion of the dark matter halo. Recent searches for a galactic dark matter axion-like particles (ALPs) can be found in [95, 96, 99, 100].

5.3.1: Expected Signal

The expected signal rate from a solar axion is

$$\frac{dN_{obs}}{dE} = \sigma_{Ae} \left(\frac{d\Phi}{dE_a}^{atomic} + \frac{d\Phi}{dE_a}^{brem} + \frac{d\Phi}{dE_a}^{Comp} \right) \Bigg|_{E=E_A} \tag{5.14}$$

where E_a is the axion energy, σ_{Ae} is the cross section for the axio-electric absorption of axions, and $\frac{d\Phi}{dE_a}$ is the differential axion flux from a given production mechanism.

$$\sigma_{Ae} = \sigma_{pe}(E_A) \frac{g_{Ae}^2}{\beta_A} \frac{3E_A^2}{16\pi\alpha m_e^2} \left(1 - \frac{\beta_A^{2/3}}{3} \right). \tag{5.15}$$

In Equation 5.15, $\sigma_{pe}(E_A)$ is the photoelectric cross section in germanium as a function of the axion energy, β_A is the axion velocity over the speed of light, and α is the fine structure constant [101]. Both σ_{Ae} and the differential axion flux depend on g_{ae}^2, so the axion interaction rate goes as the fourth power of the axion electron coupling. Figure 5.12 shows the axio-electric cross section for an axion with a 5 keV mass and an axion at the massless limit. The discontinuities in the cross section evident in Figure 5.12 occur at germanium electron shell energies.

Because the solar interior is relatively well understood, the differential flux of axions can be calculated with high precision [94]. Early calculations of the axion solar flux neglected atomic processes, which were thought to be sub-dominant because of the small amount of elements heavier than helium in the sun [102]. However, atomic process have much larger cross sections than Compton scattering and bremsstrahlung which helps offset the low abundance of heavier elements. Based on this, later calculations included atomic axio-recombination but

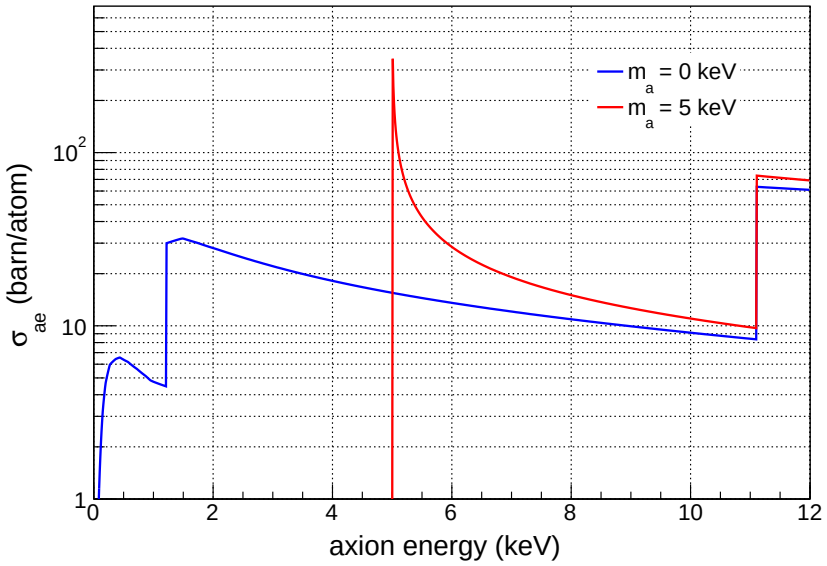

Figure 5.12: Axio-electric cross section of germanium for an ultra-relativistic axion (red) and a 5 keV axion (blue). The discontinuities in the cross section correspond to electron shell energies in germanium.

neglected to include atomic-de-excitation [103, 104]. A recent calculation by Redondo [94] includes both atomic processes as well as Compton scattering and bremsstrahlung and finds a solar axion flux $\sim 30\%$ higher than previous results. The total calculated flux from Redondo valid for a sub-keV axion with $g_{Ae} = 1$ is shown in Figure 5.13.

5.3.2: Results

The search for a signal from solar axions is performed using the profile likelihood ratio method described in Section 5.2.2 over the energy region between 1.5 keV and 8 keV. This region sits between the 1.3 keV ^{68}Ge L-capture peak and the ^{65}Zn K-capture peak. Consistent results were found using an expanded energy range that included these peaks. The background model used for this analysis includes a flat continuum, the ^{49}V K-capture peak (4.96 keV), and the ^{55}Fe K-capture peak (6.55 keV). The signal model is created by generating a histogram from Equation 5.14 for a particular axion mass m_A, convolving the spectrum with the measured detector resolution, and building a pdf by sampling the normalized, smeared histogram. This is repeated for each axion mass of interest. The likelihood

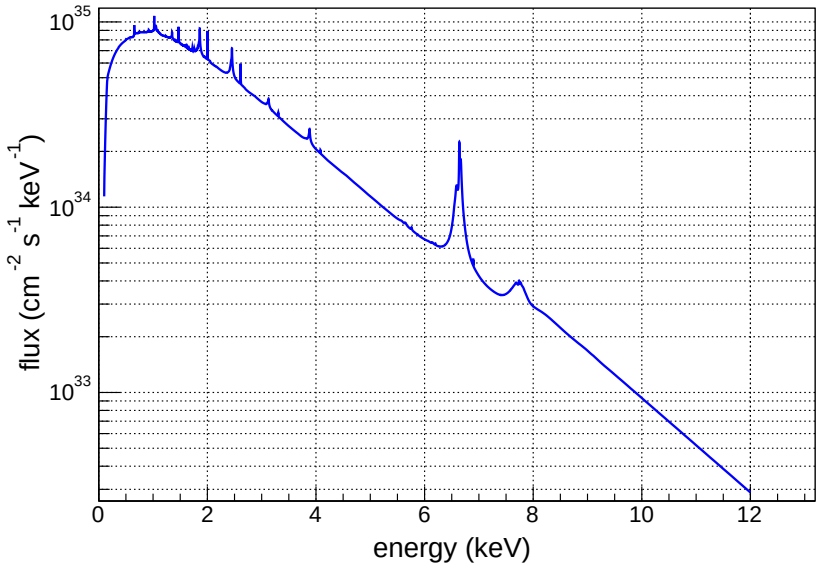

Figure 5.13: Calculated solar axion flux for a sub-keV mass axion with $g_{Ae} = 1$ from [94].

function is constructed from the following pdfs:

- Flat background: $f_{flat}(E) = 1$
- K-shell background peaks: $f_{peak_i} = \frac{1}{\sigma_i\sqrt{2\pi}} \exp\left(-\frac{(E-\mu_i)^2}{2\sigma_i^2}\right)$
- Signal pdf generated from signal spectrum - f_{signal}

A parameter that describes the number of events in each feature, N_{flat}, N_i, and N_{signal}, is included in the likelihood function in an extended likelihood term, Poisson $(\sum_x N_x, N_{obs})$, where the sum is over the pdfs. The number of events in each pdf is allowed to float freely during the analysis.

Because of the small uncertainty on the detector linearity in this energy range, the position of the K shell peaks are fixed. Based on the results from Figure 5.4, the peak widths are allowed to float independently during the fit.

There are two uncertainties that directly affect the exposure of the experiment. The first is the 3.7% uncertainty in the detector volume described in Section 5.1.3. The second arises from the signal acceptance of the slow event cut. At the 1.5 keV analysis threshold, the slow event cut removes 21.5% of the signal events. This value will be conservatively

used as the uncertainty on the slow event acceptance over the entire energy range. Both the volume uncertainty and slow event acceptance uncertainty manifest as an error in the total signal efficiency. They are added in quadrature and included in the likelihood function as a Gaussian constraint $0.5([\eta - 1]/0.218)^2$ on η, the total signal efficiency. The extended likelihood function including this term is

$$-\log\mathcal{L} = -\log\left(\text{Poisson}\left(\sum_x \eta N_x, N_{obs}\right)\right) - \sum_n \log\left(\frac{1}{\sum_x N_x}\left(\sum_x N_x f_x\right)\right) - 0.5\left(\frac{\eta - 1}{0.218}\right)^2, \tag{5.16}$$

where the sum over n is over each event in the energy region, the sums over x include all of the background and signal pdfs. A summary of the parameters used in the fit, their allowed values, and the systematic uncertainty used to constrain the values can be found in Table 5.4.

Table 5.4: Parameters used in the solar axion analysis, their allowed ranges, and, when relevant, the systematic uncertainty used to constrain the value. The allowed ranges for the number of events in each pdf were chosen so that the parameters never reached the range boundary during the analysis.

Parameter	**Value**	**Uncertainty**
V K-capture mean, μ_{Zn}	4.96 keV	fixed
V K-capture width, σ_{Zn}	$0 \rightarrow 1$ keV	
Fe K-capture mean, μ_{Ga}	6.55 keV	fixed
Fe K-capture width, σ_{Ga}	$0 \rightarrow 1$ keV	
N_V	$0 \rightarrow 10^4$	
N_F	$0 \rightarrow 10^4$	
N_{flat}	$0 \rightarrow 10^4$	
N_{signal}[†]	$-20 \rightarrow 10^4$	
Signal efficiency, η	1	21.8%

[†] range includes unphysical values to prevent fits at the parameter boundary

This analysis will only consider axions with masses between zero and 1 keV, the maximum mass for which the solar axion flux predicted in [94] is valid. Because the 1.5 keV analysis threshold falls above the maximum axion mass, there is little variation in the expected signal rate between a 1 keV axion and a massless axion. For this reason, only a small selection of axion masses were considered, $m_A = 0$ keV, $m_A = 0.1$ keV, and $m_A = 1.0$ keV. The profile likelihood curves calculated for a massless axion are shown in Figure 5.14. Neither curve shows statistically significant evidence for a solar axion signal and upper limits are placed on the axion-electron coupling. Without including systematic uncertainties, values of $g_{Ae} > 2.5 \times 10^{-11}$ are excluded at the 90% C.L. When the Gaussian constraints are included in the likelihood function, the limit on the number of axio-electric events is considerably less strict, but because the axion-electron coupling constant goes as the event rate to the fourth power, the 90% C.L. exclusion is only slightly weaker, excluding values of $g_{Ae} > 2.6 \times 10^{-11}$. The signal for an ultra-relativistic solar axion with $g_{Ae} = 2.6 \times 10^{-11}$ is shown in Figure 5.15 along with the best fit of the background model for that coupling.

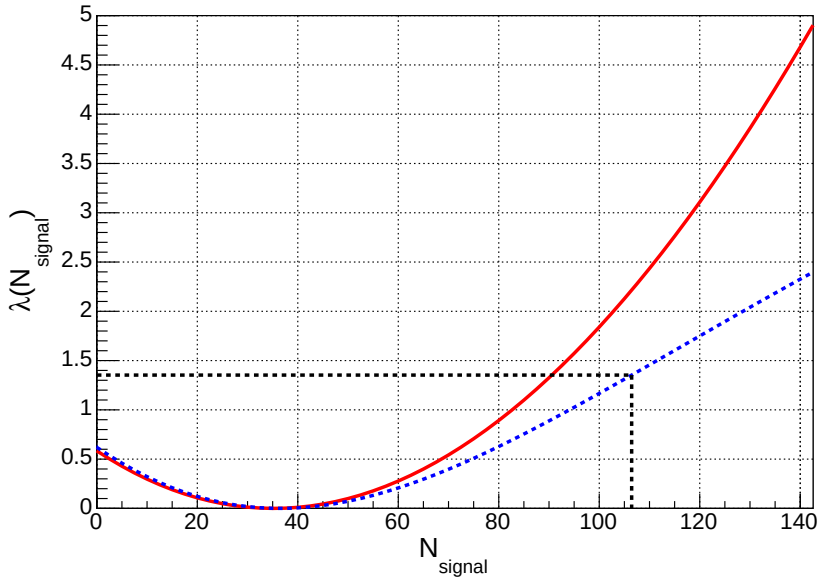

Figure 5.14: Profile likelihood curves for the number of axion events between 1.5 and 8 keV. The blue dashed curve includes the systematic uncertainties described in the text. The red curve does not. The 90% C.L. including the systematic uncertainties is indicated by the black dashed lines.

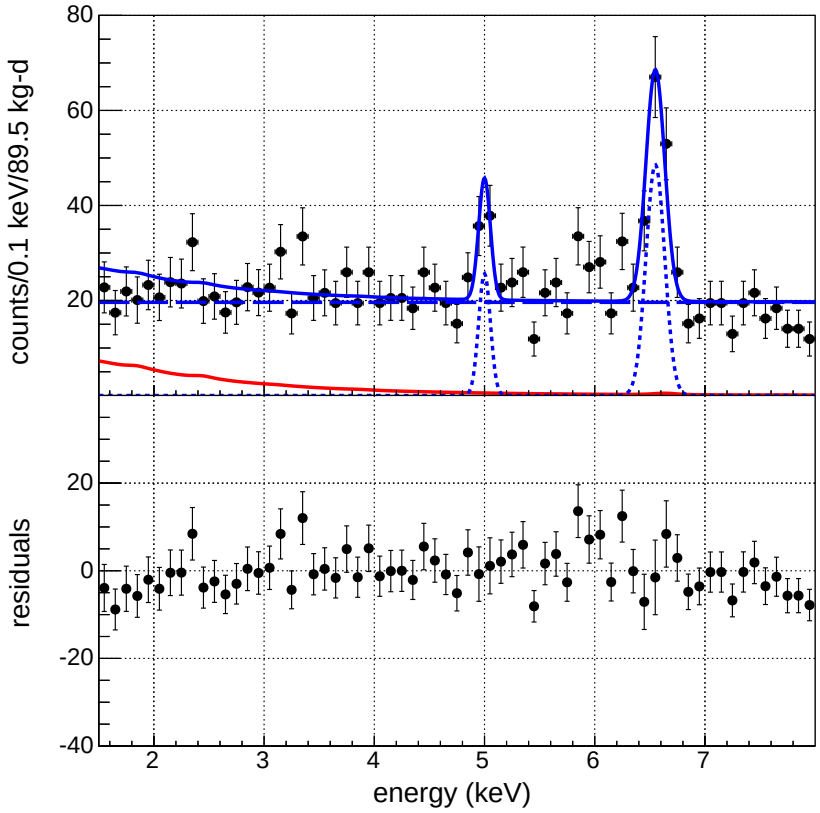

Figure 5.15: Fit of a sub-keV mass solar axion (red) with an axion-electron coupling fixed at the 90% exclusion limit to the MALBEK 89.5 kg-d dataset. The fit model (blue) includes the axion signal, a flat background (blue dashed), and the ^{49}V and ^{55}Fe K-capture peaks (blue dotted). The fit residuals are shown in the bottom panel.

The results of this analysis are shown in the context of other experimental limits and astrophysical bounds on g_{Ae} in Figure 5.16. The best experimental limits come from XENON100, which looks for axio-electric interactions within a 62 kg, dual-phase liquid xenon time projection chamber (TPC) and excludes $g_{Ae} > 7.7 \times 10^{-12}$ [100]. The exclusion from MALBEK, which has a considerably lower exposure and higher background rate in the region of interest than XENON100, is comparable to the experimental limits from EDELWEISS, who use 357 kg-d of data collected with ten 400 g low temperature germanium detectors to exclude $g_{Ae} > 2.56 \times 10^{-11}$ [96]. MALBEK is also similar in sensitivity to indirect limits derived from the observation of solar neutrinos by the Sudbury Neutrino Observatory, which constrains non-standard energy loss mechanisms in the sun to less than 10% of the sun's photon luminosity [105].

The MAJORANA DEMONSTRATOR will have approximately 100 times the mass of MALBEK and a significantly lower background rate in the axion region of interest. Following the background assumptions presented in [51], a 100 kg-yr DEMONSTRATOR exposure has a projected sensitivity to massless solar axions with $g_{ae} > 6.5 \times 10^{-12}$ at 95% C.L., a factor of four improvement in sensitivity over MALBEK. The experiment may be able to increase its solar axion discovery potential by utilizing the model-independent annual modulation in the sun-to-earth distance. The solar axion flux is proportional to $\Omega = 1/(4\pi d^2)$, which is 6.68% larger in January than in July. The time dependent rate is

$$R(t) = R_{BG} + NI(\Phi\sigma)\Big[1 + \eta \sin(\omega t + \delta)\Big], \tag{5.17}$$

where $I(\Phi\sigma)$ is the integral of the flux and cross section over the energy range of interest, R_{BG} is the background rate, N is the number of target atoms, and η is the amplitude of the modulation. If $\eta NI(\Phi\sigma) \ll R_{BG}$, discovery potential vanishes in all practicality and bounds established with even a significant dataset have no real impact.

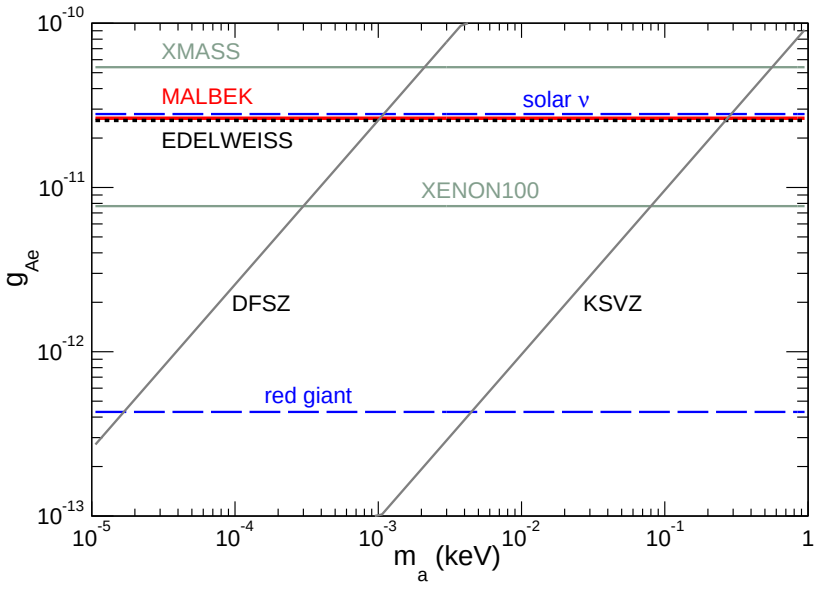

Figure 5.16: Experimentally excluded regions of the model independent axio-electric coupling (g_{Ae}) from MALBEK, XMASS [106], EDELWEISS [96], and exclusions from astronomical observations, solar neutrinos [105] and red giants [107]. The DFSZ and KSVZ solar axion predictions are also shown.

Section 5.4: Search for Pauli Exclusion Principle Violating Decays

In 1925, Wolfgang Pauli postulated the exclusion principle to describe the periodic nature of the elements. The Pauli exclusion principle (PEP) states that there can never be two or more equivalent electrons in an atom or, in the language of Quantum Field Theory (QFT), no two identical fermions can occupy the same quantum state. The Pauli exclusion principle is a fundamental law of nature, but its physical origin is still not well understood. The discovery of parity non-conservation in 1957 [108] spurred a new set of experiments testing fundamental laws. This included a search for PEP transitions of atomic electrons in iodine by Reines and Sobel in 1974 [109], who gave a lower limit on the lifetime for a non-Paulian electron transition of 2×10^{27} seconds. Following this pioneering work, many searches have been done for atoms and nuclei in Pauli exclusion principle violating states.

Despite early efforts to construct models that incorporate PEP violation [110, 111], there is no established theoretical framework for Pauli exclusion principle violation. The most promising theory that allows small violations of Fermi statistics is quon theory [112], which,

despite many positive properties, violates locality [113]. The situation is further complicated as pointed out by Amado and Primakoff, who noted that even if there is a small mixed symmetry component in a primarily antisymmetric wavefunction, the Hamiltonian would only connect a mixed state to another mixed state. Meaning that even if the exclusion principle is violated, PEP violating transitions of electron or nucleons to lower orbitals would still be forbidden [114].

In light of this constraint, Elliott et al. developed a scheme for categorizing PEP violation experiments based on the "newness" of the fermion in the system [115], i.e. the time at which the fermion interacts with the nucleus or atom and establishes the symmetry of the wavefunction. Type-I experiments involve a fermion that has never interacted with another system. This could be a fermion created during the big bang that forms an anomalous nuclear state [116] or an electron emitted during β decay or pair production that undergoes a PEP violating capture by an atomic system [117]. Type-II experiments use fermions that previously existed but have never interacted with the system. The method used by Ramberg and Snow [118] and Elliott et al. [115] to perform this type of experiment is to run a current through a conductor and look for PEP-violating electron captures of new electrons from the current source. Type-III experiments look for PEP-violating transition of an atomic electron or nucleon in an existing system. A theoretical description of this type of PEP-violation contradicts Amado and Primakoff or requires the use of extra-dimensions, electronic substructure, or other exotic physics [119, 120]. The results from PEP-violation experiments are compared using the parameter $\frac{1}{2}\beta^2$, the probability that two fermions form a state with a symmetric wave function component. As Elliott points out, this is a simplistic method of comparing experiments and warrants the wide variety of approaches used to search for PEP-violation. A comprehensive table of existing experimental results and their classification is given in [115].

MALBEK is sensitive to the transition of an L-shell germanium electron into an already full K-shell, a Type-III PEP violating atomic transition. The most stringent constraint

on this type of PEP violation comes from the DAMA/LIBRA experiment, a 250 kg array of radio-pure NaI(Tl) detectors at the Gran Sasso National Laboratory. DAMA/LIBRA searched for K-shell transitions in iodine using 0.53 ton-years of data and set a limit on the lifetime of 4.7×10^{30} seconds at 90% C.L. [121].

5.4.1: Expected Signal

A PEP violating transition of an L-shell electron into the fully occupied K-shell would deposit roughly the same energy as a standard K_α transition. However, due to the increased shielding of the nuclear charge from the second electron in the K-shell, the energy of the transition is shifted down slightly. Mau Chen has calculated the x-ray energy of a PEP violating K-shell transition to be 9.543 keV in germanium [115]. When measuring this decay with a HPGe detector, the x-ray energy sums with the emissions from the further relaxation of the atomic shells, creating a feature at 10.6 keV, on the high energy shoulder of the ^{68}Ge K-shell capture line. Because the probabilities of the x-ray or the associated relaxation emissions escaping the detector are vanishingly small, the efficiency for detecting a PEP violating K_α transition occurring within the detector active volume is effectively 100%.

5.4.2: Model and Fit Results

The search for PEP-violating K-shell transitions within the MALBEK detector is performed using the profile likelihood ratio method described in Section 5.2.2. Data that fall between 7.5 and 12.0 keV are used for the analysis. This region includes enough featureless continuum above and below the K-capture peaks to constrain the flat component of the background model. The ^{65}Zn and ^{68}Ga peaks are included because of their proximity to the ^{68}Ge peak. If the energy region containing these peaks is not used in the fit, the rate in the continuum below the ^{68}Ge peak is not well defined and the quality of the fit suffers, which in turn reduces the sensitivity of the experiment. Increasing the fit region beyond 7.5 or 12 keV does not affect the final result.

The model used for the analysis includes the ^{65}Zn (8.98 keV), ^{68}Ga (9.66 keV), and ^{68}Ge (10.37 keV) K-shell capture peaks and a flat continuum, each described by a set of nuisance parameters, and a signal component consisting of a single gaussian at 10.6 keV. The likelihood function is constructed from the following pdfs:

- Flat background: $f_{flat}(E) = 1$
- K-shell background peaks: $f_{peak_i} = \frac{1}{\sigma_K\sqrt{2\pi}} \exp\left(-\frac{(E-\mu_i)^2}{2\sigma_K^2}\right)$
- Signal peak: $f_{signal} = \frac{1}{\sigma_K\sqrt{2\pi}} \exp\left(-\frac{(E-10.6)^2}{2\sigma_K^2}\right)$

Each pdf has a corresponding parameter that describes the number of events in the pdf, N_{flat}, N_i, and N_{signal}. These parameters are allowed to float without constraint during the analysis and an extended likelihood term, Poisson $(\sum_x N_x, N_{obs})$, where the sum is over the pdfs, is added to the likelihood function.

The location of the K-shell peaks and the signal peak are fixed during the analysis because of the negligible, less than 0.2%, uncertainty in their position. Figure 5.4 shows the width of the peaks in the low energy region fit to an empirical resolution function, Equation 5.10. The measured ^{68}Ga peak width deviates from Equation 5.10 by 30%. Based on this, the peak width is allowed to float within a 30% Gaussian constraint during the analysis. A term $0.5([\sigma_K - \sigma_{K,0}]/0.3\sigma_0)^2$ is added to the log likelihood function for the peak resolution σ_K with expected value $\sigma_{K,0}$. An additional Gaussian constraint, $0.5([\eta - 1]/0.037)^2$, is added to the log likelihood function to incorporate the 3.7% systematic uncertainty in the volume of the detector, which modifies the signal efficiency, η. The extended likelihood function, including the extended likelihood term and the constraints, is

$$-\log\mathcal{L} = -\log\left(\text{Poisson}\left(\sum_x \eta N_x, N_{obs}\right)\right) - \sum_n \log\left(\frac{1}{\sum_x N_x}\left(\sum_x N_x f_x\right)\right) - 0.5\left(\frac{\sigma_K - \sigma_{K,0}}{0.3\sigma_{K,0}}\right)^2 - 0.5\left(\frac{\eta - 1}{0.037}\right)^2, \quad (5.18)$$

where the sum over n is over each event in the energy region and the sums over x include all of the background and signal pdfs. A summary of the parameters used in the fit, their allowed values, and the systematic uncertainty used to constrain the values can be found in Table 5.5.

Table 5.5: Parameters used in the PEP-violating transition analysis, their allowed ranges, and, when relevant, the systematic uncertainty used to constrain the value. The allowed ranges for the number of events in each pdf were chosen so that the parameters never reached the range boundary during the analysis.

Parameter	**Value**	**Uncertainty**
Zn K-capture mean, μ_{Zn}	8.98 keV	fixed
Ga K-capture mean, μ_{Ga}	9.66 keV	fixed
Ge K-capture mean, μ_{Ge}	10.37 keV	fixed
Signal mean, μ_{signal}	10.60 keV	fixed
Peak width, σ_K	0.117 keV	30%
N_{Zn}	$0 \rightarrow 10^4$	
N_{Ga}	$0 \rightarrow 10^4$	
N_{Ge}	$0 \rightarrow 10^4$	
N_{flat}	$0 \rightarrow 10^4$	
N_{signal} [†]	$-20 \rightarrow 10^4$	
Signal efficiency, η	1	3.7%

[†] range includes unphysical values to prevent fits at the parameter boundary

The best fit value for the PEP-violating peak, which is allowed to float to unphysical values to avoid discontinuities in the profile likelihood ratio at the parameter boundary, is -0.17 counts/kg-d. Following the method described is Section 5.2.2, N_{signal} is set to zero and the maximum likelihood value at this point is used to construct the profile likelihood ratio. The resulting profile likelihood curves are shown in Figure 5.17. The profile likelihood curve with no systematic uncertainties included in the likelihood function excludes N_{signal} greater than 0.084 counts/kg-d at the 90% C.L. The blue curve shows $\lambda(N_{signal})$ when the peak resolutions and detector efficiency are allowed to float within the constraints included in the

likelihood function. This results in a slightly weaker 90% C.L. exclusion of 0.128 counts/kg-d. The decrease in sensitivity is driven most significantly by the uncertainty in the peak resolution, σ_K, which decreases to accommodate larger N_{signal} values.

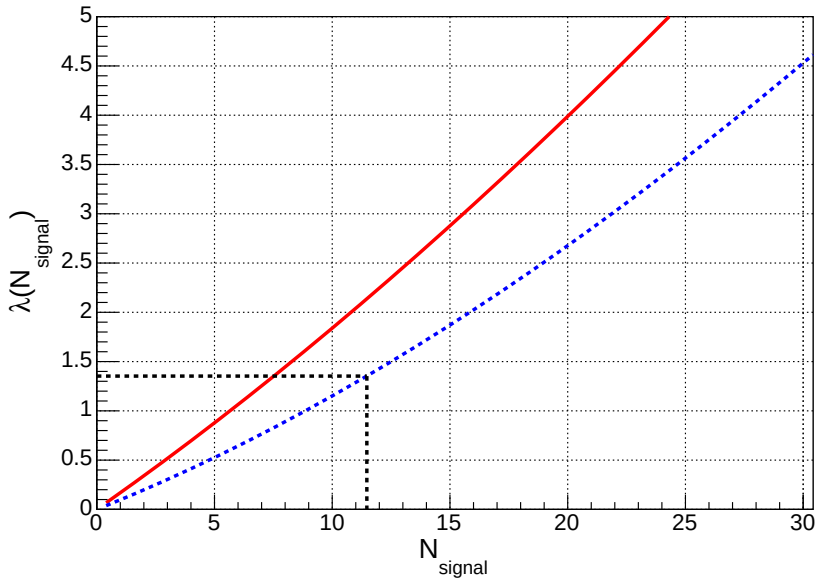

Figure 5.17: Profile likelihood curve without (red) and with (blue dashed) the systematic uncertainties described in the text. The 90% C.L. exclusion on N_{signal}, the number of events in the PEP violating atomic transition peak, is indicated by the black dashed lines.

The best fit of the constrained model to the data with N_{signal} fixed at the 90% C.L. is shown in Figure 5.18. This result corresponds to a PEP-violating K_α transition lifetime of 5.6×10^{30} seconds at a 90% C.L., comparable to the limit reported by the DAMA/LIBRA collaboration of 4.7×10^{30} seconds for iodine K-shell transitions, despite a much lower exposure time. The MALBEK detector is competitive with this result due to its significantly better energy resolution at the region of interest, 9.4% for DAMA/LIBRA versus 1.0% for MALBEK. To enable a comparison to other types of experiments searching for PEP-violating states, $\frac{1}{2}\beta^2$ can be calculated by comparing the PEP-transition lifetime to the 1.7×10^{-16} second lifetime of a standard K_α transition in germanium, resulting in a limit of $\frac{1}{2}\beta^2 < 3.04 \times 10^{-47}$. While this is competitive with other Type-III experiments looking for PEP violating atomic transitions, Type-III experiments looking for PEP-violating nuclear transitions are many orders of magnitude more sensitive, see for example [121].

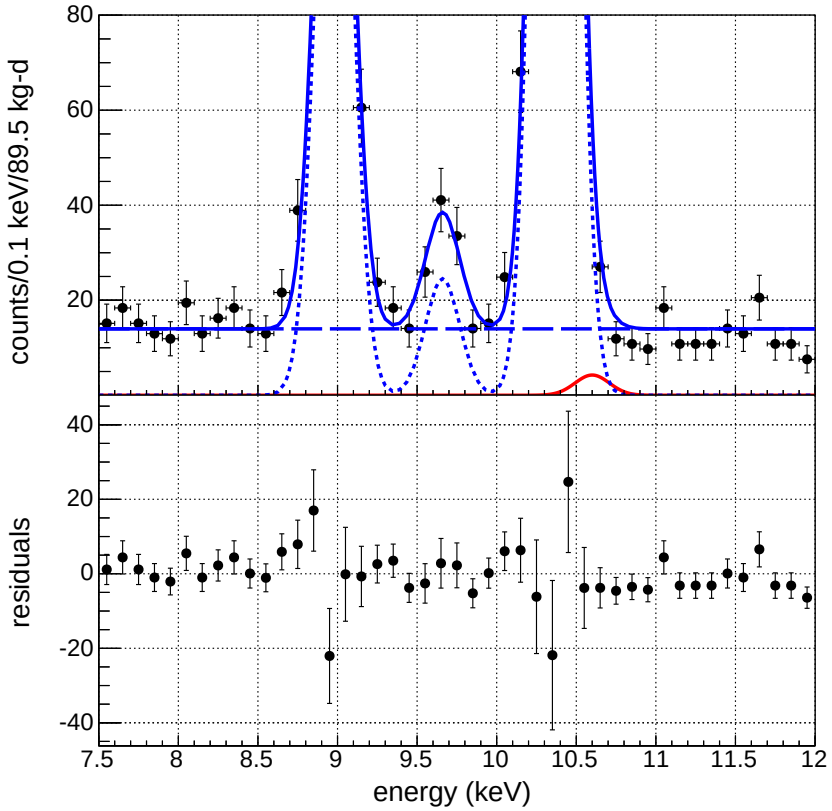

Figure 5.18: Fit of the signal plus background model (blue) with N_{signal}, the number of events in the PEP-violating decay peak, fixed at the 90% C.L. exclusion limit. The PEP-violating peak (red) has a rate of 0.128 PEP-violating events/kg/day. The background model includes the ^{68}Ge, ^{68}Ga, and ^{65}Zn K-capture lines (blue dotted) and a flat continuum (blue dashed). Fit residuals are shown in the bottom panel.

CHAPTER 6: Conclusions

Section 6.1: Summary of Results

The MALBEK detector operated underground at KURF for almost three years. During this time it proved a useful tool for evaluating the long-term performance of PPC detectors and gave the MAJORANA collaboration valuable experience operating a low-background HPGe detector in a remote underground environment. The ease of deploying sources around the detector cryostat made MALBEK an excellent resource for studying sources of background in a PPC, both at energies relevant for a $0\nu\beta\beta$ search [31] and in the region of interest for WIMPs, solar axions, and other hypothetical rare processes. The analysis and simulation tools developed in this dissertation as well as in [33] and [31] are already being used with commissioning data from the DEMONSTRATOR, and the development of the MALBEK data acquisition system and calibration techniques have informed the design and implementation of the DEMONSTRATOR electronics and commissioning plan.

It was found that slow surface events dominate the MALBEK background event rate below 1 keV. Surface events below approximately 2 keV are difficult to identify because of the poor signal-to-noise ratio near the detector energy threshold. If unaccounted for, surface events can reduce the detector's sensitivity to possible signals from WIMPs, solar axions, and forbidden decays. This is further complicated by the fact that the energy distribution of surface events is similar to that expected from WIMP-nuclear recoils. In Chapter 3, an approach to surface event identification based on the wavelet power spectrum first proposed in [33] was studied in detail. Based on these results, a data selection strategy was adopted that emphasizes removing surface events over maximizing signal efficiency. This is in contrast to the approach taken by two other collaborations operating PPC detectors to look for

WIMPs, TEXONO/CDEX [59] and CoGeNT [30], the latter of which sees an excess of events and an annual modulation that could be due to an approximately 10 GeV WIMP.

In addition to the analysis of surface event distributions, Chapter 4 describes a study of surface event formation done using a model proposed by David Radford. The salient features of the model were studied and the model was optimized to match calibration data collected with MALBEK. The simulation agrees relatively well with data, suggesting a promising path forward for developing a complete model of surface event backgrounds.

Sources of background other than surface events and the possible systematic effects relevant for rare-event searches using MALBEK were discussed in Chapter 5. The 89.5 kg-d MALBEK dataset was used to set limits on three hypothesized rare processes. Limits were placed on spin-independent WIMP-nucleon scattering for WIMPs with masses ranging from 5 to 100 GeV. These results are in tension with the signal regions from CoGeNT [30] and DAMA [84] but are significantly weaker than results from dedicated, larger mass experiments. MALBEK also placed model independent limits on the axion-electron coupling of solar axions, finding $g_{Ae} > 2.6 \times 10^{-11}$. This result is comparable to results from the EDELWEISS [96] experiment and indirect limits from solar neutrinos [105] but significantly weaker than limits derived from the larger mass XENON100 TPC [100]. A final analysis was performed searching for PEP violating atomic electron transitions. A limit of 5.6×10^{30} seconds was placed on the lifetime of this process .

Section 6.2: Extensions

The sensitivity of future measurements using the MALBEK detector could be improved in several ways. The slow event removal cut is responsible for the dominant systematic uncertainty in the analyses presented in Chapter 5. Slow event identification might be improved by decreasing the electronic noise in the data acquisition system. An improved and validated slow event simulation could also reduce the slow event cut systematic error. Validation of the slow event simulation would require additional data, including collimated

source scans of the detector surface, preferably repeated for several detectors with different geometries and surface contact formation techniques. It would also be instructive to compare simulated event drift times to data collected using the coincident event tagging technique presented in [33].

The MALBEK data acquisition system and slow control infrastructure perfomed well during data taking. However, power outages at KURF required re-biasing of the detector and reduced the long-term stability of the system. An uninterruptible power supply could be used to keep the detector running during power glitches. The MALBEK reset preamplifier induces a complicated rate and energy dependent efficiency. While not significant below 10 keV, this does complicate the interpretation of data collected at higher energies [31]. Outfitting the detector with a resistive feedback preamplifier would eliminate this problem. Reducing the MALBEK background rate would require significant reworking of the cryostat and internal detector components, although an active muon veto could be used to minimize the already sub-dominant contribution from muon-induced neutrons.

Section 6.3: Outlook

The Majorana Demonstrator will operate with 40 kgs of PPC detectors and a projected background rate below 10 keV more than two orders of magnitude lower than the MALBEK detector. While the Demonstrator will not be competitive with dedicated large-mass WIMP experiments like LUX [26] or SuperCDMS [27], it will be capable of making a model independent test of the CoGeNT result [30] and, because of the reduced background rate, may be able to do so without relying on a surface event removal cut. The Demonstrator should also have sensitivity to solar axions and dark matter ALPs comparable to current limits from XENON100 [100] and can search for additional solar axion signals due to axions emitted during nuclear de-excitations and axions produced by inverse Primakoff conversion. Lastly, the Demonstrator should be able to improve upon the limit placed in this dissertation on PEP violating electron transitions.

BIBLIOGRAPHY

[1] K. Olive *et al.*, "Review of Particle Physics," *Chin. Phys.* **C38** (2014) 090001.

[2] C. Kraus, B. Bornschein, L. Bornschein, J. Bonn, B. Flatt, A. Kovalik, B. Ostrick, E. Otten, J. Schall, T. Thummler, and C. Weinheimer, "Final results from phase II of the Mainz neutrino mass search in tritium β decay," *Eur. Phys. J. C* **40** no. 4, (2005) 447–468.

[3] J. Dunkley and others, "Five-Year Wilkinson Microwave Anisotropy Probe (WMAP) Observations: Likelihoods and Parameters from the WMAP data," *Astrophys. J. Suppl. S.* **180** no. 2, (2009) 306–329.

[4] Planck Collaboration, "Planck 2013 results. XVI. Cosmological parameters," *A. & A.* **571** (2014) A16.

[5] C. Weinheimer, "KATRIN, a next generation tritium β decay experiment in search for the absolute neutrino mass scale," *Prog. Part. Nucl. Phys.* **48** no. 1, (2002) 141–150.

[6] E. Majorana, "Teoria simmetrica dell'elettrone e del positrone," *Nuovo Cim.* **14** no. 4, (1937) 171–184.

[7] F. T. Avignone, S. R. Elliott, and J. Engel, "Double beta decay, Majorana neutrinos, and neutrino mass," *Rev. Mod. Phys.* **80** (2008) 481–516.

[8] M. Goeppert-Mayer, "Double Beta-Disintegration," *Phys. Rev.* **48** (1935) 512–516.

[9] S. R. Elliott, A. A. Hahn, and M. K. Moe, "Direct evidence for two-neutrino double-beta decay in ^{82}Se," *Phys. Rev. Lett.* **59** (1987) 2020–2023.

[10] W. H. Furry, "On Transition Probabilities in Double Beta-Disintegration," *Phys. Rev.* **56** (1939) 1184–1193.

[11] N. Abgrall *et al.*, "The Majorana Demonstrator Neutrinoless Double-Beta Decay Experiment," *Adv. High Energy Phys.* **2014** (2014) 18.

[12] E. W. Hoppe, A. Seifert, C. E. Aalseth, A. R. Day, O. T. Farmer, T. W. Hossbach, J. I. McIntyre, H. S. Miley, J. E. Smart, and G. A. Warren, "A method for removing surface contamination on ultra-pure copper spectrometer components," *J. of Radioanal. Nucl. Chem.* **276** no. 3, (2008) 645–650.

[13] R. Cooper, D. Radford, K. Lagergren, J. F. Colaresi, L. Darken, R. Henning, M. G. Marino, and K. M. Yocum, "A Pulse Shape Analysis technique for the Majorana experiment," *Nucl. Inst. Meth. A* **629** no. 1, (2010) 303–310.

[14] P. S. Barbeau, J. I. Collar, and O. Tench, "Large-mass ultralow noise germanium

detectors: performance and applications in neutrino and astroparticle physics," *J. Cosmol. Astropart. Phys.* **2007** no. 09, (2007) 009.

[15] J. Ellis, J. S. Hagelin, D. V. Nanopoulos, K. Olive, and M. Srednicki, "Supersymmetric relics from the big bang," *Nucl. Phys. B* **238** no. 2, (1984) 453–476.

[16] H.-C. Cheng, J. L. Feng, and K. T. Matchev, "Kaluza-Klein Dark Matter," *Phys. Rev. Lett.* **89** (2002) 211301.

[17] J. D. Lewin and P. F. Smith, "Review of mathematics, numerical factors, and corrections for dark matter experiments based on elastic nuclear recoil," *Astroparticle Phys.* **6** (1996) 87–112.

[18] N. Anand, A. L. Fitzpatrick, and W. Haxton, "Model-independent Analyses of Dark-Matter Particle Interactions," *Phys. Procedia* **61** no. 0, (2015) 97–106.

[19] R. Bernabei *et al.*, "Final model independent result of DAMA/LIBRA phase 1," *Eur. Phys. J. C* **73** no. 12, (2013) 2648.

[20] C. E. Aalseth *et al.*, "Search for An Annual Modulation in Three Years of CoGeNT Dark Matter Detector Data," `arXiv:1401.3295 [astro-ph]`.

[21] C. E. Aalseth *et al.*, "Maximum Likelihood Signal Extraction Method Applied to 3.4 years of CoGeNT Data," `arXiv:1401.6234 [astro-ph]`.

[22] J. H. Davis, C. McCabe, and C. Boehm, "Quantifying the evidence for dark matter in CoGeNT data," *J. Cosmol. Astropart. Phys.* **2014** no. 08, (2014) 014.

[23] G. Angloher *et al.*, "Results from 730 kg-days of the CRESST-II Dark Matter search," *Eur. Phys. J. C* **72** no. 4, (2012) 1971.

[24] G. Angloher *et al.*, "Results on low mass WIMPs using an upgraded CRESST-II detector," *Eur. Phys. J. C* **74** no. 12, (2014) 3184.

[25] R. Agnese *et al.*, "Silicon Detector Dark Matter Results from the Final Exposure of CDMS II," *Phys. Rev. Lett.* **111** (2013) 251301.

[26] D. S. Akerib *et al.*, "First Results from the LUX Dark Matter Experiment at the Sanford Underground Research Facility," *Phys. Rev. Lett.* **112** (2014) 091303.

[27] R. Agnese *et al.*, "Search for Low-Mass Weakly Interacting Massive Particles Using Voltage-Assisted Calorimetric Ionization Detection in the SuperCDMS Experiment," *Phys. Rev. Lett.* **112** (2014) 041302.

[28] V. Cirigliano, M. L. Graesser, G. Ovanesyan, and I. M. Shoemaker, "Shining LUX on isospin-violating dark matter beyond leading order," *Phys. Lett. B* **739** no. 0, (2014) 293–301.

[29] N. Chen, Q. Wang, W. Zhao, S.-T. Lin, Q. Yue, and J. Li, "Exothermic isospin-violating dark matter after SuperCDMS and CDEX," *Phys. Lett. B* **743** no. 0, (2015) 205–212.

[30] C. E. Aalseth *et al.*, "CoGeNT: A search for low-mass dark matter using p-type point contact germanium detectors," *Phys. Rev. D* **88** (2013) 012002.

[31] A. G. Schubert, *Searching for neutrinoless double-beta decay of germanium-76 in the presence of backgrounds*. PhD thesis, University of Washington, 2012.

[32] P. Finnerty, S. MacMullin, H. Back, R. Henning, A. Long, K. Macon, J. Strain, R. Lindstrom, and R. Vogelaar, "Low-background gamma counting at the Kimballton Underground Research Facility," *Nucl. Inst. & Methods A* **642** no. 1, (2011) 65–69.

[33] P. S. Finnerty, *A Direct Dark Matter Search with the Low-Background Broad Energy Germanium Detector*. PhD thesis, University of North Carolina at Chapel Hill, 2013.

[34] J. A. Formaggio and C. Martoff, "Backgrounds to Sensitive Experiments Underground," *Annu. Rev. Nucl. Part. Sci.* **54** no. 1, (2004) 361–412.

[35] K. Rielage, "Lead Acquisition and Assay for the MAJORANA DEMONSTRATOR," tech. rep., MAJORANA internal document, 2009.

[36] M. A. Howe, G. A. Cox, P. J. Harvey, F. McGirt, K. Rielage, J. F. Wilkerson, and J. M. Wouters, "Sudbury neutrino observatory neutral current detector acquisition software overview," *IEEE Trans. Nucl. Sci.* **51** no. 3, (2004) 878–883.

[37] V. T. Jordanov and G. F. Knoll, "Digital synthesis of pulse shapes in real time for high resolution radiation spectroscopy," *Nucl. Inst. & Methods A* **345** no. 2, (1994) 337–345.

[38] R. Brun and F. Rademakers, "ROOT - An object oriented data analysis framework," *Nucl. Inst. & Methods A* **389** no. 1–2, (1997) 81–86.

[39] M. Agostini *et al.*, "The MGDO software library for data analysis in Ge neutrinoless double-beta decay experiments," *J. Phys. Conf. Ser.* **375** no. 4, (2012) 042027.

[40] J. A. Bearden and A. F. Burr, "Reevaluation of X-Ray Atomic Energy Levels," *Rev. Mod. Phys.* **39** (1967) 125–142.

[41] J. Morales *et al.*, "Filtering microphonics in dark matter germanium experiments," *Nucl. Inst. & Methods A* **321** no. 1-2, (1992) 410–414.

[42] G. Cavalleri, E. Gatti, G. Fabri, and V. Svelto, "Extension of Ramo's theorem as applied to induced charge in semiconductor detectors," *Nucl. Inst. & Meth.* **92** no. 1, (1971) 137–140.

[43] D. C. Radford. `http://radware.phy.ornl.gov/MJ/m3dcr`. M3DCR.

[44] D. C. Radford. `http://radware.phy.ornl.gov/gretina/siggen`. SIGGEN.

[45] R. A. Johnson, *Alpha Backgrounds and Their Implications for Neutrinoless Double-Beta Decay Experiments Using HPGe Detectors*. PhD thesis, University of Washington, 2010.

[46] E. Aguayo *et al.*, "Characteristics of signals originating near the lithium-diffused N+ contact of high purity germanium p-type point contact detectors," *Nucl. Instrum. & Meth. A* **701** (2013) 176–185.

[47] D. L. Donoho, I. M. Johnstone, G. Kerkyacharian, and D. Picard, "Wavelet Shrinkage: Asymptopia?," *J. R. Stat. Soc. B* **57** no. 2, (1995) 301–369.

[48] D. Donoho and I. M. Johnstone, "Adapting to Unknown Smoothness via Wavelet Shrinkage," *J. Amer. Stat. Assoc.* **90** (1995) 1200–1224.

[49] D. L. Donoho, "De-noising by soft-thresholding," *IEEE Trans. Inf. Th.* **41** no. 3, (1995) 613–627.

[50] A. Antoniadis, J. Bigot, and T. Sapatinas, "Wavelet estimators in nonparametric regression: a comparative simulation study," *J. Stat. Softw.* (2001) 1–83.

[51] M. G. Marino, *Dark Matter Physics with P-type Point-contact Germanium Detectors: Extending the Physics Reach of the* MAJORANA *Experiment*. PhD thesis, University of Washington, 2010.

[52] F. Wasilewski, "The PyWavelets python Wavelet package." `http://www.pybytes.com/pywavelets`.

[53] R. R. Coifman and D. L. Donoho, "Translation-Invariant De-Noising," in *Wavelets and statistics*, A. Antoniadis and G. Oppenheim, eds., vol. 103 of *Lecture Notes in Statistics*, pp. 125–150. Springer-Verlag, 1995.

[54] S. Mallat, *A wavelet tour of signal processing: the sparse way*. Academic Press, 3rd edition ed., 2008.

[55] R. J. E. Merry, "Wavelet theory and applications: a literature study," tech. rep., Eindhoven University of Technology, 2005.

[56] I. Daubechies, *Ten Lectures on Wavelets*. SIAM: Society for Industrial and Applied Mathematics, 1st edition ed., 1992.

[57] S. G. Mallat, "A theory for multiresolution signal decomposition: the wavelet representation," *IEEE Trans. Pattern Anal. Mach. Intell.* **11** no. 7, (1989) 674–693.

[58] H. B. Li *et al.*, "Differentiation of bulk and surface events in p-type point-contact germanium detectors for light WIMP searches," *Astroparticle Phys.* **56** (2014) 1–8.

[59] Q. Yue *et al.*, "Limits on light weakly interacting massive particles from the CDEX-1 experiment with a p-type point-contact germanium detector at the China Jinping Underground Laboratory," *Phys. Rev. D* **90** (2014) 091701.

[60] G. H. R. Kegel, "Precipitation of Lithium in Germanium during Ion Drift," *IEEE Trans. Nucl. Sci.* **15** no. 3, (1968) 332–336.

[61] F. A. Trumbore, "Solid Solubilities of Impurity Elements in Germanium and Silicon," *Bell Syst. Tech. J.* **39** no. 1, (1960) 205–233.

[62] F. J. Morin and H. Reiss, "Precipitation of lithium in germanium," *J. Phys. Chem. Solids* **3** no. 3–4, (1957) 186–209.

[63] A. J. R. de Kock, F. M. Beeftink, and K. J. Schell, "Investigation of Lithium Precipitation in Germanium Crystals by X-Ray Transmission Topography," *Appl. Phys. Lett.* **20** no. 2, (1972) 81–83.

[64] D. C. Radford, "Slow-Pulse Simulations." October 2012 MAJORANA Collaboration Meeting, 2012.

[65] T. K. Alexander, J. D. Pearson, A. E. Litherland, and C. Broude, "Pulse-Shape Discrimination on the Gamma-Ray Pulses from $F^{19}(d, n\gamma)Ne^{20}$ Observed with a Lithium-Drifted Germanium Gamma-Ray Spectrometer," *Phys. Rev. Lett.* **13** (1964) 86–88.

[66] U. Tamm, W. Michaelis, and P. Coussieu, "A pulse shape discrimination circuit for lithium-drifted germanium diodes," *Nucl. Instrum. & Meth.* **48** no. 2, (1967) 301–305.

[67] M. G. Strauss and R. N. Larsen, "Pulse height defect due to electron interaction in the dead layers of Ge(li) γ-Ray detectors," *Nucl. Instrum. & Meth.* **56** no. 1, (1967) 80–92.

[68] E. Sakai, "Slow Pulses from Germanium Detectors," *IEEE Trans. Nucl. Sci.* **18** no. 1, (1971) 208–218.

[69] G. Gilmore and J. Hemingway, *Practical Gamma Ray Spectroscopy.* Wiley & Sons, 1996.

[70] D.-M. Mei, Z.-B. Yin, and S. R. Elliott, "Cosmogenic production as a background in searching for rare physics processes," *Astroparticle Phys.* **31** no. 6, (2009) 417–420.

[71] I. Barabanov, S. Belogurov, L. Bezrukov, A. Denisov, V. Kornoukhov, and N. Sobolevsky, "Cosmogenic activation of germanium and its reduction for low background experiments," *Nucl. Inst. & Meth. B* **251** no. 1, (2006) 115–120.

[72] G. J. Alner *et al.*, "First limits on nuclear recoil events from the ZEPLIN I galactic dark matter detector," *Astrophys. J. Lett.* **23** no. 5, (2005) 444–462.

[73] J. Lindhard and M. Scharff, "Energy Dissipation by Ions in the keV Region," *Phys. Rev.* **124** (1961) 128–130.

[74] A. K. Soma *et al.*, "Extraction of Physics Signals Near Threshold with Germanium Detectors in Neutrino and Dark Matter Experiments," `arXiv:1411.4802 [ins-det]`.

[75] P. S. Barbeau, *Neutrino and Astroparticle Physics with P-Type Point Contact High Purity Germanium Detectors*. PhD thesis, University of Chicago, 2009.

[76] J. Engel, S. Pittel, and P. Vogel, "Nuclear Physics of Dark Matter Detection," *Int. J. Mod. Phys. E* **01** no. 01, (1992) 1–37.

[77] W. Eadie, D. Drijard, F. James, M. Roos, and B. Sadoulet, *Statistical Methods in Experimental Physics*. North-Holland Publ. Co., Amsterdam, 1971.

[78] E. Aprile *et al.*, "Likelihood approach to the first dark matter results from XENON100," *Phys. Rev. D* **84** (2011) 052003.

[79] J. Billard, "Profile Likelihood Ratio Analysis Techniques for Rare Event Signals," *J. Low Temp. Whys.* **176** no. 5-6, (2014) 966–972.

[80] W. A. Rolke, A. M. López, and J. Conrad, "Limits and confidence intervals in the presence of nuisance parameters," *Nucl. Inst. & Meth. A* **551** no. 2–3, (2005) 493–503.

[81] W. Verkerke and D. Kirkby, "The RooFit toolkit for data modeling," `arXiv:0306116`.

[82] M. G. Marino. `http://github.com/mgmarino/pyWIMP`. PYWIMP.

[83] R. Agnese *et al.*, "Search for Low-Mass Weakly Interacting Massive Particles with SuperCDMS," *Phys. Rev. Lett.* **112** (2014) 241302.

[84] C. Savage, G. Gelmini, P. Gondolo, and K. Freese, "Compatibility of DAMA/LIBRA dark matter detection with other searches," *J. Cosmol. Astro. Phys.* **2009** no. 04, (2009) 010.

[85] E. Aprile *et al.*, "Dark Matter Results from 225 Live Days of XENON100 Data," *Phys. Rev. Lett.* **109** (2012) 181301.

[86] G. K. Giovanetti *et al.*, "A Dark Matter Search with MALBEK," *Phys. Procedia* **00** (2014) 1.

[87] R. D. Peccei and H. R. Quinn, "CP Conservation in the Presence of Pseudoparticles," *Phys. Rev. Lett.* **38** (1977) 1440–1443.

[88] S. Weinberg, "A New Light Boson?," *Phys. Rev. Lett.* **40** (1978) 223–226.

[89] F. Wilczek, "Problem of Strong P and T Invariance in the Presence of Instantons," *Phys. Rev. Lett.* **40** (1978) 279–282.

[90] J. E. Kim, "Weak-Interaction Singlet and Strong CP Invariance," *Phys. Rev. Lett.* **43** (1979) 103–107.

[91] M. A. Shifman, A. I. Vainshtein, and V. I. Zakharov, "Can confinement ensure natural CP invariance of strong interactions?," *Nucl. Phys. B* **166** no. 3, (1980) 493–506.

[92] A. R. Zhitnitsky, "On Possible Suppression of the Axion Hadron Interactions," *Sov. J. Nucl. Phys.* **31** (1980) 260.

[93] M. Srednicki, "Axion couplings to matter: (I). CP-conserving parts," *Nucl. Phys. B* **260** no. 3–4, (1985) 689–700.

[94] J. Redondo, "Solar axion flux from the axion-electron coupling," *J. Cosmol. Astropart. Phys.* **2013** no. 12, (2013) 008.

[95] Z. Ahmed *et al.*, "Search for Axions with the CDMS Experiment," *Phys. Rev. Lett.* **103** (2009) 141802.

[96] E. Armengaud *et al.*, "Axion searches with the EDELWEISS-II experiment," *J. Cosmol. Astropart. Phys.* **2013** no. 11, (2013) 067.

[97] W. C. Haxton and K. Y. Lee, "Red-giant evolution, metallicity, and new bounds on hadronic axions," *Phys. Rev. Lett.* **66** (1991) 2557–2560.

[98] A. V. Derbin, A. I. Egorov, I. A. Mitropolsky, V. Muratova, D. A. Semenov, and E. V. Unzhakov, "Search for resonant absorption of solar axions emitted in M1 transition in ^{57}Fe nuclei," *Eur. Phys. J. C* **62** no. 4, (2009) 755–760.

[99] C. E. Aalseth *et al.*, "Experimental Constraints on a Dark Matter Origin for the DAMA Annual Modulation Effect," *Phys. Rev. Lett.* **101** (2008) 251301.

[100] E. Aprile *et al.*, "First axion results from the XENON100 experiment," *Phys. Rev. D* **90** (2014) 062009.

[101] F. T. Avignone III *et al.*, "Laboratory limits on solar axions from an ultralow-background germanium spectrometer," *Phys. Rev. D* **35** (1987) 2752–2757.

[102] G. G. Raffelt, "Astrophysical axion bounds diminished by screening effects," *Phys. Rev. D* **33** (1986) 897–909.

[103] S. Dimopoulos, J. Frieman, B. W. Lynn, and G. D. Starkman, "Axiorecombination:

A new mechanism for stellar axion production," *Phys. Lett. B* **179** no. 3, (1986) 223–227.

[104] M. Pospelov, A. Ritz, and M. Voloshin, "Bosonic super-WIMPs as keV-scale dark matter," *Phys. Rev. D* **78** (2008) 115012.

[105] P. Gondolo and G. G. Raffelt, "Solar neutrino limit on axions and keV-mass bosons," *Phys. Rev. D* **79** (2009) 107301.

[106] K. Abe *et al.*, "Search for solar axions in XMASS, a large liquid-xenon detector," *Phys. Lett. B* **724** no. 1–3, (2013) 46–50.

[107] N. Viaux, M. Catelan, P. B. Stetson, G. G. Raffelt, J. Redondo, A. A. R. Valcarce, and A. Weiss, "Neutrino and Axion Bounds from the Globular Cluster M5 (NGC 5904)," *Phys. Rev. Lett.* **111** (2013) 231301.

[108] C. S. Wu, E. Ambler, R. W. Hayward, D. D. Hoppes, and R. P. Hudson, "Experimental Test of Parity Conservation in Beta Decay," *Phys. Rev.* **105** (1957) 1413–1415.

[109] F. Reines and H. W. Sobel, "Test of the Pauli exclusion principle for atomic electrons," *Phys. Rev. Lett.* **32** no. 17, (1974) 954–954.

[110] A. Y. Ignatiev and V. A. Kuzmin, "Is a weak violation of the Pauli principle possible," *Sov. J. Nucl. Phys.* **46** (1987) 444–446.

[111] O. W. Greenberg and R. N. Mohapatra, "Local Quantum Field Theory of Possible Violation of the Pauli Principle," *Phys. Rev. Lett.* **59** (1987) 2507–2510.

[112] O. W. Greenberg, "Particles with small violations of Fermi or Bose statistics," *Phys. Rev. D* **43** (1991) 4111–4120.

[113] O. W. Greenberg, "Theories of violation of statistics," *AIP Conf. Proc.* **545** no. 1, (2000) 113–127.

[114] R. D. Amado and H. Primakoff, "Comments on testing the Pauli principle," *Phys. Rev. C* **22** (1980) 1338–1340.

[115] S. R. Elliott, B. H. LaRoque, V. M. Gehman, M. F. Kidd, and M. Chen, "An Improved Limit on Pauli-Exclusion-Principle Forbidden Atomic Transitions," *Found. Phys.* **42** no. 8, (2012) 1015–1030.

[116] M. H. Thoma and E. Nolte, "Limits on small violations of the Pauli exclusion principle in the primordial nucleosynthesis," *Phys. Lett. B* **291** no. 4, (1992) 484–487.

[117] M. Goldhaber and G. Scharff-Goldhaber, "Identification of Beta-Rays with Atomic Electrons," *Phys. Rev.* **73** (1948) 1472–1473.

[118] E. Ramberg and G. A. Snow, "Experimental limit on a small violation of the Pauli principle," *Phys. Lett. B* **238** no. 2–4, (1990) 438–441.

[119] K. Akama, H. Terazawa, and M. Yasuè, "Superficial violation of the Pauli principle due to the possible substructure of electrons," *Phys. Rev. Lett.* **68** (1992) 1826–1829.

[120] O. W. Greenberg and R. N. Mohapatra, "Phenomenology of small violations of Fermi and Bose statistics," *Phys. Rev. D* **39** (1989) 2032–2038.

[121] R. Bernabei *et al.*, "New search for processes violating the Pauli exclusion principle insodium and in iodine," *Eur. Phys. J. C* **62** no. 2, (2009) 327–332.